

The Pristine survey - XII: Gemini-GRACES chemo-dynamical study of newly discovered extremely metal-poor stars in the Galaxy

Collin L. Kielty,^{1*} Kim A. Venn¹, Federico Sestito^{1,2,3}, Else Starkenburg^{3,4}, Nicolas F. Martin^{2,5}, David S. Aguado⁶, Anke Arentsen^{2,3}, Sébastien Fabbro⁷, Jonay I. González Hernández^{8,9}, Vanessa Hill¹⁰, Pascale Jablonka^{10,11}, Carmela Lardo¹¹, Lyudmila I. Mashonkina¹², Julio F. Navarro¹, Chris Sneden¹³, Guillaume F. Thomas⁷, Kris Youakim¹⁴, Spencer Bialek¹, Rubén Sánchez-Janssen¹⁵.

¹Department of Physics and Astronomy, University of Victoria, Victoria, BC, V8W 3P2, Canada

²Université de Strasbourg, CNRS, Observatoire astronomique de Strasbourg, UMR 7550, F-67000 Strasbourg, France

³Leibniz-Institut für Astrophysik Potsdam (AIP), An der Sternwarte 16, D-14482, Potsdam, Germany

⁴Kapteyn Astronomical Institute, University of Groningen, Landleven 12, 9747 AD Groningen, The Netherlands

⁵Max-Planck-Institut für Astronomie, Königstuhl 17, D-69117, Heidelberg, Germany

⁶Institute of Astronomy, University of Cambridge, Madingley Road, Cambridge CB3 0HA, UK

⁷National Research Council of Canada, Herzberg Astronomy & Astrophysics Program, 5071 West Saanich Road, Victoria, BC, V9E 2E7, Canada

⁸Instituto de Astrofísica de Canarias, Vía Lactea, E-38205 La Laguna, Tenerife, Spain

⁹Departamento de Astrofísica, Universidad de La Laguna, E-38206 La Laguna, Tenerife, Spain

¹⁰GEPI, Observatoire de Paris, Université PSL, CNRS, Place Jules Janssen, F-92190 Meudon, France

¹¹Dipartimento di Fisica e Astronomia, Università degli Studi di Bologna, Via Gobetti 93/2, I-40129 Bologna, Italy

¹²Institute of Astronomy, Russian Academy of Sciences, RU-119017 Moscow, Russia

¹³Department of Astronomy, University of Texas at Austin, Austin, TX, 78712, USA

¹⁴Department of Astronomy, Stockholm University, SE-106 91 Stockholm, Sweden

¹⁵UK Astronomy Technology Centre, Royal Observatory Edinburgh, Blackford Hill, Edinburgh EH9 3HJ, UK

Accepted XXX. Received Dec, 2020

ABSTRACT

High-resolution optical spectra of 30 metal-poor stars selected from the *Pristine* survey are presented, based on observations taken with the Gemini Observatory GRACES spectrograph. Stellar parameters T_{eff} and $\log g$ are determined using a Gaia DR2 colour-temperature calibration and surface gravity from the Stefan-Boltzmann equation. GRACES spectra are used to determine chemical abundances (or upper-limits) for 20 elements (Li, O, Na, Mg, K, Ca, Ti, Sc, Cr, Mn, Fe, Ni, Cu, Zn, Y, Zr, Ba, La, Nd, Eu). These stars are confirmed to be metal-poor ($[\text{Fe}/\text{H}] < -2.5$), with higher precision than from earlier medium-resolution analyses. The chemistry for most targets is similar to other extremely metal-poor stars in the Galactic halo. Three stars near $[\text{Fe}/\text{H}] = -3.0$ have unusually low Ca and high Mg, suggestive of contributions from few SN II where alpha-element formation through hydrostatic nucleosynthesis was more efficient. Three new carbon-enhanced metal-poor stars are also identified (two CEMP-s and one potential CEMP-no star) when our chemical abundances are combined with carbon from previous medium-resolution analyses. The GRACES spectra also provide precision radial velocities ($\sigma_{\text{RV}} \leq 0.2 \text{ km s}^{-1}$) for dynamical orbit calculations with the Gaia DR2 proper motions. Most of our targets are dynamically associated with the Galactic halo; however, five stars with $[\text{Fe}/\text{H}] < -3$ have planar-like orbits, including one retrograde star. Another five stars are dynamically consistent with the Gaia-Sequoia accretion event; three have typical halo $[\alpha/\text{Fe}]$ ratios for their metallicities, whereas two are $[\text{Mg}/\text{Fe}]$ -deficient, and one is a new CEMP-s candidate. These results are discussed in terms of the formation and early chemical evolution of the Galaxy.

Key words: stars: metal-poor – stars: chemistry – stars: nucleosynthesis – Galaxy: formation

1 INTRODUCTION

The oldest and most metal-poor stars contain a fossil record of the star formation processes in the early Universe. These first stars would have been composed solely of hydrogen, helium, and trace amounts of lithium (Steigman 2007; Cyburt et al. 2016); without metals to efficiently cool the gas, large Jeans masses, and thereby very massive stars ($M_* \geq 100M_\odot$) are predicted to have formed (Silk 1983; Tegmark et al. 1997; Bromm et al. 1999; Abel et al. 2002; Yoshida et al. 2006). In addition, improved gas fragmentation models (e.g., Clark et al. 2011; Schneider et al. 2012) and the discovery of very low mass ultra metal-poor stars ($[\text{Fe}/\text{H}] < -4$; Keller et al. 2014; Starkenburg et al. 2017b; Schlaufman et al. 2018; Nordlander et al. 2019) have suggested that lower mass, long lived stars may have also formed in these pristine environments (e.g., Nakamura & Umemura 2001; Wise et al. 2012). Notably, if $\leq 0.8 M_\odot$ stars were to form, they could still exist today on the main sequence, and are expected to have undergone very little surface chemical evolution over their lifetimes. Detailed studies could provide invaluable constraints on (1) the nucleosynthetic yields from the first stars and the earliest supernovae (e.g., Heger & Woosley 2010; Ishigaki et al. 2014; Tominaga et al. 2014; Clarkson et al. 2018; Nordlander et al. 2019), (2) the physical conditions in the high redshift universe (where stars are too faint to be observed individually; Tegmark et al. 1997; Freeman & Bland-Hawthorn 2002; Cooke & Madau 2014; Hartwig et al. 2018; Salvadori et al. 2019), (3) the primordial initial mass function (e.g., Greif et al. 2012; Susa et al. 2014), and (4) early Galactic chemical evolution processes (see Sneden et al. 2008; Tolstoy et al. 2009; Roederer et al. 2014; Yoon et al. 2016; Wanajo et al. 2018; Kobayashi et al. 2020, and references therein).

Dedicated searches for old, metal-poor stars in the Milky Way and in its dwarf galaxy satellites were initiated over two decades ago (e.g., Bond 1980; Carney & Peterson 1981; Beers et al. 1985, 1999). Chemical abundances have now been measured for hundreds of extremely metal-poor stars (EMP), where $[\text{Fe}/\text{H}]^1 \leq -3$ (e.g., Aoki et al. 2013; Yong et al. 2013a; Cohen et al. 2013; Frebel & Norris 2015; Matsuno et al. 2017; Aguado et al. 2019) and over a dozen stars with $[\text{Fe}/\text{H}] < -4$ (see Aguado et al. 2018b,a; Bonifacio et al. 2018; Starkenburg et al. 2017b; Aguado et al. 2019; Frebel et al. 2019; Nordlander et al. 2019, and references therein). Most of the Galactic EMP stars show enhanced $[\alpha/\text{Fe}]$ abundances and a diversity of neutron capture element ratios, interpreted as the yields from core-collapse supernovae with different progenitor masses and explosion prescriptions. More recently, the importance of compact binary mergers to the r-process abundance ratios has also been revealed (Ji et al. 2016; Roederer et al. 2016; Hansen et al. 2017). In dwarf galaxies, the abundance ratios of hydrostatic elements (e.g., O, Na, Mg), explosive elements (e.g., Si, K, Mn), complex elements (like Zn), and heavy elements (as Ba, Y) tend to be lower than those of their Galactic counterparts of similar metallicity. This reflects a range of differences in their star formation histories, including interstellar mixing efficiencies, star formation efficiencies, star formation rates, and effective mass functions of the dwarf galaxy systems (Venn et al. 2004; Tolstoy et al. 2009; Nissen & Schuster 2010; McWilliam et al. 2013; Frebel & Norris 2015; Hasselquist et al. 2017; Hayes et al. 2018; Lucchesi et al. 2020). The diversity of chemical abundance profiles seen in this sparse population of

objects makes for challenging statistical studies. Targeted programs are needed to uncover larger samples of these (nearly) pristine stars.

The present day locations of metal-poor stars also a diagnostic of early galaxy formation. Based on cosmological simulations of the Local Group, it is thought that the Galactic halo was formed through the accretion and disruption of dwarf galaxies at early epochs. Consequently, properties of the old, metal-poor stars seen in the halo manifest in the properties of their dwarf galaxy hosts (e.g., Ibata et al. 1994; Helmi et al. 1999; Johnston et al. 2008; Wise et al. 2012; Starkenburg et al. 2017a; El-Badry et al. 2018). The arrival of precision proper motions from *Gaia* DR2 (Gaia Collaboration et al. 2018), and increasingly large datasets of stars with precision radial velocities from high-resolution spectroscopy, has enabled the determination of orbits for halo stars. The majority of the EMP halo stars have been shown to have high-velocities and eccentric orbits, consistent with accretion from a dwarf galaxy (Sestito et al. 2019, 2020; Di Matteo et al. 2020; Cordoni et al. 2021). A large population of halo stars has also been found with retrograde orbits and kinematics consistent with a halo merger remnant, e.g., *Gaia-Enceladus/Sausage* (Meza et al. 2005; Belokurov et al. 2018; Helmi et al. 2018; Myeong et al. 2018) and *Gaia-Sequoia* (Barbá et al. 2019; Myeong et al. 2019; Matsuno et al. 2017; Monty et al. 2020; Cordoni et al. 2021).

The Galactic halo is not the only place to look for old stars. Curiously, some EMP stars have been found on nearly circular, planar orbits (Caffau et al. 2012; Sestito et al. 2019, 2020; Schlaufman et al. 2018; Venn et al. 2020). Since the Galactic plane is thought to have formed ~ 10 Gyr ago (Casagrande et al. 2016), these stars challenge the idea that the metal-poor stars are amongst the oldest stars accreted from the mergers of dwarf galaxies. The Galactic bulge is another environment to look for relics of first stars (White & Springel 2000; Guo et al. 2010; Starkenburg et al. 2017a; El-Badry et al. 2018). To date, ~ 2000 very metal-poor stars ($[\text{Fe}/\text{H}] < -2.0$) associated with the bulge have been found (García Pérez et al. 2015; Howes et al. 2015, 2016; Lamb et al. 2017; Arentsen et al. 2020b). Detailed chemical abundance analyses for these objects are limited, especially at the lowest metallicities, but they indicate that many of the metal-poor bulge candidates are chemically similar to halo stars (Lucey et al. 2019). In fact, estimates of their orbital properties using the exquisite astrometry from *Gaia* DR2 (Gaia Collaboration et al. 2018) suggests that up to 50% of these stars may be normal halo stars with highly elliptical and plunging orbits, a fraction which increases with decreasing metallicity (Lucey et al. 2020). However, while *Gaia* DR2 proper motions are extremely valuable in eliminating foreground metal-poor non-bulge members, the uncertainties on the parallax measurements for most stars in the bulge are currently too large for reliable distance estimates.

Regardless of where metal-poor stars are found, the union of stellar dynamics and chemical cartography provides a foundation for studies of *Galactic Archaeology* (e.g., Carney et al. 2003; Freeman & Bland-Hawthorn 2002; Venn et al. 2004; Hayden et al. 2015; Bovy et al. 2016; Hasselquist et al. 2017). Dedicated surveys have been successful in finding most of the metal-poor stars; these include the HK and Hamburg-ESO surveys (Beers et al. 1992; Christlieb et al. 2002; Beers & Christlieb 2005), the SDSS SEGUE, BOSS, and APOGEE surveys (Yanny et al. 2009; Eisenstein et al. 2011; Majewski et al. 2015), LAMOST (Cui et al. 2012), and more recently the narrow band imaging surveys *SkyMapper* (Keller et al. 2007; Da Costa et al. 2019; Onken et al. 2020) and *Pristine* (Starkenburg et al. 2017b). The discovery of more EMP stars is necessary to build a statistically significant sample to study the metal-poor Galaxy, and

¹ We adopt the square bracket notation for chemical abundances relative to the Sun, such that $[X/Y] = \log(X/Y)_\odot - \log(X/Y)_*$, where X and Y are column densities for two given elements.

also to overcome cosmic variance in the chemo-dynamic analysis of stellar populations within it.

In this paper, 30 new candidate EMP stars have been selected from the *Pristine* survey for follow-up high-resolution spectroscopy. *Pristine* is based on a MegaPrime/MegaCam imaging survey at the 3.6-metre Canada France Hawaii Telescope, using a unique narrow-band filter centered on the Ca II H & K spectral lines (*CaHK*). When *CaHK* is combined with the broad-band SDSS *gri* photometry (York et al. 2000) or Gaia DR2 photometry, this *CaHK* filter can be calibrated to find metal-poor candidates with $4000 < T_{\text{eff}} < 7000$ K (Youakim et al. 2017; Starkenburg et al. 2017b; Arentsen et al. 2020a). The *Pristine* survey has been shown to successfully predict stellar metallicities. $\sim 56\%$ of stars with $[\text{Fe}/\text{H}]_{\text{phot.}} < -2.5$ are confirmed to have $[\text{Fe}/\text{H}] < -2.5$ ($\sim 23\%$ when $[\text{Fe}/\text{H}]_{\text{phot.}} < -3.0$) based on follow-up spectroscopic studies (Youakim et al. 2017; Caffau et al. 2017; Bonifacio et al. 2019b; Aguado et al. 2019; Venn et al. 2020). The target stars for this paper were selected from the medium-resolution spectroscopic follow-up studies of EMP candidates found within the initial ~ 2500 sq. degree footprint² of the *Pristine* survey (Martin et al., in prep.). In Section 4, we improve upon the the previous stellar parameter determinations; in Section 5, we calculate the chemical abundances or upper-limits for ~ 15 elements; and in Section 6, we estimate the orbits using the Gaia DR2 database for a chemo-dynamical analysis. Together, these properties permit a study of the origins of these metal-poor stars themselves, ultimately to unravel the formation history of the Milky Way Galaxy.

2 TARGET SELECTION

Targets in this paper have been selected from the original 2500 sq. degree *Pristine* photometric survey (Starkenburg et al. 2017b; Youakim et al. 2017) and medium-resolution spectroscopic follow-up survey (Youakim et al. 2017; Aguado et al. 2019). All of the medium-resolution spectra (hereafter MRS) were observed at the Isaac Newton Telescope (INT), and were analysed using the FERRE data analysis pipeline (Prieto et al. 2006) and the ASSET grid of synthetic stellar spectra as described and published by Aguado et al. 2017. FERRE searches for the best fit to the observed spectrum by simultaneously deriving the main stellar atmospheric parameters (effective temperature, surface gravity, and metallicity $[\text{Fe}/\text{H}]$), and it also determines the carbonicity, $[\text{C}/\text{Fe}]$. Uncertainties are found via Markov Chain Monte Carlo (MCMC) sampling around the best fit stellar parameters. Stars with a very high probability ($> 90\%$) for a *Pristine* metallicity $[\text{Fe}/\text{H}]_{\text{phot.}} < -2.75$ in both the ($g-i$) and ($g-r$) calibrations are shown in Fig. 1 (in grey). The metallicities from the INT medium-resolution spectral analyses by FERRE for those *same stars* are also shown in Fig. 1 (in red). Clearly some of our initial *Pristine* metallicities were too low; however, significant improvements in the *Pristine* selection function have been made since our original MRS spectroscopic follow-up programs, in anticipation of providing targets for the WEAVE survey (Dalton et al. 2014, 2018).

Targets in this paper with high-resolution spectroscopy have been selected with $[\text{Fe}/\text{H}]_{\text{MRS}} < -3$ and low temperatures ($T_{\text{eff}} < 6500$ K) in the magnitude range $14.8 < V < 16.4$. These are noted in blue in Fig. 1. We have observed $< 5\%$ of the full sample from the original footprint area, showing that a spectroscopic

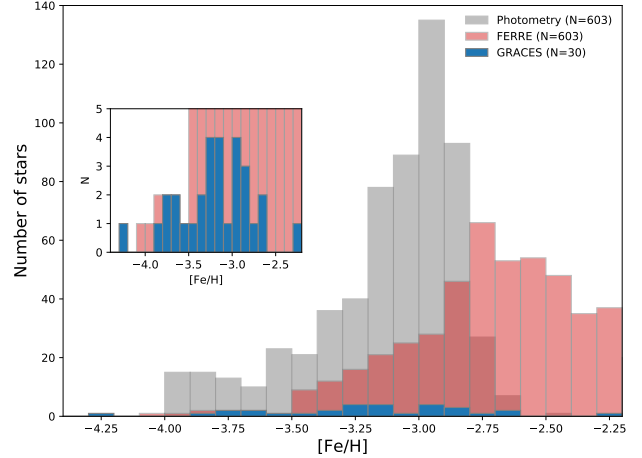


Figure 1. The metallicity distribution for the full sample of metal-poor stars found in the original *Pristine* footprint. The grey and pink distributions are for the same sample of stars ($V < 18$, Aguado et al. 2019), showing that medium-resolution spectral follow-up found slightly higher metallicities for this sample. GRACES metallicities from this paper are shown in blue (inset included for higher detail). Clearly, there are many more EMP candidates available for high-resolution spectroscopic analyses.

survey like WEAVE is necessary to reach all of them. Some stars with enhanced carbon were included ($[\text{C}/\text{Fe}]_{\text{FERRE}} > 1$); however, stars with non-normal carbon abundances were not given a higher priority in the target selection because the carbon abundances are typically unreliable when low SNR (< 25) and low-resolution data are analysed with the FERRE pipeline (see below, also Aguado et al. 2019, Arentsen et al. in prep.).

The targets analysed in this paper are listed in Table B1. The stellar identifications (IDs) are a combination of their SDSS RA and DEC coordinates and V are in observer magnitudes calculated from SDSS u, g, r, i, z given the calibration by (Lupton et al. 2005). The other SDSS and *Pristine* filter magnitudes have been dereddened using $E(B-V)$ from (Schlegel et al. 1998). Table B1 also lists the information on the exposures and the SNR of the final combined spectrum for each target. Stellar parameters from the *Pristine* survey are listed in Table B2. This includes the photometric *Pristine* metallicities ($[\text{Fe}/\text{H}]_{\text{phot.}}$) and the colour temperatures ($T_{\text{phot.}}$), which are an average of the dwarf and giant solutions from SDSS *gri* and *Pristine CaHK* photometry (see Starkenburg et al. 2017b). Table B2 also includes the stellar parameters from the FERRE analysis of the INT medium-resolution spectroscopic survey by Aguado et al. (2019) for our sample. The average SNR = 28 for the MRS of our targets, with a range $7 < \text{SNR} < 79$. As mentioned above, the FERRE pipeline simultaneously determines the effective temperature (T_{eff}), surface gravity ($\log g$), metallicity $[\text{Fe}/\text{H}]_{\text{MRS}}$, and carbonicity $[\text{C}/\text{Fe}]_{\text{MRS}}$ for each star. Radial velocities are also derived from MRS ($\Delta RV \sim 1$ km s⁻¹). Aguado et al. (2019) investigated the FERRE carbonicity measurements as functions of both surface gravity and SNR. They find that carbon abundances are more reliably determined (systematic uncertainties of ~ 0.2 dex) for cool, lower gravity giants, primarily due to the increased strength of spectral lines at lower temperatures. Likewise, increased line strength means lower SNR is needed for a detection of the G band. Conversely, the uncertainties in the carbon abundances increases up to ~ 0.6 dex for the hotter, higher gravity stars, where weaker spectral features and less reliable surface gravities are expected. Since the carbon measurement is so

² We note that the *Pristine* survey has more than doubled its survey area since its initial footprint.

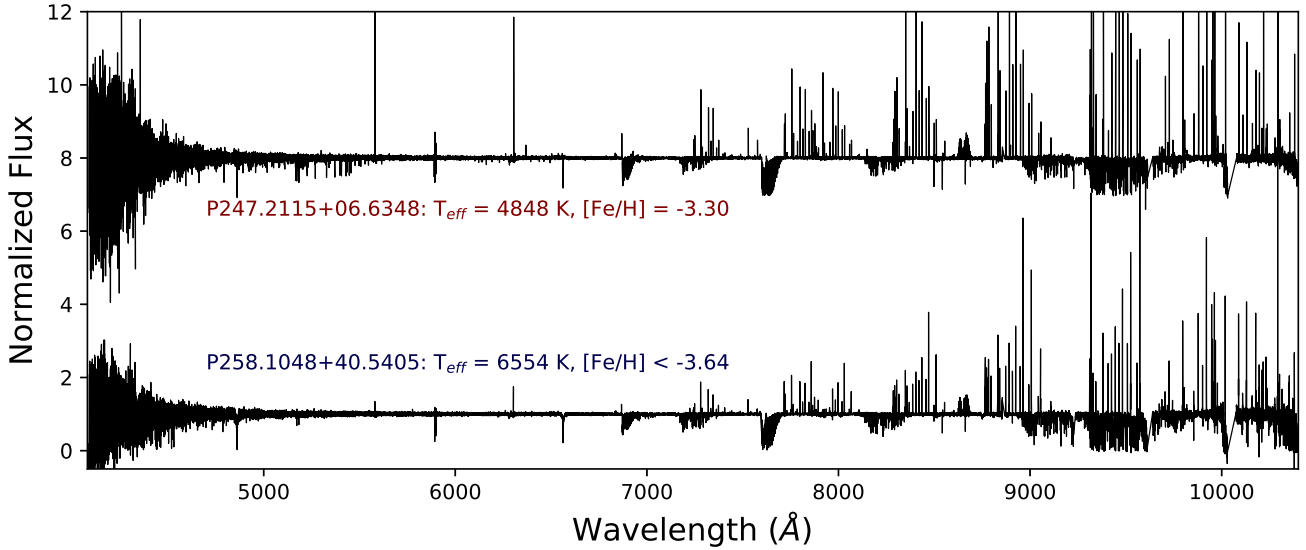


Figure 2. Full Gemini/GRACES spectra for the hottest and coolest stars in our sample. Even though the star+sky mode was used, the sky subtraction is clearly imperfect due to the presence of emission lines at longer wavelengths. The poor throughput below $\sim 4800\text{\AA}$ of the long 270-metre optical fibre can be seen as an decrease in the SNR at blue wavelengths.

heavily dependent on both SNR and gravity, we do not report individual values for $[\text{C}/\text{Fe}]_{\text{MRS}}$ in Table B2, and instead flag stars as C-rich candidates if $[\text{C}/\text{Fe}]_{\text{MRS}} > 1.0$. The stars are flagged further to note whether the carbon abundances are *reliable*, based on the SNR of the medium-resolution INT spectra analysed by FERRE.

3 GEMINI-GRACES OBSERVATIONS

High-resolution spectra have been collected for 30 extremely metal-poor candidates with the Gemini Remote Access to CFHT ESPaDOnS Spectrograph (GRACES; [Chene et al. 2014](#); [Pazder et al. 2014](#)). A 270-metre optical fibre links the Cassegrain focus at the Gemini-North telescope to the Canada-France-Hawaii Telescope ESPaDOnS spectrograph (a cross-dispersed high-resolution échelle spectrograph that covers the whole visible spectrum; [Donati et al. 2006](#)). We note that the exposure times we used were in good agreement with the GRACES ITC provided by Gemini Observatory. In the 2-fibre (object+sky) mode, spectra are obtained with resolution $R \sim 65,000$; however, light below $\sim 4800\text{\AA}$ is severely limited by poor transmission through the optical fibre link.

The GRACES spectra have been reduced using the Gemini “Open-source Pipeline for ESPaDOnS Reduction and Analysis” tool (OPERA, [Martoli et al. 2012](#)). This includes standard calibrations (images are bias subtracted, flat fielded, extracted, wavelength calibrated, and heliocentric corrected). Starting from the individually extracted and normalized échelle orders (the *.i.fits files), one continuous spectrum is stitched together by weighting the overlapping wavelength regions by their error spectrum, and co-adding as a weighted average. All visits for a given star are examined for radial velocity (RV) variations, potentially indicating binarity; no evidence for binary systems was found based on the criteria $\Delta\text{RV} \leq 1\text{ km s}^{-1}$, although we note radial velocity variations are unlikely to be measured due to the short cadence of our observations. All visits for a given star have then been co-added via a weighted

mean using the error spectrum. The coadded spectrum has then been radial velocity corrected through cross-correlation with a high SNR comparison spectrum of the metal-poor standard star HD 122563. Other radial velocity standards were examined (e.g., Arcturus and a synthetic spectrum for a typical metal-poor RGB), however the solutions had the smallest uncertainties ($\sigma_{\text{RV}} \leq 0.2\text{ km s}^{-1}$) when compared to HD 122563. As a final step, the RV corrected spectra were re-normalized using k-sigma clipping with a nonlinear filter (a combination of a median and a boxcar). The effective scale length of the filter ranged from 8 to 15 \AA , dependent on the crowding of the spectral lines, which was sufficient to follow the continuum when used in conjunction with iterative clipping. The full wavelength coverage of the final spectra for two sample stars is shown in Fig. 2, including the imperfect sky subtraction, as seen by the night sky emission lines above $\sim 8000\text{\AA}$.

4 STELLAR PARAMETERS AND RADIAL VELOCITIES

The stellar temperatures (T_{eff}) have been determined using the colour-temperature relation for Gaia photometry from [Mucciarelli & Bellazzini \(2020\)](#) (MB2020). This calibration was selected based on their inclusion of very metal-poor stars (from [González Hernández & Bonifacio 2009](#)). When calculating temperatures from MB2020, it is necessary to know if the star is a dwarf or giant (two sets of calibrations) and to have a metallicity estimate *a priori*. Using the Gaia parallaxes, we were able to estimate the likelihood of an individual star as a dwarf or giant (see below), and we adopted the initial metallicities determined from the *Pristine* survey photometry and INT medium-resolution spectroscopic analysis ([Aguado et al. 2019](#)). Colours were dereddened using [Schlafly & Finkbeiner \(2011\)](#), adapted for Gaia DR2 photometry³. A comparison of our temperatures from the MB2020 calibration to those from

³ Gaia DR2 extinction values (v 3.4) at <http://stev.oapd.inaf.it/cgi-bin/cmd>.

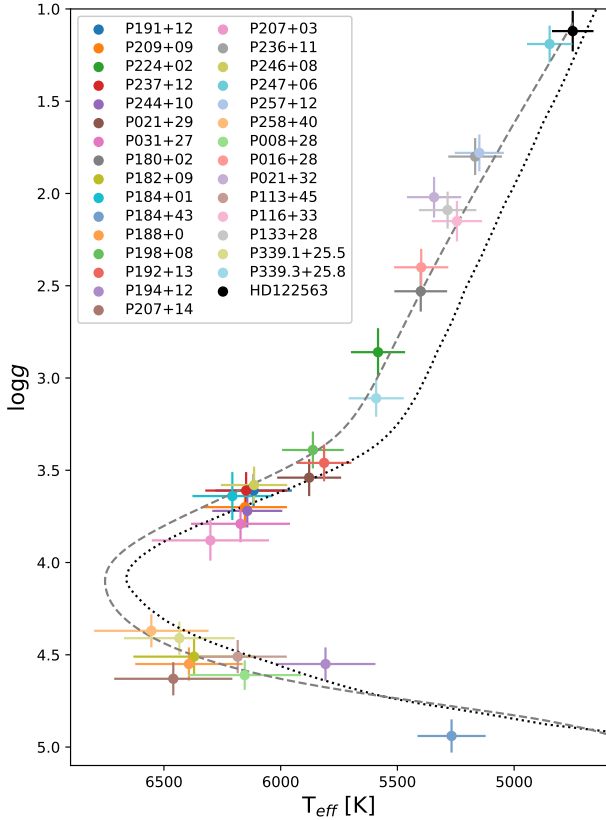


Figure 3. T_{eff} and $\log g$ derived from Mucciarelli & Bellazzini (2020) and the Stefan-Boltzmann law. MIST/MESA (dashed grey line) and Yale-Yonsei (dotted black line) isochrones with $[\text{Fe}/\text{H}] = -3.5$ and age = 13 Gyr are shown for visual reference.

the Casagrande et al. (2020) calibration showed very good agreement, even though the latter had very few standard stars at very low metallicities.

Surface gravities ($\log g$) were determined using the Stefan-Boltzmann equation (e.g., Venn et al. 2017; Kraft & Ivans 2003). This method requires (i) a distance, which we calculate from the Gaia DR2 parallax assuming the parallax zero point offset from Lindegren et al. (2018), (ii) the solar bolometric magnitude⁴ of $M_{\text{bol}} = 4.74$, and (iii) bolometric corrections for Gaia DR2 photometry (Andrae et al. 2018).

Uncertainties in T_{eff} and $\log g$ were determined from a Monte Carlo analysis on the uncertainties from the input parameters, as well as assuming a flat prior on the stellar mass, spanning 0.5 to 1.0 M_{\odot} . The final stellar parameter, microturbulence ξ , was determined from the surface gravity values, using the calibrations by Sitnova et al. (2015) for dwarf stars and Mashonkina et al. (2017) for giants.

This method was selected over the use of isochrones due to significant differences between the MIST/MESA (Paxton et al. 2011; Dotter 2016; Choi et al. 2016) and Yale-Yonsei isochrones (Demarque et al. 2004; Lejeune et al. 1998) for old, metal-poor stars shown in Fig. 3. The quality of the spectral parameters using the MIST/MESA isochrones for metal-poor stars has been questioned.

⁴ IAU 2015 Resolution B2 on the bolometric magnitude scale available at https://www.iau.org/static/resolutions/IAU2015_English.pdf.

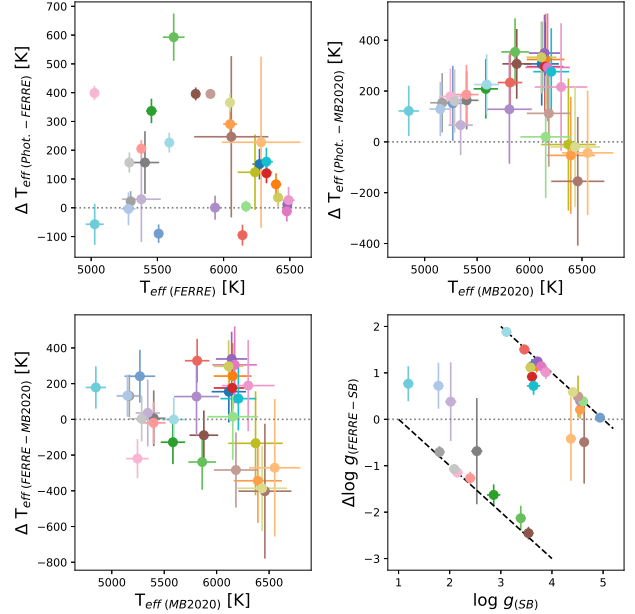


Figure 4. Comparison of T_{eff} and $\log g$ derived from SDSS photometry, medium-resolution spectroscopy, and our method of using the Mucciarelli & Bellazzini (2020) calibration with the Stefan-Boltzmann law (see text). Dashed black lines of fixed $\log g_{\text{FERRE}} = 1.0$ and 5.0 (the bounds of the FERRE grid) are shown in the bottom right panel. See Fig. 3 for star labels.

For example, Monty et al. (2020) found good agreement between spectroscopic and isochrone-mapping temperature determinations for stars with $[\text{Fe}/\text{H}] > -2$. However, for lower metallicities, the temperatures determined from isochrone-mapping tended to be hotter, by up to $\Delta T_{\text{eff}} = +500$ K when $[\text{Fe}/\text{H}] = -3.5$. A similar result has been seen by Joyce & Chaboyer (2015, 2018) due to a range of (optimized) values for the convective mixing length parameter. Nevertheless, a comparison of our temperatures from the MB2020 calibrations to those from the Bayesian inference method using MIST/MESA isochrones developed by Sestito et al. (2019) showed good agreement for dwarfs and red giants. Where we found significant deviations were for our EMP stars on the sub-giant branch and those predicted to be carbon-rich.

A comparison of our stellar parameters (Table B3) to those determined from our medium-resolution FERRE analysis (Table B2) are shown in the bottom row of Fig. 4. The FERRE stellar parameter errors are the FERRE MCMC fitting errors to the spectra. The SDSS photometric colour estimates for temperature (Table B1) are also shown for comparisons in the top row of Fig. 4, where separate dwarf and giant solutions have been averaged together. We note that the MB2020 calibrations appear to be well constrained for EMP stars on the red giant branch and the main sequence (see their Fig. 2). Nevertheless, for hotter stars, which are typically the main sequence or main sequence turn off stars, there are larger temperature uncertainties as seen in Fig. 4. From tests in our MCMC analysis of temperature, we find this is simply due to a nearly constant uncertainty in the colours that scales to a slightly larger temperature uncertainty as the temperature increases.

Overall, the agreement between our temperatures from MB2020 and the FERRE MRS analysis are in good agreement ($\sigma_{T_{\text{eff}}} \sim 200$ K). The SDSS photometric temperatures tend to be hotter than our temperatures or those from the FERRE MRS anal-

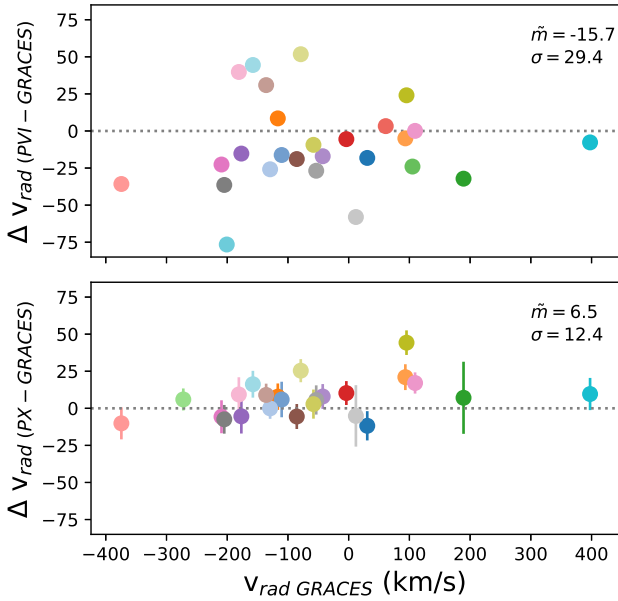


Figure 5. Comparison of the radial velocities (RVs) derived from our GRACES spectra and those from medium-resolution INT spectra. The MRS radial velocities in the top panel are from *Pristine VI* (PVI [Aguado et al. 2019](#)), and improved measurements with uncertainties are shown in the lower panel from *Pristine X* (PX [Sestito et al. 2020](#)). The GRACES RV errorbars are smaller than the point sizes. The median offset (\bar{m}) and standard deviation (σ), both in km/s, are shown in each panel. See Fig. 3 for star labels.

ysis, by $\Delta T_{\text{eff}} \sim 200$ K. Only the hottest stars show photometric and FERRE MRS temperatures that are cooler than ours. On the other hand, our values for $\log g$ are more precise than those from the FERRE MRS analysis. Due to the low SNR of the MRS, FERRE is forced to make a dwarf/giant distinction, forcing the gravities to values to be near the edges of their synthetic grid ($\log g = 1.0$ or 5.0). Similar trends in gravity have been seen when comparing the FERRE MRS results to other high-resolution spectral analyses of EMP stars in our group ([Bonifacio et al. 2019a](#); [Venn et al. 2020](#); [Arentsen et al. 2020b](#)).

A comparison of radial velocity values from the medium-resolution spectra and our high-resolution GRACES spectra is shown in Fig. 5. There has been significant improvement in the radial velocity determinations between our initial MRS results (in *Pristine VI*, [Aguado et al. 2019](#)) and the most recent MRS analysis (in *Pristine X*, [Sestito et al. 2020](#)). The most recent MRS radial velocities show a mean offset of only $\Delta(\text{RV}) \sim 6$ km/s, with a dispersion of 12 km/s, relative to our HRS values.

5 CHEMICAL ABUNDANCES

Chemical abundances are determined for each star using the stellar parameters discussed above and a classical model atmospheres analysis. Model atmospheres were generated using the most up-to-date models on the MARCS website⁵ ([Gustafsson et al. 2008](#), with additions by B. Plez); the OSMARCS spherical models are used

⁵ MARCS model atmospheres at <https://marcs.astro.uu.se/>

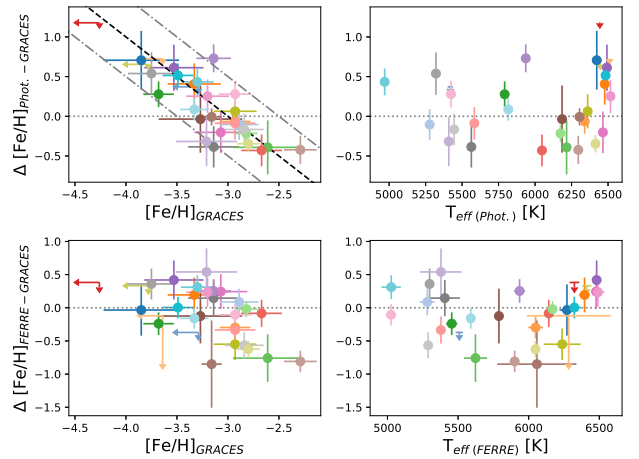


Figure 6. Comparison of $[\text{Fe}/\text{H}]$ derived from photometry, MRS INT spectra, and our GRACES spectra. Dashed lines of fixed $[\text{Fe}/\text{H}] = -2.5, -3.0,$ and -3.5 are shown in the top left panel, which suggest that our *Pristine* survey photometric metallicities may be limited to $[\text{Fe}/\text{H}] \gtrsim -3$. Y-axes are shared between left and right panels.

when $\log g < 3.5$. Spectral lines of iron were selected from the recent metal-poor stars analyses by [Norris et al. \(2017\)](#) and [Monty et al. \(2020\)](#). Atomic data was adopted from the *linemake*⁶ atomic and molecular line database. Chemical abundances are compared to the Sun using the [Asplund et al. \(2009\)](#) solar data.

Elemental abundances are calculated in a three step process: (1) the list of well known iron lines was examined in each spectrum for an initial iron abundance, and the metallicity of the model atmosphere was updated. This process was run twice with the updated metallicities to ensure convergence. (2) A new synthesis of all elements was generated including line abundances and upper limits for all of the clean spectral lines (e.g., see Figs. 7, 10, 11). (3) For the more challenging spectral features (i.e., those that were more severely blended or required hyperfine structure corrections), then a full spectrum synthesis was carried out using *linemake* to find all features and components within ± 10 Å of the feature of interest. When a spectral feature was well fit, then the abundance was measured. If not, a 3σ upper limit was calculated. Each synthetic spectrum was broadened in MOOG using a Gaussian smoothing kernel with $\text{FWHM}=0.15$, other than two stars (P198+08 and P016+28) which required more broadening ($\text{FWHM}=0.25$). When there were multiple spectral lines for a given element, then the average of the measured abundances, or the lowest (most constrained) upper limit, was adopted. The number of lines synthesized per element ranged from 1 (Eu II) to 25 (Cr I). Blends, isotopic corrections, and hyperfine structure corrections were taken from *linemake* and included in the spectrum syntheses for lines of Li I, O I, Sc II, Mn I, Cu I, Zn I, Y II, Zr II, Ba II, La II, and Eu II. A sample line list is available in Appendix B; the full line list is available online.

Abundance errors are determined in two ways: (1) the line to line variations that represent measurement errors, e.g., in the contin-

⁶ *linemake* contains laboratory atomic data (transition probabilities, hyperfine and isotopic substructures) published by the Wisconsin Atomic Physics and the Old Dominion Molecular Physics groups. These lists and accompanying line list assembly software have been developed by C. Sneden and are curated by V. Placco at <https://github.com/vmplacco/linemake>.

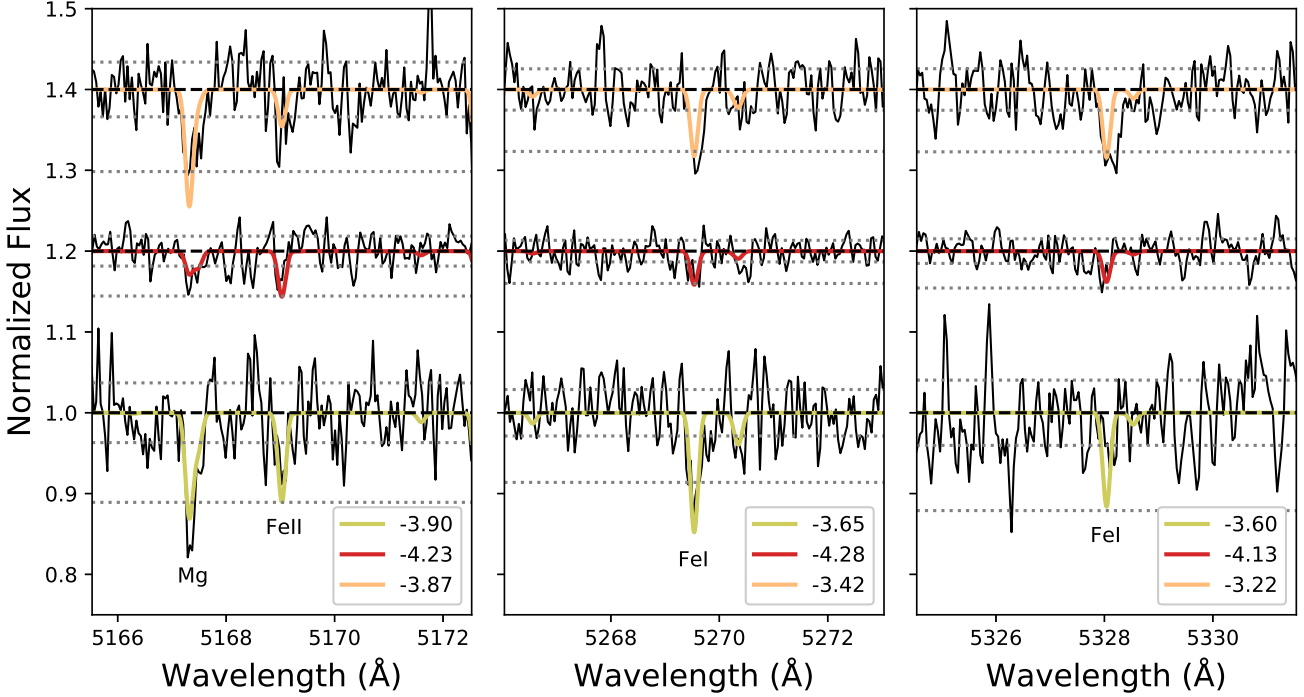


Figure 7. Synthesized Fe I and Fe II lines for the three stars with only Fe upper limits. Arranged top to bottom in order of hottest to coolest are P258+40 ($T_{\text{eff}} = 6554\text{K}$), P237+12 ($T_{\text{eff}} = 6148\text{K}$), and P246+08 ($T_{\text{eff}} = 6140\text{K}$). Three Fe lines are shown (Fe II 5169.028Å, Fe I 5269.537Å, and Fe I 5328.039Å), chosen as they provide the tightest constraints on [Fe/H] for most stars in our sample. The GRACES spectra (solid black line) are compared to synthesized spectra (solid coloured lines that match the colour labels in Fig. 3 per star). The [Fe/H] abundances used in the synthetic spectra are noted in each panel. The continuum placement (dashed black line) and the $\pm 1\sigma$ and -3σ noise levels (grey dotted lines) are shown.

uum placement and/or due to the local SNR (see Tables B3 to B6), and (2) systematic uncertainties due to the stellar parameters (see Tables B7 to B12). The final abundance uncertainties are calculated by adding the line-to-line scatter (σ_{EW}) in quadrature with the uncertainties imposed by the stellar parameter errors ($\sigma_{T_{\text{eff}}}$, $\sigma_{\log g}$, and $\sigma_{[\text{Fe}/\text{H}]}$). These final uncertainties are used in the abundance plots (i.e., Figures 6, 8-9, A2, A4).

The EMP standard star HD 122563 has been analysed from an archival very high SNR (>200) GRACES spectrum. We determined its stellar parameters using the same methods as for the GRACES targets, and find $T_{\text{eff}} = 4750 \pm 89$ K, $\log g = 1.12 \pm 0.11$, after adopting an initial metallicity of $[\text{Fe}/\text{H}] = -2.7$. These results are in fair agreement with the literature; e.g., Collet et al. (2018) revisit the analysis of this star with high resolution 3D model atmospheres. They adopt $T_{\text{eff}} = 4600 \pm 47$ K based on the IR flux method by Casagrande et al. (2014), and they use the Stefan-Boltzman formula to determine surface gravity $\log g = 1.61 \pm 0.07$, based on the available parameters at that time (e.g., they adopted a larger *Hipparcos* parallax $\pi' = 4.22 \pm 0.35$ mas vs the Gaia DR2 value of $\pi' = 3.444 \pm 0.063$ with zero point offset of -0.029 mas). Their results are consistent with other photometric, interferometric, and spectroscopic methods, whereas ours are both hotter and brighter based on the new Gaia DR2 parallax measurement. Nevertheless, our abundance results for HD 122563 are similar to those in the literature and to other Galactic standard stars (see Figs. 9, 12, and A2.)

5.1 Iron-group

Iron abundances are calculated from the average of the synthetic fits to each spectral feature identified in Table B15. Iron is calculated from Fe I and Fe II independently, where [Fe/H] in Table B3 is the weighted average.

A comparison of the iron abundances between our high-resolution GRACES spectra, the MRS analysis, and the *Pristine* photometric estimates are shown in Fig. 6. In the top left panel, lines of constant metallicity are shown at $[\text{Fe}/\text{H}] = -2.5$, -3.0 , and -3.5 . This plot suggests that the precision in the current *Pristine* photometric metallicities may be limited to $[\text{Fe}/\text{H}] \geq -3$, particularly for the hotter stars that dominate our sample. In the top right panel, our metallicities from the GRACES analyses suggest that the *Pristine* photometric metallicities near $[\text{Fe}/\text{H}] = -3$ have an intrinsic dispersion of $\Delta[\text{Fe}/\text{H}] \sim \pm 0.5$. This dispersion appears to be even larger for the FERRE results, as seen in the bottom left panel. The latter may also be temperature dependent, in that stars near $T_{\text{eff}}(\text{FERRE}) = 6000$ K result in $[\text{Fe}/\text{H}]_{\text{MRS}}(\text{FERRE})$ metallicities that are too low, as seen in the bottom right panel.

Samples of the spectrum synthesis of three Fe lines (and one Mg line) are shown in Fig. 7 for three stars: P258+40 ($T_{\text{eff}} = 6554$ K), P237+12 ($T_{\text{eff}} = 6148$ K), and P246+08 ($T_{\text{eff}} = 6140$ K). Note that P237+12 is the lowest metallicity star in our sample, and we determine an upper limit of $[\text{Fe}/\text{H}] \leq -4.26$, despite a very high SNR spectrum ($\text{SNR} \sim 95$ at 6000 Å). This is partially due to the limited (red) wavelength region available in the GRACES spectra and lack of strong Fe II lines in this wavelength region. Examination of all three spectral lines shown in Fig. 7 provide the mean 1DLTE

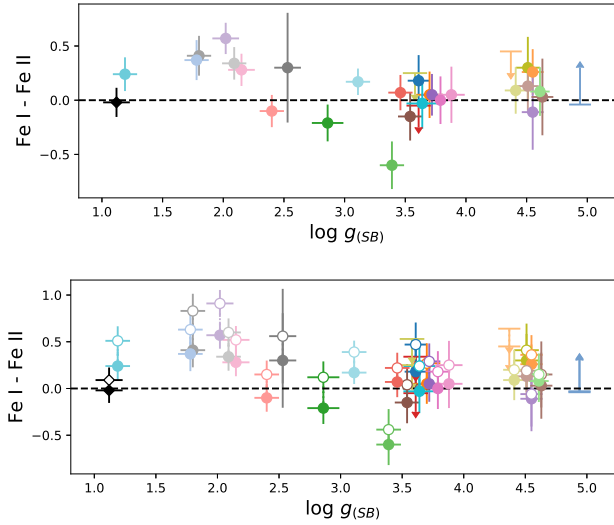


Figure 8. Comparison of $[\text{Fe I}/\text{H}] - [\text{Fe II}/\text{H}]$ vs. surface gravity derived from the Stefan-Boltzmann law. Upper panel are 1DLTE abundances, and lower panel includes NLTE corrections (open circles; see text). $[\text{Fe II}/\text{H}]$ is lower than $[\text{Fe I}/\text{H}]$ for a majority of the stars. The dashed black line at $[\text{Fe I}/\text{H}] - [\text{Fe II}/\text{H}] = 0$ represents ionization equilibrium - a spectroscopic check for the accuracy of the surface gravity. Reference star HD 122563 is shown as the black diamond.

3σ upper limit for P237+12. A follow-up VLT-UVES spectrum of this star confirms this low metallicity from more and bluer iron features (Lardo et al., *in prep.*).

Departures from LTE are known to overionize the Fe I atoms due to the impact of the stellar radiation field on the level populations, particularly in hotter stars and metal-poor giants. These non-LTE (NLTE) effects can be significant in our stellar parameter range. To investigate the impact of NLTE corrections on the iron abundances, the $[\text{Fe I}/\text{H}] - [\text{Fe II}/\text{H}]$ differences are compared to the surface gravities in Fig. 8. We find that Fe I and Fe II are in excellent agreement for the dwarfs and subgiants ($\log g \geq 2.5$), whereas Fe II tends to be lower than Fe I for the giants (by $> 1\sigma$). This is *not* the typical signature of neglected NLTE effects. NLTE corrections are examined from two databases; (1) INSPECT⁷ provides NLTE corrections for some of our Fe I and Fe II lines (Bergemann et al. 2012; Lind et al. 2012), and (2) the MPIA NLTE grid⁸ which provides NLTE correction for several additional lines (Bergemann et al. 2012; Kovalev et al. 2019). The NLTE corrections for our Fe II lines are negligible throughout. However, when the Fe I NLTE corrections are applied (bottom panel), the differences increase such that the giants show $\langle [\text{Fe I}/\text{H}]_{\text{NLTE}} - [\text{Fe II}/\text{H}] \rangle \sim +0.5$. The average NLTE corrections per star are summarized in Table B3.

Offsets in stellar parameters due to enhancements of certain chemical elements have been predicted to affect the isochrones for old, metal-poor stars (VandenBerg et al. 2012). Specifically, enhanced $[\text{Mg}/\text{Fe}]$ or $[\text{Si}/\text{Fe}]$ by +0.4 relative to scaled-solar has been predicted to move a 12 Gyr isochrones with $[\text{Fe}/\text{H}] = -2$ to lower temperatures and higher gravities. These changes in T_{eff} and $\log g$ would impact the Fe I and Fe II line abundances, and move Fe I closer to Fe II, providing a possible resolution to our results. It is not clear

how/if this effect is incorporated into the MB2020 calibrations, but regardless, this chemical effect will make any calibrations of the stellar parameters of old, metal-poor upper RGB stars subject to larger uncertainties. We note that our upper RGB stars do show a significant range in $[\text{Mg}/\text{Fe}]_{\text{RGB}} = +0.1$ to $+0.8$, with $\sigma[\text{Mg}/\text{Fe}] = 0.1$ to 0.4 . We also notice that the offsets from $\text{Fe I} = \text{Fe II}$ are small for our stars on the lower RGB and seem to rise on the upper RGB, consistent with the predictions from the chemically-dependent isochrone analysis. Regardless of these observations, we do not attempt a purely spectroscopic analysis of the stellar parameters for our RGB stars since we have very few Fe II lines (< 5) in these GRACES spectra.

The other iron-group elements Cr and Ni were also synthesized, but only 1-4 spectral lines of each element are available in our GRACES spectra. Their abundances are provided in Table B5 and shown in Fig. 9. When Cr or Ni are calculated, their 1DLTE abundances are in excellent agreement with Fe, which is similar to other metal-poor stars in the Galaxy. Examination of the NLTE corrections suggests that $[\text{Cr}/\text{Fe}]$ may be increase by up to ~ 0.4 . This would be important for the detailed interpretation of the chemistry of each star; however, we do not include the NLTE effects in Fig. 9 since the Galactic comparison stars are not also corrected.

5.2 Carbon

As the GRACES spectra are restricted to redder wavelengths, we do not have any carbon features to analyse. However, $[\text{C}/\text{Fe}]$ is determined in the FERRE analysis of our MRS from the G-band and features below 4300 \AA . In Table B2, we identify our targets that were reported to have C-enhancements by Aguado et al. (2019). A total of eight of the 30 stars in our sample were identified by FERRE to have $[\text{C}/\text{Fe}] > +1.0$ (P016+28, P021+29, P113+45, P133+28, P184+01, P188+00, P224+02, P339.1+25.5). Unfortunately, the FERRE pipeline struggles to determine C when the SNR of the MRS is low (≤ 25) in the temperature range of our targets. Closer inspection of the MRS shows that five of these are likely upper limits to non-existent G-bands.

Only three stars appear to have noticeable G bands in the MRS spectra, and in each of these cases the FERRE analysis found them to be very carbon-rich, with $[\text{C}/\text{Fe}] > +2$ (P016+28, P184+01, P224+02). Only P016+28 is flagged to have a reliable carbon abundance. The other two do appear to be C-enhanced, but their specific $[\text{C}/\text{Fe}]$ values are quite uncertain. The slight changes in our stellar parameters from the MB2020 calibrations/SB law are also likely to affect the final C abundances.

In summary, we find the C abundances for most of our targets are not sufficiently reliable from the MRS analysis; nevertheless, one star is clearly C-rich (P016+28), and two others are very likely C-enhanced (P184+01, P224+02).

5.3 Alpha elements

Alpha elements in extremely metal-poor stars form primarily through He-capture during various stages in the evolution of massive stars, and dispersed through SNe II events. Thus, the $[\alpha/\text{Fe}]$ ratio is a key tracer of the relative contributions of SN II to SN Ia products in a star forming region. In this paper, the α -elements include Na, Mg, Ca, and Ti. We have included Na because it typically scales linearly with Mg in metal-poor stars in the Galaxy (e.g., Pilachowski et al. 1996; Venn et al. 2004; Norris et al. 2013). We have also included Ti since it too scales with other α -elements even though the dominant

⁷ INSPECT NLTE corrections are available at <http://inspect-stars.net>.

⁸ MPIA NLTE corrections are available at <http://nlte.mpia.de>.

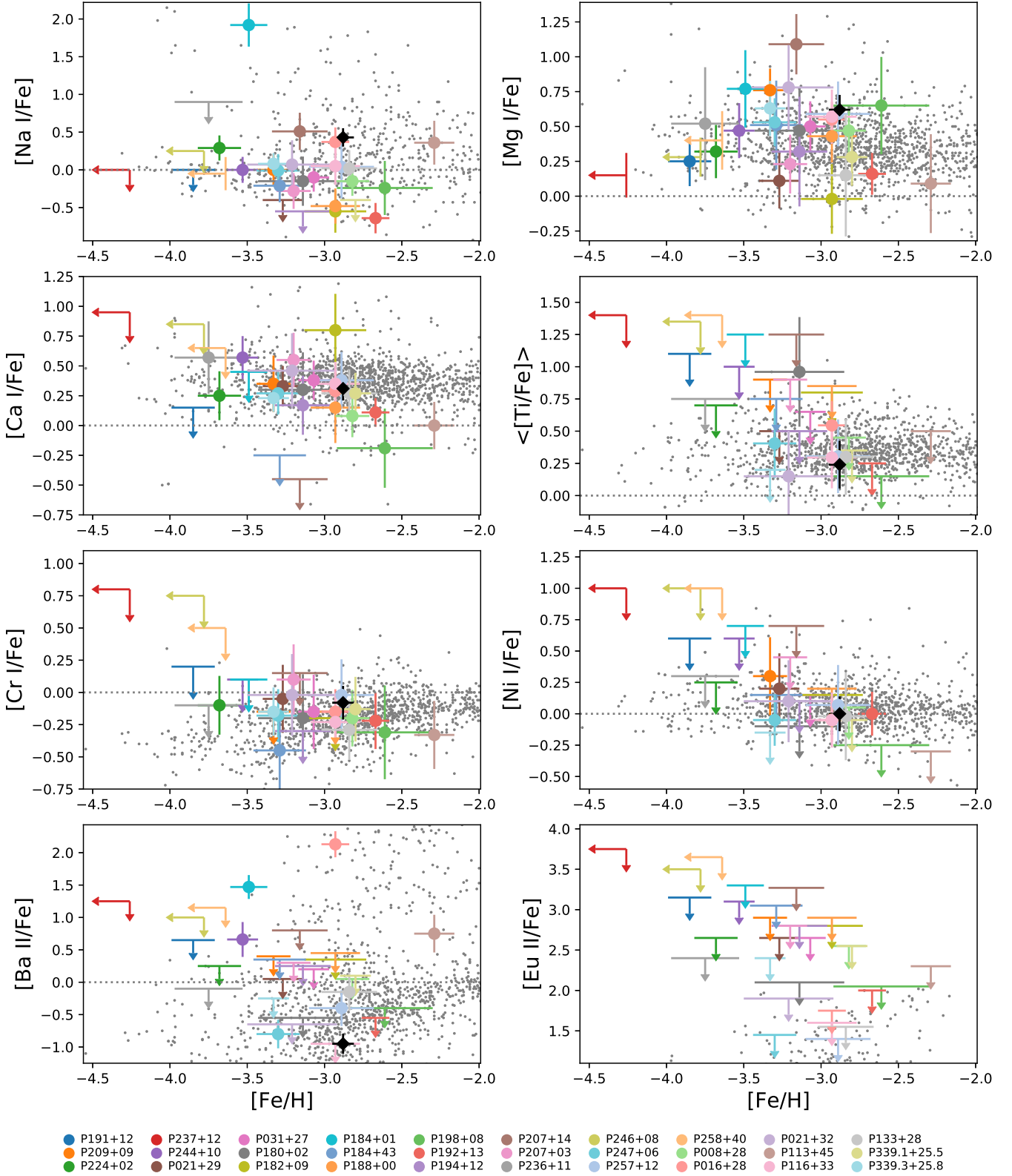


Figure 9. Elements with good spectral line detections, and Eu II . $\langle [\text{Ti}/\text{Fe}] \rangle$ is the average of $[\text{Ti I}/\text{Fe}]$ and $[\text{Ti II}/\text{Fe}]$ when a detection was made for both species, otherwise it is the highest upper limit between the two species. Our analysis of the GRACES spectrum for HD 122563 is shown as the black diamond. The Galactic reference star abundances are taken from the literature (Venn et al. 2004; Aoki et al. 2013; Yong et al. 2013a; Roederer et al. 2014; Frebel et al. 2014).

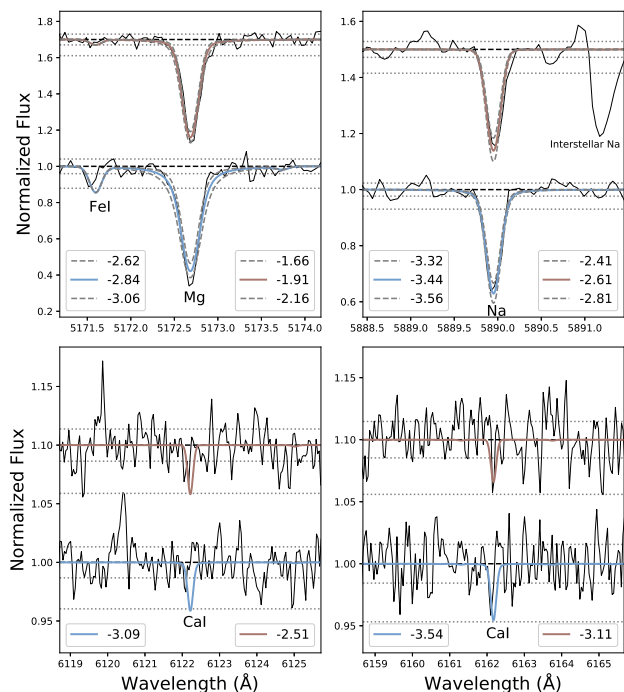


Figure 10. Spectrum syntheses for two stars near $[\text{Fe}/\text{H}] = -3$ that are notably Mg-rich, but Ca-poor. Syntheses of the Mg I 5172.68 Å and Na I 5889.95 Å (top panels), and two Ca I lines (6122.21 Å, 6162.17 Å; bottom panels) are shown, for P207+14 (brown, top) and P184+43 (blue, bottom). These absorption lines provide the best abundances or the tightest constraints for these two stars. The GRACES spectra are the solid black lines, and the synthesized spectra are the solid coloured lines with the $[\text{X}/\text{H}]$ measurements in the legend. Spectra are offset for clarity. Dashed grey lines represent the $\pm 1\sigma$ synthesis. The dashed black line represents the continuum placement and the dotted grey lines are $\pm 1\sigma$ and -3σ , where σ is defined as the measured scatter in the continuum.

isotope ^{48}Ti forms primarily through Si-burning in massive stars (e.g., Woosley et al. 2002).

Na abundances or upper limits are from the two strong Na D lines. These lines are clear and present in most of the stars in our sample, and easily separated from any interstellar lines. NLTE effects can be significant for these resonance lines, however corrections in this analysis are small (ranging from $\Delta(\text{Na}) = -0.1$ to -0.2 for most stars), as shown in Table B14. Mg is from 2-4 lines of Mg I in all stars, even P237+12 which has only an iron upper-limit. NLTE corrections are small (typically $\Delta\text{Mg} \leq +0.2$). Ca is from 1-10 lines of Ca I in most stars, or the Ca I 6122.217 and Ca I 6162.173 lines are used to estimate an upper limit (e.g., see Fig. 10). NLTE corrections are moderate (typically $\Delta\text{Ca} \leq +0.3$). The Ca II triplet is also examined, however we do not use those results in our analysis (especially without NLTE corrections). Ti is from 1-4 lines of Ti I and 1-6 lines of Ti II. For many stars, upper limits only were available and estimated from Ti I lines. The average NLTE corrections for Ti I can be large ($\Delta\text{Ti} \leq +0.6$), however the NLTE corrections to Ti II are negligible. Again, we do not include the NLTE corrections in Fig. 9 since abundances for the Galactic comparison stars are not also corrected.

The majority of these newly discovered extremely metal-poor stars show 1DLTE abundances that are within 1σ uncertainties of the Galactic comparison stars, especially given our results for the

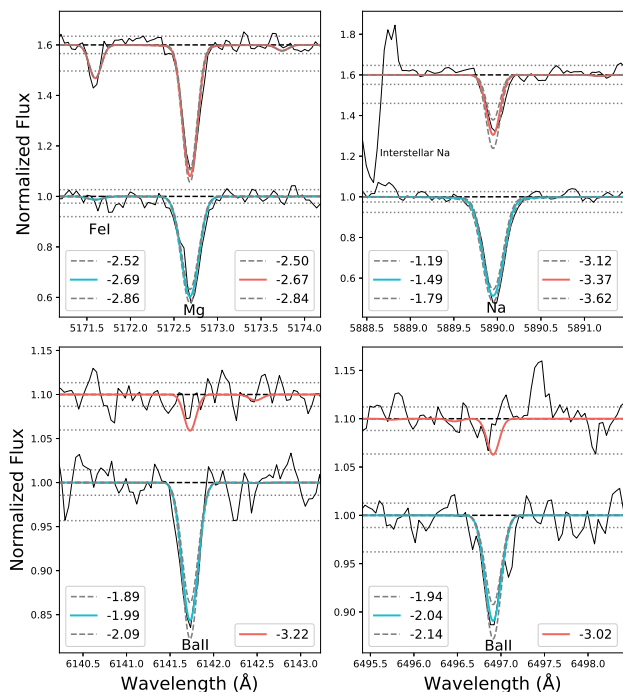


Figure 11. Spectrum syntheses for one Ba-rich star (P184+01, blue) and one Ba-poor star (P192+13, red). Our spectrum syntheses for the two Ba II lines (6141.73 Å, 6496.91 Å) are shown (bottom panels), and our best fit syntheses for Mg I 5172.68 Å and Na I 5889.95 Å (top panels) for comparison. See Fig. 10 for additional label information.

EMP standard star, HD 122563 (black point in each abundance plot). Only a handful of stars have α -element abundances that are statistically lower than the Galactic comparison stars. These include;

(i) Two stars with $[\text{Fe}/\text{H}] < -3$ (P184+43 and P207+14), and a third star near $[\text{Fe}/\text{H}] = -2.6$ (P198+08), show sub-solar $[\text{Ca}/\text{Fe}]$. This is an unusual abundance signature when compared with the Galactic halo sample, especially as all three are enriched in $[\text{Mg}/\text{Fe}] (> +0.5)$. Sample spectra and our 1DLTE synthesis for lines of Mg I, Na I, and Ca I are shown in Fig. 10. NLTE corrections are small and do not affect these trends (see Table B14). This abundance pattern has been seen in only a few EMP stars (see Sitnova et al. 2019), and is discussed further below.

(ii) One star near $[\text{Fe}/\text{H}] = -3$ (P182+09) shows a low, solar-like $[\text{Mg}/\text{Fe}]$ value, yet high values of $[\text{Ca}/\text{Fe}] \sim +0.8$. This pattern has been seen for stars in dwarf galaxies, and is typically attributed to an effectively truncated upper IMF, loss of gas from high mass supernova events, and/or inhomogeneous mixing of supernova yields in the dwarf galaxy's interstellar medium (e.g., Tolstoy et al. 2009; McWilliam et al. 2013; Kobayashi et al. 2015; Frebel & Norris 2015).

(iii) One star near $[\text{Fe}/\text{H}] = -3.5$ (P184+01) shows an enrichment in $[\text{Na}/\text{Fe}]$. This star will be discussed further below (see Section 6.1).

Oxygen is examined from the O I 7770 Å triplet feature, however this resulted in upper limit abundances for most of our stars (see Appendix A. Oxygen could be measured in only six stars, and NLTE corrections were applied (see Table B14. Three stars (P116+33, P198+08, and P339.1+25.5), showing $[\text{O}/\text{Fe}] \sim +0.5$, consistent with $[\text{Mg}/\text{Fe}]$ after oxygen NLTE corrections are applied. Three

other stars (P184+01, P207+14, P224+02) show $[O/Fe] > +1.5$, which is much higher than the other α -elements in those stars. We note that two of these stars are CEMP (Section 5.2 and the third is one of our high $[Mg/Ca]$ stars. The other CEMP and high $[Mg/Ca]$ stars in our sample have high $[O/Fe]$ upper limits only that do not constrain oxygen. These oxygen abundances support our identifications above that these are stars of special interest.

5.4 Neutron-capture elements

Elemental abundances or upper limits are determined for six neutron capture elements: Y, Zr, La, Nd, Ba, and Eu. These formed in massive stars and core collapse supernovae through rapid neutron capture reactions, and those other than Eu also form via slow neutron captures during the thermal pulsing AGB phase in intermediate-mass stars. The specific details and yields from these nucleosynthetic processes is a dynamic field of current research. For the core collapse SNe, new models and calculations of their yields include details of the SN explosion energies, explosion symmetries, early rotation rates, and metallicity distributions (e.g., Kratz et al. 2007; Nishimura et al. 2015; Tsujimoto & Nishimura 2015; Kobayashi et al. 2020), as well as exploration of contributions from compact binary mergers as a (or as the most) significant site for the r-process (e.g., Fryer et al. 2012; Korobkin et al. 2012; Côté et al. 2016; Emerick et al. 2018). Similarly, predictive yields from AGB stars by mass, age, metallicity distributions, and details of convective-reactive mixing are also an active field of research (e.g., Lugaro et al. 2012; Cristallo et al. 2015; Pignatari et al. 2016).

Only Ba and Eu are discussed in this section. For all stars, we have 1-2 Ba II lines (6141.73 Å, 6496.91 Å). Hyperfine structure and isotopic splitting are taken into account using the atomic data in *linemake*. For Eu, the GRACES spectra only permit studies of the Eu II 6645 Å line, which is too weak to be observed in any of our spectra. The upper limits for Eu from this line are also too high to be scientifically useful in testing for pure r-process enrichment in these stars. It would be important to examine the much stronger Eu II 4129 Å line to constrain the pure r-process contributions in these stars.

Two stars appear to be Ba-rich (P184+01 and P016+28); as seen in Fig. 9, both appear to have $[Ba/Fe] \sim +1$ with $[Fe/H] \lesssim -3$. The spectrum synthesis of the two Ba II lines in P184+01 is shown in Fig. 11, where it is clear that these lines are clear, strong, and well measured. NLTE corrections were calculated for these two Ba-rich stars following the methods in Mashonkina et al. (1999) and Mashonkina & Belyaev (2019), using models representing their specific stellar atmospheres and high LTE Ba abundances. The NLTE corrections for P184+01 increase $[Ba/Fe]$ by 0.09 dex, when averaged between the individual corrections for each of the two lines (6141 and 6496 Å). Alternatively, $[Ba/Fe]$ decreases by 0.44 dex when NLTE corrections are calculated for P016+28. Including these corrections, the NLTE Ba abundances are still significantly higher than the 1DLTE results in similar EMP stars in the Galaxy.

Six of our stars appear to be Ba-poor (Fig. 9). The spectrum synthesis for P192+13 shows that the Ba II 6141 and 6497 Å lines are not present (Fig. 11). Using the $3\text{-}\sigma$ line depth, we find upper limits of $[Ba/Fe] < -0.4$ near $[Fe/H] = -2.6$. For our six Ba-poor stars, the $[Ba/Fe]$ abundances and upper limits are within the lower envelope of Ba abundances for stars in the Galaxy.

The other neutron capture elements with spectral features in the GRACES wavelength regions are examined in Appendix A2. Only upper limits could be determined, and they did not provide useful scientific constraints.

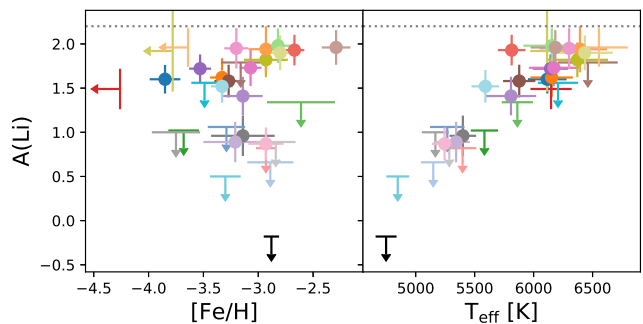


Figure 12. Lithium abundances from Li I 6707 Å. Stellar labels are the same as in Fig. 9. The Spite plateau (Spite & Spite 1982; Sbordone et al. 2010) is shown as the dashed gray line.

5.5 Lithium

The Li I 6707 spectral line is present in the spectra of over half of our targets. Our spectrum syntheses for Li included hyperfine structure and isotopic splitting, with atomic data taken from *linemake*. The study of lithium in EMP stars is an active topic of discussion due to the links between EMP stars and the chemistry of the early Universe. The cosmological lithium problem refers to the discrepancy between the amount of Li predicted from Big Bang nucleosynthesis ($A(\text{Li}) = 2.67$ to 2.74 ; Cyburt et al. 2016; Coc & Vangioni 2017) and the highest Li abundances measured in the atmospheres of unevolved metal-poor stars ($A(\text{Li}) \sim 2.2$, the Spite Plateau; Spite & Spite 1982; Bonifacio et al. 2007; González Hernández et al. 2008; Aoki et al. 2009; Sbordone et al. 2010). Finding unevolved EMP stars with detectable Li provides strong constraints on the lithium problem.

A majority of our sample shows expected trends between $A(\text{Li})$, T_{eff} , and metallicity (Fig. 12). Most of the hotter and higher metallicity stars are found near the Spite plateau. As metallicity decreases, a higher degree of scatter in $A(\text{Li})$ is observed, consistent with the meltdown of the Spite plateau observed by Sbordone et al. (2010); Bonifacio et al. (2012). The RGB stars in our sample show lower lithium abundances (or upper limits), as expected since Li is destroyed through surface convection in cooler stars (Spite & Spite 1982). Five stars, however, are notable: P191+12, P224+10, P237+12, P246+08, P258+40. P191+12 and P224+10 have metallicities of $[Fe/H] = -3.85$ and -3.68 , respectively, and the other three stars only have metallicity upper-limits with $[Fe/H] < -3.5$, but all four have detectable Li at the 3σ level. Their measured $A(\text{Li})$ places them at the Spite plateau (see Table B7). Similar in T_{eff} , $\log g$, metallicity, and $A(\text{Li})$ to the primary star of the spectroscopic binary CS22876-032 (González Hernández et al. 2008, 2019), these main-sequence and turn-off stars are excellent candidates for follow-up studies related to the cosmological lithium problem.

6 DISCUSSION

Using the chemical abundances determined in this paper, we discuss our EMP stars in terms of the accretion history and chemical evolution of the Galaxy.

6.1 New CEMP candidates

In this paper, we have analysed three stars with slight to large carbon enhancements. As their precise $[C/Fe]$ results are quite uncertain, we regard these stars simply as carbon-enhanced metal-poor

(CEMP) candidates, rather than confirmed CEMP stars. At the lowest metallicities, stars are often found to be enhanced in carbon (Beers et al. 1992; Norris et al. 1997), typically comprising 40% of the EMP stars (see Yong et al. 2013b; Lee et al. 2013; Placco et al. 2014), though recently those percentages have been lowered through considerations of the carbon 3DNLTE corrections (Norris & Yong 2019).

Different types of CEMP stars have been identified and defined by Beers & Christlieb (2005), where the two main classes are the CEMP-s stars, which show additional enhancement in s-process elements (such that $[C/Fe] > +0.7$ and $[Ba/Fe] > +1.0$), and the CEMP-no stars, which do not show any s-process enhancements. These initial definitions have been further refined by Yoon et al. (2016), based on the trends observed between $[Fe/H]$ and $[C/Fe]$. The C excess in CEMP-no stars is generally attributed to nucleosynthetic pathways associated with the very first stars to be born in the universe (Iwamoto et al. 2005; Meynet et al. 2006).

Of our three new CEMP candidates, we find that two (P016+28 and P184+01) are enriched in barium, with $[Ba/Fe] > +1$ (to within their 1σ uncertainties), which suggests that they may belong to the CEMP-s sub-class. Examining P016+28 further, the carbon abundance from FERRE is $[C/Fe] = +2.42$, for an absolute carbon abundance of $A(C) = 7.76$. If this carbon abundance is accurate, this star would be amongst the high-C/Group I population in Yoon et al. (2016, $A(C) = 7.96 \pm 0.42$). Meanwhile, P184+01 has $[Fe/H] = -3.49$ and a very uncertain carbon abundance of $A(C) = 7.26$, which places it between Groups I, II, and III. Another way to test the CEMP-s hypothesis for these two stars is through radial velocity monitoring, as most CEMP-s stars are found in a binary systems (e.g., Lucatello et al. 2005; Hansen et al. 2016; Starkenburg et al. 2014, and references therein). This property has contributed to the theory that CEMP-s stars have received their carbon and s-process enhancements through mass-transfer with an asymptotic giant branch (AGB) star in a binary system (Abate et al. 2013). We do not search for radial velocity variations in our data though, since the GRACES spectra were rarely taken over several epochs, and the medium-resolution INT spectra do not have sufficient precision.

The remaining CEMP-no candidate, P224+02, has a low barium upper-limit. As this star has $[Fe/H] = -3.68$ (and a tentative $A(C) = 7.29$), it falls between the $A(C)$ -metallicity groups in Yoon et al. (2016). Groups II and III are dominated by CEMP-no stars, but recent analysis of Group I CEMP stars has shown that 14% are CEMP-no (Norris & Yong 2019). While generally low in s-process elements, the Group I CEMP-no stars also show higher $[Sr/Ba]$ abundances than the majority of Group I CEMP-s/rs stars. To explain the $[Sr/Ba]$ ratios, Norris & Yong (2019) speculated that Group I CEMP-no stars may experience some mass exchange with massive AGB stars or rapidly-rotating "spinstars" in binary systems (both produce less s-process material). Unfortunately, we do not determine $[Sr/Fe]$ as the Sr II lines are at blue wavelengths, not reached by our GRACES spectra. Alternatively, we examine the α -elements (Na, Mg, Ca) since some CEMP-no stars can show enrichments in these elements; P224+02 shows normal halo abundances for these elements. As discussed by Maeder & Meynet (2015), the predictions for these elements depend on mixing in massive stars though, and the predictions can vary widely. Frebel & Norris (2015) showed that enhanced alpha-elements only occur in about half of their CEMP-no sample, and even less when $[Fe/H] \lesssim -3$.

The exact origin(s) of the CEMP-no stars is not yet clear, however it has also been proposed that CEMP-no stars may form in dwarf galaxies, and thereby may be associated with accreted

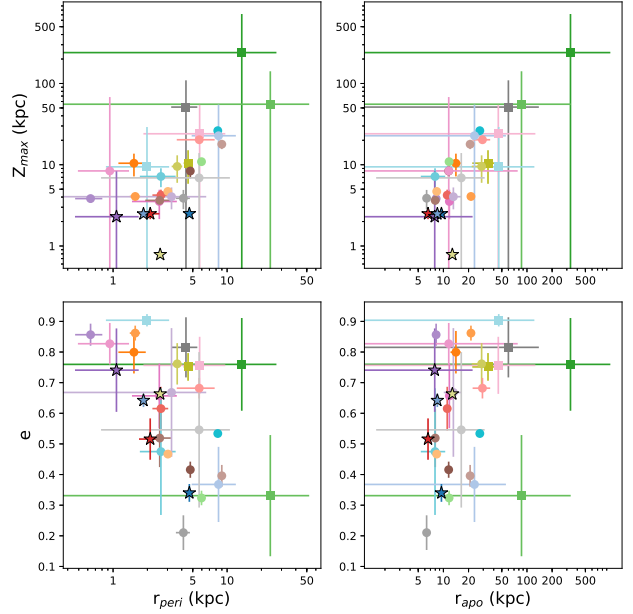


Figure 13. Orbital elements for stars from 2018A-2019B datasets. Star symbols represent stars in planar disk orbits, squares are stars that reach the outer Galactic halo.

systems (Yuan et al. 2020; Limberg et al. 2020). To examine this further, we compute the orbits of our 30 GRACES stars below.

6.2 Other stars with interesting chemistries

Highlighted in Section 5.3, three stars (P184+43, P198+08, and P207+14) show very low $[Ca/Fe] (\leq -0.3)$ and large $[Mg/Fe] (> +0.5)$. This results in $[Mg/Ca] \gtrsim +0.8$. This rare abundance pattern had been seen in only a few EMP stars, e.g., one star (HE1424-0241) at $[Fe/H] = -4$ was highlighted by Cohen et al. (2007) for its high $[Mg/Ca] = +0.83$, mostly driven by its low Ca. This abundance pattern cannot be explained by uncertainties in the stellar parameters (including any possible systematic errors in the surface gravity, e.g., if these were on the horizontal branch); instead, it is interpreted as contributions to stellar Mg and Ca abundances from only a small number of SN II explosions, i.e., where the nucleosynthetic yield for explosive alpha-burning nuclei like Ca was very low compared to that for the hydrostatic alpha-burning element Mg (see Sitnova et al. 2019). These results are further supported by our high $[O/Fe]_{NLTE}$ values (see Appendix A).

Two similar stars in the Hercules dwarf galaxy with $[Mg/Ca] = +0.58$ and $+0.94$ dex were studied by Koch et al. (2008). Koch et al. (2008) argued that such high ratios can be attributed to enrichment from high mass ($\sim 35M_{\odot}$) Type II SNe, based on yields from Woosley & Weaver (1995). Furthermore, their chemical evolution models for Hercules-like dwarf galaxies indicate that the observed $[Mg/Ca]$ ratios can only be reproduced in 10% of the systems that are enriched by only a few (1-3) Type II events. Clearly these are chemically unique objects which reflect the chemical evolution of rare environments. Sitnova et al. (2019) also note that these exceptional stars comprise $<10\%$ of stars with $[Fe/H] < -3$ and do not typically reveal carbon enhancement, consistent with our results.

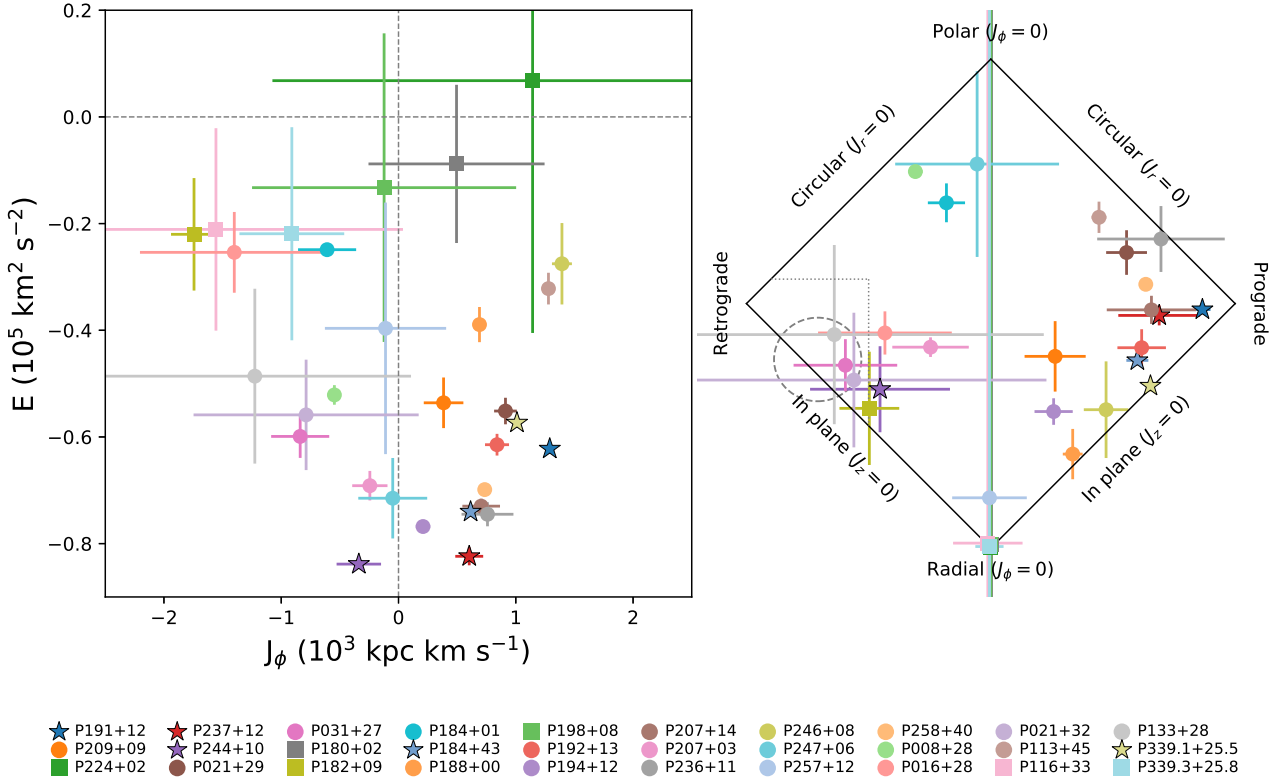


Figure 14. Action vectors and energies for stars from 2018A-2019B datasets. Same symbols as in Fig. 13. The dotted grey box in the right panel is the dynamical cut for Gaia-Sequoia from Myeong et al. (2019) ($e \sim 0.6$ with $J_\phi/J_{tot} < -0.5$ and $(J_z - J_R)/J_{tot} < 0.1$) and the dashed grey ellipse represents the mean dynamical properties of the associated Gaia-Sequoia stars from Limberg et al. (2020).

6.3 Orbit calculations

Gaia DR2 proper motions and astrometry have dramatically accelerated the fields of Galactic Archaeology and near-field cosmology by providing the data needed to calculate the detailed orbits of nearby stars. The stars in this study were also selected to have small parallax errors, and therefore precise distances. When combined with the precision radial velocities from our high-resolution GRACES spectra, then we are able to estimate the orbits for these stars to within the accuracy of our assumptions on the MW potential.

Orbital parameters for the stars in this paper are calculated with *Galpy* (Bovy 2015), using the parallax distances, our radial velocities from the GRACES spectra, and the *Gaia* DR2 proper motions. The *MWPotential14*⁹ was adopted, though a more massive halo of $1.2 \times 10^{12} M_\odot$ was chosen following Sestito et al. (2019). Errors have been propagated from the uncertainties in the proper motions, RVs, and distances via Monte-Carlo sampling of the Gaussian distributions of the input quantities.

The apocentric and pericentric distances (R_{apo} and R_{peri}), perpendicular distance from the Galactic plane (Z_{max}), and eccentricity (e) of the calculated orbits for our stars are shown in Fig. 13. Following Sestito et al. (2019), stars with $R_{apo} < 15$ kpc and $|Z|_{max} < 3$ kpc are considered to be confined to the Galactic plane, while stars with $R_{apo} > 30$ kpc are considered to be members of the outer halo. The

orbital energy (E) and action parameters (vertical J_z , azimuthal J_ϕ) for the sample are also calculated with *Galpy*, and shown in Fig. 14. All targets appear to be bound to the Milky Way, to within their uncertainties.

6.4 Stars with Interesting Orbits

Five of our new EMP stars (P184+43, P191+12, P237+12, P244+10, and P339.1+25.5) have distinctly planar-like orbits ($|Z|_{max} < 3$ kpc). All five have $[\text{Fe}/\text{H}] < -3$ and somewhat elliptical orbits ($e = 0.3$ to 0.7). P237+12 is the most metal-poor star in the GRACES sample with a 1DLTE metallicity upper-limit of $[\text{Fe}/\text{H}] < -4.26$. This star has Mg below the canonical MW halo plateau values, though the abundances, when available, are generally within the regime of normal Galactic halo stars. The implications of finding planar-like EMP stars, in the context of Galactic evolution, is discussed further in the following section. P339.1+25.5 stands out dynamically as it has the lowest $|Z|_{max}$ (< 1 kpc) of the stars in this sample, suggesting it may be coincident with the prograde Galactic thin disk. However, its somewhat elliptical orbit ($e \sim 0.7$) is uncharacteristic of typical thin disk stars.

The star P184+43 with a prograde, planar orbit also has an unusual chemistry, as it is enriched in magnesium, $[\text{Mg}/\text{Fe}] = +0.6$, and yet has a very low upper-limit on calcium, $[\text{Ca}/\text{Fe}] < -0.2$. In Section 6.2, we speculated that this peculiar abundance pattern may suggest a lack of contributions from lower mass stars and SN Ia. If so, then this star could have formed in a dwarf galaxy that was

⁹ This potential is three component model composed of a power law, exponentially cut-off bulge, Miyamoto Nagai Potential disc, and Navarro, Frenk & White (1997) dark matter halo.

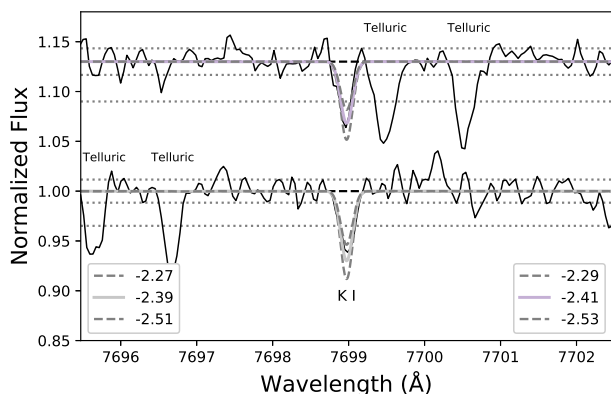


Figure 15. Syntheses of K I at 7698.97 Å. P133+28 (light grey, bottom) and P021+32 (light purple, top). Both objects are K-rich (e.g. Fig. A2) and appear to be dynamically related to the Gaia-Sequoia accretion event (e.g. Fig. 14). Telluric absorption lines are identified, however telluric subtraction was not performed as no spectral standards were observed in tandem with these science acquisitions. See Fig. 11 for additional label information.

accreted by the Milky Way at early times, before SN Ia could enrich it. This speculation is discussed further below (Section 6.5).

Five high-energy, highly-retrograde stars (P016+28, P021+32, P031+27, P133+28, P182+09) appear to be dynamically related to the “Gaia-Sequoia” accretion event (Myeong et al. 2019). Sequoia is the population of high-energy retrograde halo stars that are presumed to be associated with an ancient accretion event of a counter-rotating progenitor dwarf galaxy (Myeong et al. 2019; Matsuno et al. 2019; Monty et al. 2020; Cordoni et al. 2021; Yuan et al. 2020; Limberg et al. 2020). Myeong et al. (2019) identifies stars with $e \sim 0.6$, $J_\phi/J_{tot} < -0.5$, and $(J_z - J_R)/J_{tot} < 0.1$ to be linked to Gaia-Sequoia. These five stars also meet the more recent and stricter membership criteria by Limberg et al. (2020, see Fig. 14), to within their errors. We acknowledge that these simple action vector cuts do not account for background stars which are non-coincident with Sequoia. Limberg et al. (2020) explored the effect of background contamination via a membership clustering algorithm and found that up to $\sim 50\%$ of their Sequoia sample may indeed be contamination. Due to the small size of our sample, we do not explore this further and only offer these stars as Gaia-Sequoia candidates to be confirmed/rejected in later studies. We note that all five have $[\text{Fe}/\text{H}] \sim -3$, and normal halo $[\alpha/\text{Fe}]$ ratios. These add to the few extremely metal-poor stars now found associated with Gaia-Sequoia (see also Monty et al. 2020; Cordoni et al. 2021; Limberg et al. 2020).

The action vectors computed for the orbit of P244+10 suggests that it may also be associated with Gaia-Sequoia; however, its low energy planar-like orbit is uncharacteristic of other Sequoia members. P244+10 is more dynamically similar to stars associated with the Thamnos event (Helmi et al. 2017; Koppelman et al. 2018; Limberg et al. 2020). Thamnos is also believed to be a lower metallicity - higher α -abundance population than Gaia-Sequoia (Koppelman et al. 2018; Monty et al. 2020; Limberg et al. 2020), and our chemical abundance study would support that. We find P244+10 has $[\text{Fe}/\text{H}] = -3.5 \pm 0.3$, compared to the five Gaia-Sequoia targets (above) with $\langle [\text{Fe}/\text{H}] \rangle = -3.0 \pm 0.2$, and highlight that P244+10 is an interesting star for follow-up investigations.

6.5 Formation and Early Chemical Evolution of the Galaxy

This work is consistent with the results by Sestito et al. (2019) who found that a large number of ultra metal-poor stars in the literature are on planar orbits in the Galaxy. We have found five new EMP stars on planar-like orbits (or 16% of our sample). Four are on prograde orbits and one (P244+10) is on a retrograde orbit. These ratios are comparable to our earlier results from an analysis of CFHT spectra for 115 metal-poor candidates which resulted in 16 very metal-poor stars ($[\text{Fe}/\text{H}] < -2.5$) confined to the Galactic plane ($R_{\text{apo}} < 15$ kpc, $Z_{\text{max}} < 3$ kpc), including one on an extremely retrograde orbit (Venn et al. 2020). In comparison with the larger *Pristine* database of medium-resolution INT spectra, Sestito et al. (2020) found that the ratio of metal-poor stars ($[\text{Fe}/\text{H}] < -2.5$) with prograde versus retrograde orbits is 1.28, based on 358 stars. We find a similar ratio of 1.23, for our sample of 29 stars with $[\text{Fe}/\text{H}] < -2.5$. When compared to the Numerical Investigation of a Hundred Astronomical Objects (NIHAO Wang et al. 2015) hydrodynamic simulations of galaxy formation, specifically the NIHAO-UHD simulations (Buck 2020), these simulations show that such a population of stars is ubiquitous among these Milky Way-like galaxies as investigated by Sestito et al. (2021).

In Section 6.2, we speculated that P184+43, with its planar orbit and unusual chemistry ($[\text{Mg}/\text{Ca}] > +0.8$), may have formed in a dwarf galaxy that was accreted at early times. The age estimate is based on its low metallicity $[\text{Fe}/\text{H}] = -3.3 \pm 0.3$ and chemical pattern, which suggests a lack of contributions from lower mass stars and SN Ia. It is possible that this star and its host dwarf galaxy were amongst the original building blocks that formed the proto Milky Way, as suggested from an analysis of NIHAO hydrodynamic simulations by Sestito et al. (2021).

The chemistry of the Gaia-Sequoia candidates P016+28, P021+32, and P031+27 are largely consistent with previous studies, which show typical α -enhancement at low metallicities (Matsuno et al. 2019; Monty et al. 2020; Limberg et al. 2020; Yuan et al. 2020). Cordoni et al. (2021) find that this α -abundances pattern span a metallicity range from $-3.6 < [\text{Fe}/\text{H}] < -2.4$. However, amongst our two other Gaia-Sequoia candidate stars, P133+28 and P182+09, the former shows low $[\text{Mg}/\text{Fe}]$ and $[\text{Ca}/\text{Fe}]$, whereas the latter has solar-like $[\text{Mg}/\text{Fe}]$ and enriched $[\text{Ca}/\text{Fe}]$, such that P182+09 has $[\text{Mg}/\text{Ca}] = -0.8$. Monty et al. (2020) also found one Gaia-Sequoia candidate (G184-007) with low $[\text{Mg}/\text{Fe}]$ and $[\text{Ca}/\text{Fe}]$ though at a much higher metallicity ($[\text{Fe}/\text{H}] = -1.67$ for G184-007 vs. $[\text{Fe}/\text{H}] = -2.84$ and -2.93 for P133+28 and P182+09, respectively). If the location of the “knee” in the $[\text{Mg}/\text{Fe}]$ vs. $[\text{Fe}/\text{H}]$ plane, as identified by Monty et al. (2020) at $[\text{Fe}/\text{H}] = -1.6$ or -2.3 , is an accurate reflection of the chemical evolution of Gaia-Sequoia, then our low $[\text{Mg}/\text{Fe}]$ ratios in P133+28 and P182+09 would be difficult to reconcile. Either they are not Gaia-Sequoia members, or alternatively, if Gaia-Sequoia had episodes of star formation that stochastically enriched its interstellar medium, there could be a range in elements like Mg. Similar abundance patterns have been seen in EMP stars in dwarf galaxies, such as Carina and Sextans (Norris et al. 2017; de Boer et al. 2014; Theler et al. 2020; Lucchesi et al. 2020). Furthermore, two of our Gaia-Sequoia candidates (P021+32 and P133+28) may be enriched in potassium (see Figs. 15 and A2). An anti-correlation of stars that are Mg-poor but K-rich was discovered in the outer globular cluster NGC 2419 (Cohen et al. 2011; Cohen & Kirby 2012). This describes P133+28 well, though our Mg abundance for P021+32 is quite high and would not fit this pattern well. Other elements (Sc, and to a lesser extent Si and Ca) also showed variations, such that a more detailed analysis of these two Gaia-Sequoia candi-

dates, especially with broader spectra that can reach more elements, would be interesting.

Finally, one of our new CEMP candidates, P016+28, appears to be *dynamically* associated with the Gaia-Sequoia event. We note that Yuan et al. 2020 identify one CEMP-no candidate with Gaia-Sequoia (CS29514-007, from Roederer et al. 2014). CS29514-007 ($[\text{Fe}/\text{H}] = -2.8$) has a similar metallicity to P016+28 ($[\text{Fe}/\text{H}] = -2.93 \pm 0.20$), but significantly different barium (CS29514-007 has $[\text{Ba}/\text{Fe}] \sim 0$, whereas we find P016+28 is rich in neutron-capture elements (Ba, La, Nd) by $\geq +1.5$; see Appendix A2). It would be interesting if these two stars probe the most metal-poor regime of their (former) host and could constrain its early chemical evolution,

7 CONCLUSIONS

We present detailed spectral analyses for 30 new metal-poor stars found within the Pristine survey and followed-up with Gemini GRACES high-resolution spectroscopy. All of these stars were previously observed with INT medium-resolution spectra.

- We confirm that 19 of our targets are EMP with $[\text{Fe}/\text{H}] < -3.0$ (63%), three of which only have iron upper-limits. If we consider their $1\sigma(\text{Fe})$ errors, then we confirm 24 are EMP stars (80%). The most metal-poor star in the sample is P237+12, with $[\text{Fe}/\text{H}] < -4.26$.
- The INT medium-resolution spectra showed that three of our targets may be carbon-enhanced. We find that one is a CEMP-no candidate based on low $[\text{Ba}/\text{Fe}]$ upper-limits, while the other two appear to be CEMP-s candidates.
- Three stars (P184+43, P198+08, and P207+14) are found to be deficient in Ca, yet Mg enriched, yielding $[\text{Mg}/\text{Ca}] \gtrsim +0.8$. This is a rare abundance signature, interpreted as the yields from a small number of SN II that underproduce Ca in explosive alpha-element production compared to Mg from hydrostatic nucleosynthesis.
- Five stars (P184+43, P191+12, P237+12, P244+10, P339.1+25.5) orbit in the Galactic plane, including the most metal-poor star in our sample (P237+12). We suggest they were brought in with one or more dwarf galaxies that were building blocks that formed the Galactic plane. As additional support one of these stars (P244+10) has a retrograde planar orbit. This star overlaps in eccentricity and action with the Gaia-Sequoia accreted dwarf galaxy; however, its low energy and low metallicity ($[\text{Fe}/\text{H}] = -3.5 \pm 0.3$) are in better agreement with the Thamnos event.
- Five stars are new candidates for the accreted stellar population from Gaia-Sequoia, based on their positions in the eccentricity-action-energy phase space (P016+28, P021+32, P031+27, P133+28, and P182+09). We find that P016+28, P021+32, P031+27 are enhanced in Mg and Ca, consistent with previous chemical studies of the Sequoia population; however, P133+28 and P182+09 both show low $[\text{Mg}/\text{Fe}]$. This could imply these stars are non-members; however, it is also possible that Gaia-Sequoia had episodes of star formation that stochastically enriched its interstellar medium. These two stars show different $[\text{Ca}/\text{Fe}]$ from the rest of the population (one is Ca-poor and the other Ca-rich), and two Gaia-Sequoia members P133+28 and P021+32) are enriched in K. Also, we have found that P016+28 is a CEMP-s candidate, showing enhancements of C, Ba, La, and Nd.

This work shows that the Pristine survey has been highly successful in finding new and interesting metal-poor stars, especially when combined with Gaia DR2 parallaxes and proper motions for testing stellar population and galaxy formation models. We look forward to the upcoming large spectroscopic surveys that will be able

to tackle statistically large samples of these metal-poor stars for a detailed chemo-dynamical evaluation of the metal-poor components of our Galaxy.

ACKNOWLEDGEMENTS

We wish to thank the referee Mike Bessell for his expert advice in exploring the stellar parameter determinations for our metal-poor stars. We also wish to thank Keith Hawkins for helpful discussions (and warnings) on systematic errors in stellar spectral analyses and on the chemical evolution of the metal-poor Galaxy.

This work is based on observations obtained with Gemini Remote Access to CFHT ESPaDOnS Spectrograph (GRACES), as part of the Gemini Large and Long Program, GN-X-LP-102 (where X includes semesters 2018B to 2020A), and also the PI Kieley program, GN-2018BA-Q-117. Gemini Observatory is operated by the Association of Universities for Research in Astronomy, Inc., under a cooperative agreement with the NSF on behalf of the Gemini partnership: the National Science Foundation (United States), the National Research Council (Canada), CONICYT (Chile), Ministerio de Ciencia, Tecnología e Innovación Productiva (Argentina), Ministério da Ciência, Tecnologia e Inovação (Brazil), and Korea Astronomy and Space Science Institute (Republic of Korea). CFHT is operated by the National Research Council of Canada, the Institut National des Sciences de l'Univers of the Centre National de la Recherche Scientifique of France, and the University of Hawai'i. ESPaDOnS is a collaborative project funded by France (CNRS, MENESR, OMP, LATT), Canada (NSERC), CFHT, and the European Space Agency. Data was reduced using the CFHT developed OPERA data reduction pipeline.

This work has also made use of data from the European Space Agency mission Gaia (<https://www.cosmos.esa.int/gaia>), processed by the Gaia Data Processing and Analysis Consortium (DPAC, <https://www.cosmos.esa.int/web/gaia/dpac/consortium>). Funding for the DPAC has been provided by national institutions, in particular the institutions participating in the Gaia Multilateral Agreement. This research has made use of use of the SIMBAD database, operated at CDS, Strasbourg, France (Wenger et al. 2000).

This research made use of NASA's Astrophysics Data System, the SIMBAD astronomical database, operated at CDS, Strasbourg, France. This work also made extensive use of Astropy,¹⁰ a community-developed core Python package for Astronomy (Astropy Collaboration et al. 2013, 2018).

CLK and KAV are grateful for funding through the National Science and Engineering Research Council Discovery Grants program and the CREATE training program on New Technologies for Canadian Observatories. ES gratefully acknowledge funding by the Emmy Noether program from the Deutsche Forschungsgemeinschaft (DFG). FS and NFM gratefully acknowledge support from the French National Research Agency (ANR) funded project "Pristine" (ANR-18-CE31-0017) along with funding from CNRS/INSU through the Programme National Galaxies et Cosmologie and through the CNRS grant PICS07708. FS thanks the Initiative d'Excellence IdEx from the University of Strasbourg and the Programme Doctoral International PDI for funding his PhD. This work has been published under the framework of the IdEx Unistra and benefits from funding from the state managed by the

¹⁰ <http://www.astropy.org>

French National Research Agency (ANR) as part of the investments for the future program.

The authors thank the International Space Science Institute (ISSI) in Bern, Switzerland, for providing financial support and meeting facilities to the international team Pristine.

The authors wish to recognize and acknowledge the very significant cultural role and reverence that the summit of Maunakea has always had within the Native Hawaiian community. We are very fortunate to have had the opportunity to conduct observations from this mountain.

DATA AVAILABILITY

The data underlying this article and online supplementary material will be shared on reasonable requests to the corresponding author.

REFERENCES

- Abate C., Pols O. R., Izzard R. G., Mohamed S. S., de Mink S. E., 2013, *A&A*, **552**, A26
- Abel T., Bryan G. L., Norman M. L., 2002, *Science*, **295**, 93
- Aguado D. S., González Hernández J. I., Allende Prieto C., Rebolo R., 2017, *A&A*, **605**, A40
- Aguado D. S., González Hernández J. I., Allende Prieto C., Rebolo R., 2018a, *ApJ*, **852**, L20
- Aguado D. S., Allende Prieto C., González Hernández J. I., Rebolo R., 2018b, *ApJ*, **854**, L34
- Aguado D. S., et al., 2019, *MNRAS*, **490**, 2241
- Andrae R., et al., 2018, *A&A*, **616**, A8
- Aoki W., et al., 2009, *A&A*, **502**, 569
- Aoki W., et al., 2013, *AJ*, **145**, 13
- Arentsen A., et al., 2020a, *MNRAS*, **491**, L11
- Arentsen A., et al., 2020b, *MNRAS*, **496**, 4964
- Asplund M., Grevesse N., Sauval A. J., Scott P., 2009, *ARA&A*, **47**, 481
- Astropy Collaboration et al., 2013, *A&A*, **558**, A33
- Astropy Collaboration et al., 2018, *aj*, **156**, 123
- Barbá R. H., Minniti D., Geisler D., Alonso-García J., Hempel M., Monachesi A., Arias J. I., Gómez F. A., 2019, *ApJ*, **870**, L24
- Beers T. C., Christlieb N., 2005, *ARA&A*, **43**, 531
- Beers T. C., Preston G. W., Shectman S. A., 1985, *AJ*, **90**, 2089
- Beers T. C., Preston G. W., Shectman S. A., 1992, *AJ*, **103**, 1987
- Beers T. C., Rossi S., Norris J. E., Ryan S. G., Shefler T., 1999, *AJ*, **117**, 981
- Belokurov V., Erkal D., Evans N. W., Koposov S. E., Deason A. J., 2018, *MNRAS*, **478**, 611
- Bergemann M., 2011, *MNRAS*, **413**, 2184
- Bergemann M., Cescutti G., 2010, *A&A*, **522**, A9
- Bergemann M., Lind K., Collet R., Magic Z., Asplund M., 2012, *MNRAS*, **427**, 27
- Bergemann M., Collet R., Amarsi A. M., Kovalev M., Ruchti G., Magic Z., 2017, *ApJ*, **847**, 15
- Bond H. E., 1980, *ApJS*, **44**, 517
- Bonifacio P., et al., 2007, *A&A*, **462**, 851
- Bonifacio P., Sbordone L., Caffau E., Ludwig H. G., Spite M., González Hernández J. I., Behara N. T., 2012, *A&A*, **542**, A87
- Bonifacio P., et al., 2018, *A&A*, **612**, A65
- Bonifacio P., Caffau E., Spite M., Spite F., 2019a, *Research Notes of the American Astronomical Society*, **3**, 64
- Bonifacio P., et al., 2019b, *MNRAS*, **487**, 3797
- Bovy J., 2015, *ApJS*, **216**, 29
- Bovy J., Rix H.-W., Schlafly E. F., Nidever D. L., Holtzman J. A., Shetrone M., Beers T. C., 2016, *ApJ*, **823**, 30
- Bromm V., Coppi P. S., Larson R. B., 1999, *ApJ*, **527**, L5
- Buck T., 2020, *MNRAS*, **491**, 5435
- Buzzoni B., et al., 1984, *The Messenger*, **38**, 9
- Caffau E., et al., 2012, *A&A*, **542**, A51
- Caffau E., et al., 2017, *Astronomische Nachrichten*, **338**, 686
- Carney B. W., Peterson R. C., 1981, *ApJ*, **245**, 238
- Carney B. W., Latham D. W., Stefanik R. P., Laird J. B., Morse J. A., 2003, *AJ*, **125**, 293
- Casagrande L., et al., 2014, *MNRAS*, **439**, 2060
- Casagrande L., et al., 2016, *MNRAS*, **455**, 987
- Casagrande L., et al., 2020, arXiv e-prints, p. arXiv:2011.02517
- Chene A.-N., et al., 2014, GRACES: Gemini remote access to CFHT ES-PaDOnS spectrograph through the longest astronomical fiber ever made: experimental phase completed. p. 915147, doi:10.1117/12.2057417
- Choi J., Dotter A., Conroy C., Cantiello M., Paxton B., Johnson B. D., 2016, *The Astrophysical Journal*, **823**, 102
- Christlieb N., Wisotzki L., Graßhoff G., 2002, *A&A*, **391**, 397
- Clark P. C., Glover S. C. O., Klessen R. S., Bromm V., 2011, *ApJ*, **727**, 110
- Clarkson O., Herwig F., Pignatari M., 2018, *MNRAS*, **474**, L37
- Coc A., Vangioni E., 2017, *International Journal of Modern Physics E*, **26**, 1741002
- Cohen J. G., Kirby E. N., 2012, *ApJ*, **760**, 86
- Cohen J. G., McWilliam A., Christlieb N., Shectman S., Thompson I., Melendez J., Wisotzki L., Reimers D., 2007, *ApJ*, **659**, L161
- Cohen J. G., Huang W., Kirby E. N., 2011, *ApJ*, **740**, 60
- Cohen J. G., Christlieb N., Thompson I., McWilliam A., Shectman S., Reimers D., Wisotzki L., Kirby E., 2013, *ApJ*, **778**, 56
- Collet R., Nordlund Å., Asplund M., Hayek W., Trampedach R., 2018, *MNRAS*, **475**, 3369
- Cooke R. J., Madau P., 2014, *ApJ*, **791**, 116
- Cordoni G., et al., 2021, *MNRAS*, **503**, 2539
- Côté B., West C., Heger A., Ritter C., O'Shea B. W., Herwig F., Travaglio C., Bisterzo S., 2016, *MNRAS*, **463**, 3755
- Cristallo S., Straniero O., Piersanti L., Gobrecht D., 2015, *ApJS*, **219**, 40
- Cui X.-Q., et al., 2012, *Research in Astronomy and Astrophysics*, **12**, 1197
- Cyburtt R. H., Fields B. D., Olive K. A., Yeh T.-H., 2016, *Reviews of Modern Physics*, **88**, 015004
- Da Costa G. S., et al., 2019, *MNRAS*, **489**, 5900
- Dalton G., et al., 2014, in *Ground-based and Airborne Instrumentation for Astronomy V*. p. 91470L (arXiv:1412.0843), doi:10.1117/12.2055132
- Dalton G., et al., 2018, in Evans C. J., Simard L., Takami H., eds, *Society of Photo-Optical Instrumentation Engineers (SPIE) Conference Series Vol. 10702, Ground-based and Airborne Instrumentation for Astronomy VII*. p. 107021B, doi:10.1117/12.2312031
- Demarque P., Woo J.-H., Kim Y.-C., Yi S. K., 2004, *ApJS*, **155**, 667
- Di Matteo P., Spite M., Haywood M., Bonifacio P., Gómez A., Spite F., Caffau E., 2020, *A&A*, **636**, A115
- Donati J. F., Catala C., Landstreet J. D., Petit P., 2006, in Casini R., Lites B. W., eds, *Astronomical Society of the Pacific Conference Series Vol. 358, Solar Polarization 4*. p. 362
- Dotter A., 2016, *ApJS*, **222**, 8
- Eisenstein D. J., et al., 2011, *AJ*, **142**, 72
- El-Badry K., et al., 2018, *MNRAS*, **480**, 652
- Emerick A., Bryan G. L., Mac Low M.-M., Côté B., Johnston K. V., O'Shea B. W., 2018, *ApJ*, **869**, 94
- Frebel A., Norris J. E., 2015, *ARA&A*, **53**, 631
- Frebel A., Simon J. D., Kirby E. N., 2014, *ApJ*, **786**, 74
- Frebel A., Ji A. P., Ezzeddine R., Hansen T. T., Chiti A., Thompson I. B., Merle T., 2019, *ApJ*, **871**, 146
- Freeman K., Bland-Hawthorn J., 2002, *ARA&A*, **40**, 487
- Fryer C. L., Belczynski K., Wiktorowicz G., Dominik M., Kalogera V., Holz D. E., 2012, *ApJ*, **749**, 91
- Gaia Collaboration et al., 2018, *A&A*, **616**, A1
- García Pérez A. E., et al., 2015, preprint, (arXiv:1510.07635)
- González Hernández J. I., Bonifacio P., 2009, *A&A*, **497**, 497
- González Hernández J. I., et al., 2008, *A&A*, **480**, 233
- González Hernández J. I., Bonifacio P., Caffau E., Ludwig H. G., Steffen M., Monaco L., Cayrel R., 2019, *A&A*, **628**, A111
- Greif T. H., Bromm V., Clark P. C., Glover S. C. O., Smith R. J., Klessen R. S., Yoshida N., Springel V., 2012, *MNRAS*, **424**, 399
- Guo Q., White S., Li C., Boylan-Kolchin M., 2010, *MNRAS*, **404**, 1111

- Gustafsson B., Edvardsson B., Eriksson K., Jørgensen U. G., Nordlund Å., Plez B., 2008, *A&A*, **486**, 951
- Hansen T. T., Andersen J., Nordström B., Beers T. C., Placco V. M., Yoon J., Buchhave L. A., 2016, preprint, ([arXiv:1601.03385](https://arxiv.org/abs/1601.03385))
- Hansen T. T., et al., 2017, *ApJ*, **838**, 44
- Hartwig T., et al., 2018, *MNRAS*, **478**, 1795
- Hasselquist S., et al., 2017, *ApJ*, **845**, 162
- Hayden M. R., Bovy J., Holtzman J. A. e. a., 2015, *ApJ*, **808**, 132
- Hayes C. R., et al., 2018, *ApJ*, **852**, 49
- Heger A., Woosley S. E., 2010, *ApJ*, **724**, 341
- Helmi A., White S. D. M., de Zeeuw P. T., Zhao H., 1999, *Nature*, **402**, 53
- Helmi A., Veljanoski J., Breddels M. A., Tian H., Sales L. V., 2017, *A&A*, **598**, A58
- Helmi A., Babusiaux C., Koppelman H. H., Massari D., Veljanoski J., Brown A. G. A., 2018, *Nature*, **563**, 85
- Howes L. M., et al., 2015, *Nature*, **527**, 484
- Howes L. M., et al., 2016, *MNRAS*, **460**, 884
- Ibata R. A., Gilmore G., Irwin M. J., 1994, *Nature*, **370**, 194
- Ishigaki M. N., Tominaga N., Kobayashi C., Nomoto K., 2014, *ApJ*, **792**, L32
- Iwamoto N., Umeda H., Tominaga N., Nomoto K., Maeda K., 2005, *Science*, **309**, 451
- Ji A. P., Frebel A., Chiti A., Simon J. D., 2016, *Nature*, **531**, 610
- Johnston K. V., Bullock J. S., Sharma S., Font A., Robertson B. E., Leitner S. N., 2008, *ApJ*, **689**, 936
- Joyce M., Chaboyer B., 2015, *ApJ*, **814**, 142
- Joyce M., Chaboyer B., 2018, *ApJ*, **856**, 10
- Keller S. C., et al., 2007, *Publ. Astron. Soc. Australia*, **24**, 1
- Keller S. C., et al., 2014, *Nature*, **506**, 463
- Kobayashi C., Nomoto K., Hachisu I., 2015, *ApJ*, **804**, L24
- Kobayashi C., Karakas A. I., Lugaro M., 2020, *ApJ*, **900**, 179
- Koch A., McWilliam A., Grebel E. K., Zucker D. B., Belokurov V., 2008, *ApJ*, **688**, L13
- Koppelman H., Helmi A., Veljanoski J., 2018, *ApJ*, **860**, L11
- Korobkin O., Rosswog S., Arcones A., Winteler C., 2012, *MNRAS*, **426**, 1940
- Kovalev M., Bergemann M., Ting Y.-S., Rix H.-W., 2019, *A&A*, **628**, A54
- Kraft R. P., Ivans I. I., 2003, *PASP*, **115**, 143
- Kratz K.-L., Farouqi K., Pfeiffer B., Truran J. W., Sneden C., Cowan J. J., 2007, *ApJ*, **662**, 39
- Lamb M., et al., 2017, *MNRAS*, **465**, 3536
- Lee Y. S., et al., 2013, *AJ*, **146**, 132
- Lejeune T., Cuisinier F., Buser R., 1998, *VizieR Online Data Catalog*, [pp J/A+AS/130/65](https://cds.u-strasbg.fr/cgi-bin/vizie?-source=J/A+AS/130/65)
- Limberg G., et al., 2020, arXiv e-prints, [p. arXiv:2011.08305](https://arxiv.org/abs/2011.08305)
- Lind K., Asplund M., Barklem P. S., Belyaev A. K., 2011, *A&A*, **528**, A103
- Lind K., Bergemann M., Asplund M., 2012, *MNRAS*, **427**, 50
- Lindgren L., et al., 2018, *A&A*, **616**, A2
- Lucatello S., Tsangarides S., Beers T. C., Carretta E., Gratton R. G., Ryan S. G., 2005, *ApJ*, **625**, 825
- Lucchesi R., et al., 2020, arXiv e-prints, [p. arXiv:2001.11033](https://arxiv.org/abs/2001.11033)
- Lucey M., et al., 2019, *MNRAS*, **488**, 2283
- Lucey M., et al., 2020, arXiv e-prints, [p. arXiv:2009.03886](https://arxiv.org/abs/2009.03886)
- Lugaro M., Karakas A. I., Stancliffe R. J., Rijs C., 2012, *ApJ*, **747**, 2
- Lupton R. H., et al., 2005, in *American Astronomical Society Meeting Abstracts*. p. 133.08
- Maeder A., Meynet G., 2015, *A&A*, **580**, A32
- Majewski S. R., Schiavon R. P., Frinchaboy P. M., et al. 2015 2015, arXiv preprint [arXiv:1509.05420](https://arxiv.org/abs/1509.05420)
- Martoli E., Teeple D., Manset N., Devost D., Withington K., Venne A., Tannock M., 2012, Open source pipeline for ESPaDOs reduction and analysis. p. 84512B, [doi:10.1117/12.926627](https://doi.org/10.1117/12.926627)
- Mashonkina L. I., Belyaev A. K., 2019, *Astronomy Letters*, **45**, 341
- Mashonkina L., Gehren T., Bikmaev I., 1999, *A&A*, **343**, 519
- Mashonkina L., Korn A. J., Przybilla N., 2007, *A&A*, **461**, 261
- Mashonkina L., Jablonka P., Pakhomov Y., Sitnova T., North P., 2017, *A&A*, **604**, A129
- Matsuno T., Aoki W., Beers T. C., Lee Y. S., Honda S., 2017, *AJ*, **154**, 52
- Matsuno T., Aoki W., Suda T., 2019, *ApJ*, **874**, L35
- McWilliam A., Wallerstein G., Mottini M., 2013, *ApJ*, **778**, 149
- Meynet G., Ekström S., Maeder A., 2006, *A&A*, **447**, 623
- Meza A., Navarro J. F., Abadi M. G., Steinmetz M., 2005, *MNRAS*, **359**, 93
- Monty S., Venn K. A., Lane J. M. M., Lokhorst D., Yong D., 2020, *MNRAS*, **497**, 1236
- Mucciarelli A., Bellazzini M., 2020, *Research Notes of the American Astronomical Society*, **4**, 52
- Myeong G. C., Evans N. W., Belokurov V., Sanders J. L., Koposov S. E., 2018, *ApJ*, **863**, L28
- Myeong G. C., Vasiliev E., Iorio G., Evans N. W., Belokurov V., 2019, *MNRAS*, **488**, 1235
- Nakamura F., Umemura M., 2001, *ApJ*, **548**, 19
- Nishimura N., Takiwaki T., Thielemann F.-K., 2015, *ApJ*, **810**, 109
- Nissen P. E., Schuster W. J., 2010, *A&A*, **511**, L10
- Nordlander T., et al., 2019, *MNRAS*, **488**, L109
- Norris J. E., Yong D., 2019, *ApJ*, **879**, 37
- Norris J. E., Ryan S. G., Beers T. C., 1997, *ApJ*, **488**, 350
- Norris J. E., et al., 2013, *ApJ*, **762**, 28
- Norris J. E., Yong D., Venn K. A., Gilmore G., Casagrande L., Dotter A., 2017, *ApJS*, **230**, 28
- Onken C. A., et al., 2020, arXiv e-prints, [p. arXiv:2008.10359](https://arxiv.org/abs/2008.10359)
- Paxton B., Bildsten L., Dotter A., Herwig F., Lesaffre P., Timmes F., 2011, *ApJS*, **192**, 3
- Pazder J., Fournier P., Pawluczyk R., van Kooten M., 2014, The FRD and transmission of the 270-m GRACES optical fiber link and a high numerical aperture fiber for astronomy. p. 915124, [doi:10.1117/12.2057327](https://doi.org/10.1117/12.2057327)
- Pignatari M., et al., 2016, *ApJS*, **225**, 24
- Pilachowski C. A., Sneden C., Kraft R. P., 1996, *AJ*, **111**, 1689
- Placco V. M., Frebel A., Beers T. C., Stancliffe R. J., 2014, *ApJ*, **797**, 21
- Prieto C. A., Beers T. C., Wilhelm R., Newberg H. J., Rockosi C. M., Yanny B., Lee Y. S., 2006, *The Astrophysical Journal*, **636**, 804
- Roederer I. U., Preston G. W., Thompson I. B., Shectman S. A., Sneden C., Burley G. S., Kelson D. D., 2014, *AJ*, **147**, 136
- Roederer I. U., et al., 2016, *AJ*, **151**, 82
- Salvadori S., Bonifacio P., Caffau E., Korotin S., Andreevsky S., Spite M., Skúladóttir Á., 2019, *MNRAS*, **487**, 4261
- Sbordone L., et al., 2010, *A&A*, **522**, A26
- Schlafly E. F., Finkbeiner D. P., 2011, *ApJ*, **737**, 103
- Schlaufman K. C., Thompson I. B., Casey A. R., 2018, *ApJ*, **867**, 98
- Schlegel D. J., Finkbeiner D. P., Davis M., 1998, *ApJ*, **500**, 525
- Schneider R., Omukai K., Bianchi S., Valiante R., 2012, *MNRAS*, **419**, 1566
- Sestito F., et al., 2019, *MNRAS*, **484**, 2166
- Sestito F., et al., 2020, *MNRAS*, **497**, L7
- Sestito F., et al., 2021, *MNRAS*, **500**, 3750
- Silk J., 1983, *MNRAS*, **205**, 705
- Sitnova T. M., Mashonkina L. I., Ryabchikova T. A., 2013, *Astronomy Letters*, **39**, 126
- Sitnova T., et al., 2015, *ApJ*, **808**, 148
- Sitnova T. M., Mashonkina L. I., Ezzeddine R., Frebel A., 2019, *MNRAS*, **485**, 3527
- Sneden C., Cowan J. J., Gallino R., 2008, *ARA&A*, **46**, 241
- Spite M., Spite F., 1982, *Nature*, **297**, 483
- Starkenburger E., Shetrone M. D., McConnachie A. W., Venn K. A., 2014, *MNRAS*, **441**, 1217
- Starkenburger E., Oman K. A., Navarro J. F., Crain R. A., Fattahi A., Frenk C. S., Sawala T., Schaye J., 2017a, *MNRAS*, **465**, 2212
- Starkenburger E., et al., 2017b, *MNRAS*, **471**, 2587
- Steigman G., 2007, *Annual Review of Nuclear and Particle Science*, **57**, 463
- Susa H., Hasegawa K., Tominaga N., 2014, *ApJ*, **792**, 32
- Tegmark M., Silk J., Rees M. J., Blanchard A., Abel T., Palla F., 1997, *ApJ*, **474**, 1
- Theler R., et al., 2020, *A&A*, **642**, A176
- Tolstoy E., Hill V., Tosi M., 2009, *ARA&A*, **47**, 371
- Tominaga N., Iwamoto N., Nomoto K., 2014, *ApJ*, **785**, 98
- Tsujimoto T., Nishimura N., 2015, *ApJ*, **811**, L10
- VandenBerg D. A., Bergbusch P. A., Dotter A., Ferguson J. W., Michaud G., Richer J., Proffitt C. R., 2012, *ApJ*, **755**, 15

- Venn K. A., Irwin M., Shetrone M. D., Tout C. A., Hill V., Tolstoy E., 2004, *AJ*, **128**, 1177
- Venn K. A., Starkenburg E., Malo L., Martin N., Laevens B. P. M., 2017, *MNRAS*, **466**, 3741
- Venn K. A., et al., 2020, *MNRAS*, **492**, 3241
- Wanajo S., Müller B., Janka H.-T., Heger A., 2018, *ApJ*, **852**, 40
- Wang L., Dutton A. A., Stinson G. S., Macciò A. V., Penzo C., Kang X., Keller B. W., Wadsley J., 2015, *MNRAS*, **454**, 83
- White S. D. M., Springel V., 2000, in Weiss A., Abel T. G., Hill V., eds, *The First Stars*. p. 327 ([arXiv:astro-ph/9911378](https://arxiv.org/abs/astro-ph/9911378)), doi:10.1007/10719504_62
- Wise J. H., Turk M. J., Norman M. L., Abel T., 2012, *ApJ*, **745**, 50
- Woosley S. E., Weaver T. A., 1995, *ApJS*, **101**, 181
- Woosley S. E., Heger A., Weaver T. A., 2002, *Reviews of Modern Physics*, **74**, 1015
- Yanny B., et al., 2009, *AJ*, **137**, 4377
- Yong D., et al., 2013a, *ApJ*, **762**, 26
- Yong D., et al., 2013b, *ApJ*, **762**, 27
- Yoon J., et al., 2016, preprint, ([arXiv:1607.06336](https://arxiv.org/abs/1607.06336))
- York D. G., et al., 2000, *AJ*, **120**, 1579
- Yoshida N., Omukai K., Hernquist L., Abel T., 2006, *ApJ*, **652**, 6
- Youakim K., et al., 2017, preprint, ([arXiv:1708.01264](https://arxiv.org/abs/1708.01264))
- Yuan Z., et al., 2020, *ApJ*, **891**, 39
- de Boer T. J. L., Tolstoy E., Lemasle B., Saha A., Olszewski E. W., Mateo M., Irwin M. J., Battaglia G., 2014, *A&A*, **572**, A10

APPENDIX A: SPECTRA AND LINE DATA

A1 The 1D Spectra

The reduced 1D spectra for a subset of the stars in this paper (in T_{eff} and $[\text{Fe}/\text{H}]$) are shown in Figure A1. Only the wavelength region used in this paper for the chemical analysis is shown; a zoomed in region from 470 to 680 nm. Each star and its metallicity are labelled, and the objects are sorted by effective temperature. The Balmer lines ($H\alpha$ and $H\beta$) are clear, as well as the Mg β lines. The atmospheric bands near 5850 and 6300 are clear in most stars, as well as some sky emission lines from an imperfect sky subtraction. These stars were not telluric cleaned due to inconsistent observations of telluric standards.

A2 The world of (mostly) upper limits.

In higher metallicity stars, several spectral lines of additional elements exist in the GRACES wavelength region. We examine those regions, to provide additional abundances, but mostly upper limits only. The upper limits in this section do not provide useful constraints for nucleosynthetic interpretations, thus they are collected here in an Appendix, for completeness. These elements include the odd-elements (K, Sc, Mn, Cu), also Zn, and the neutron capture elements (Y, Zr, La, Nd). See Table B15 for our line list and their adopted atomic data, including isotopic and/or hyperfine structure information.

Sc and K abundances were measured in 1 and 5 stars, respectively. It is unclear if the slight increase in K with decreasing metallicity is astrophysically significant as the uncertainties for each star are large, but certainly some stars appear to be rich in K. The upper limits on Zn, Y, Nd, and La are in good agreement with the distribution of $[\text{X}/\text{Fe}]$ in metal-poor stars in the Galaxy. One r-process rich star (P016+28; CEMP-s, discussed in the main text) also has enriched, and therefore measureable, La and Nd abundances.

Finally, oxygen is included here since we could analyse the strong $\lambda 7770$ triplet (see Fig. A3); however, these lines are known

to form over many layers in a stellar atmosphere, being very sensitive to small uncertainties in stellar parameters, and especially NLTE corrections. They are also in a region of significant telluric contamination. The O abundances for six stars where we could measure the O I triplet are shown in Fig. A4.

A3 Line List

A sample line list is provided in Table B15, including the element, wavelength, excitation potential (χ in eV), and oscillator strengths ($\log gf$). The majority of the analysis of our GRACES data was carried out using spectrum syntheses, thus the line abundance from each spectral feature is listed (rather than an equivalent width). These line abundances have been averaged together for the final abundance, per element, per star.

APPENDIX B: DATA TABLES

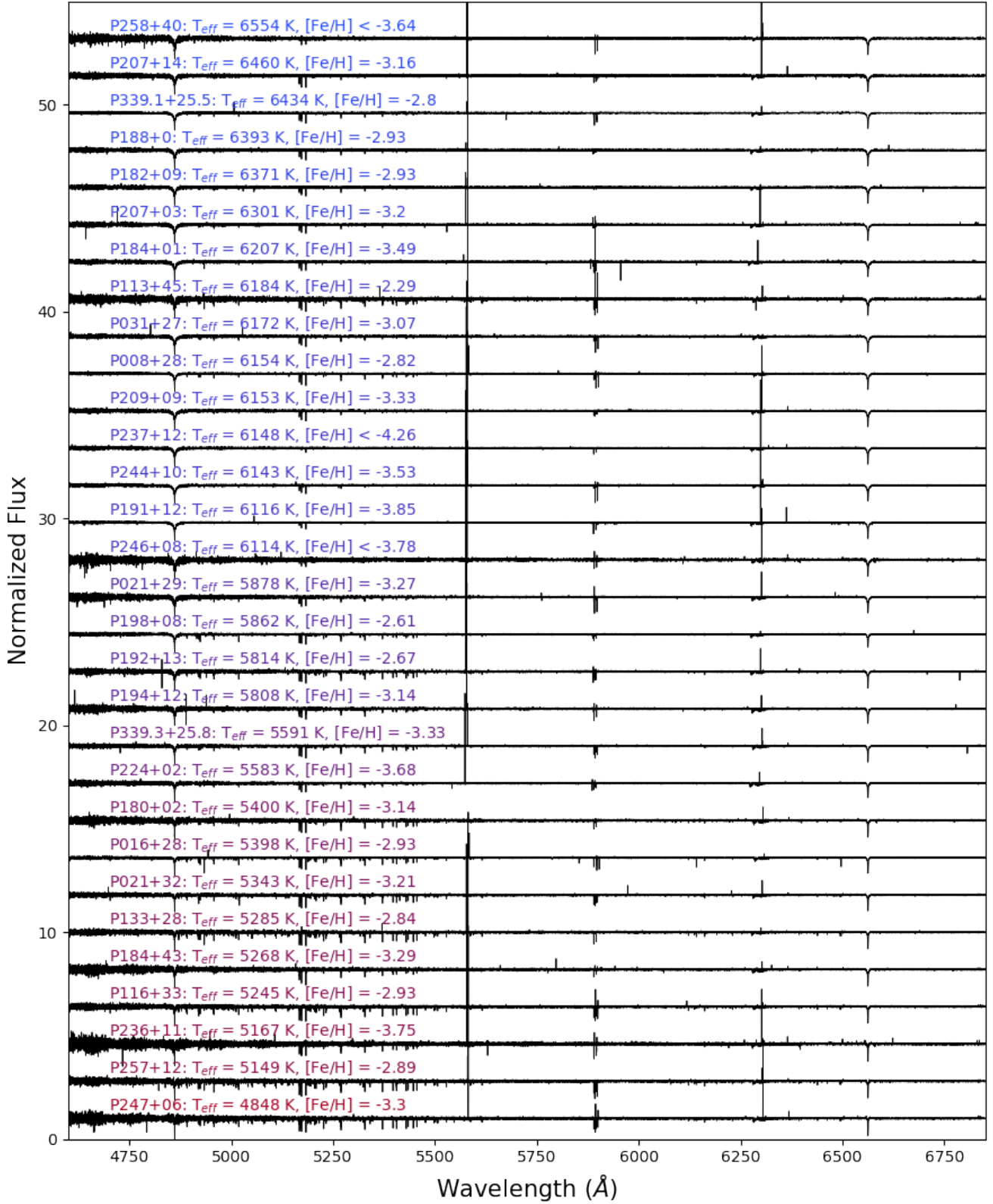


Figure A1. Portion of the 1D spectra for our GRACES data, sorted by temperature. This region was selected for our detailed analyses as it has the highest SNR, is mostly free of telluric and sky lines, and contains spectral lines for many elements of interest.

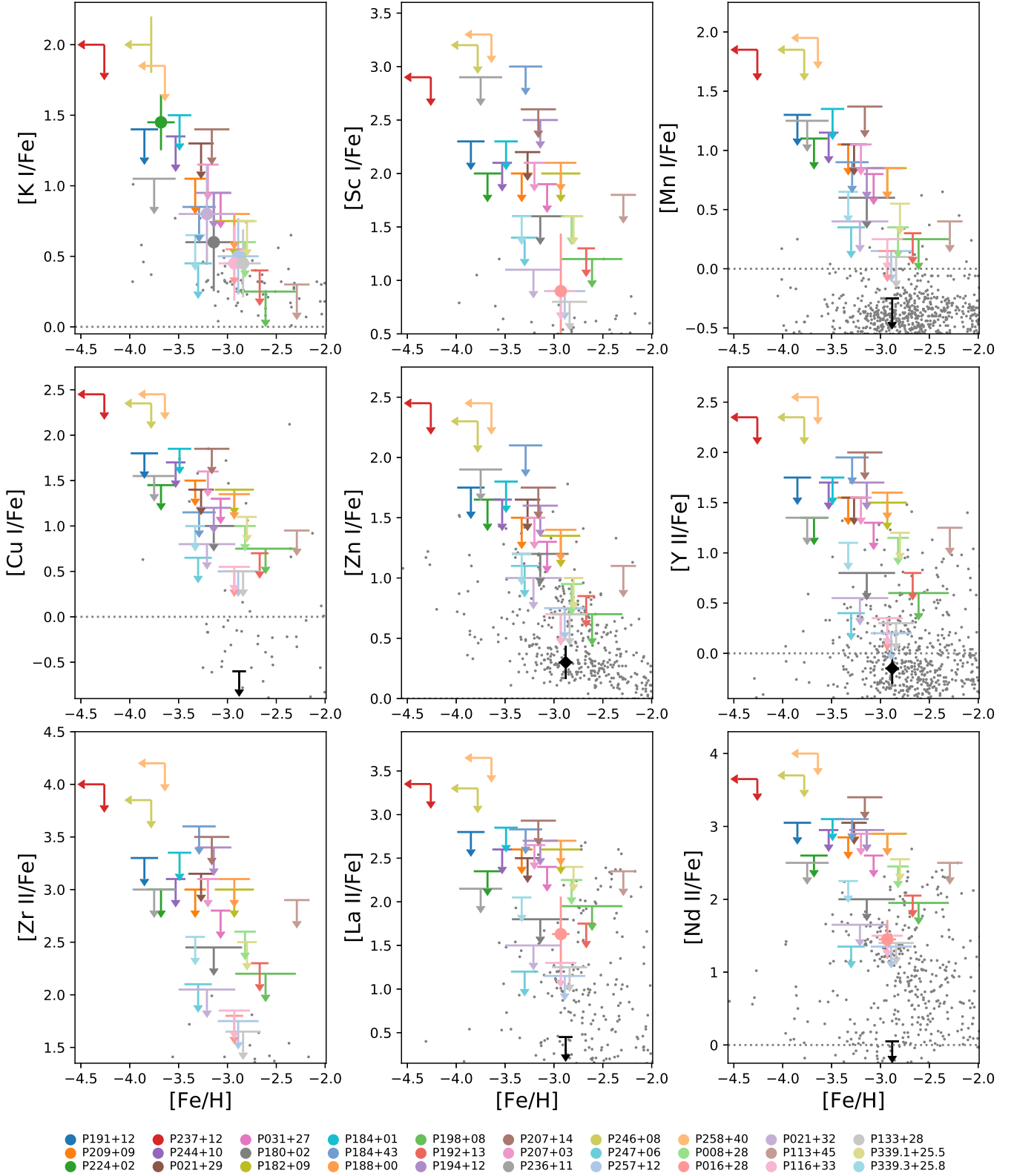


Figure A2. Elemental abundances for the chemical elements with mainly upper limit in our analysis. See Fig. 9 for more information on the labels and Galactic comparison stars.

Table B1. Stellar identifications, positions, and CaHK and SDSS dereddened magnitudes for our GRACES targets, selected from the *Pristine* survey (Starkenburg et al. 2017a; Aguado et al. 2019). E(B-V) values from Schlegel et al. (1998), and the observer V magnitudes from the SDSS conversions. Total exposure times (number of exposures), observation dates, and final SNR (at 6000 Å) are also provided.

ID	RA (deg)	Dec (deg)	V (mag)	E(B-V)	CaHK ₀ (mag)	g ₀ (mag)	r ₀ (mag)	i ₀ (mag)	t _{exp} (s, #)	SNR	Obs. Dates
<i>2018A:</i>											
P191.8535+12.0508	191.8535	12.0508	15.21	0.03	15.52	15.26	15.05	14.98	5580 (3)	121	6/16, 6/17/2018
P209.0986+09.8244	209.0986	9.8244	15.50	0.03	15.79	15.51	15.32	15.25	6300 (3)	75	6/15/2018
P224.8444+02.3043	224.8444	2.3043	15.21	0.05	15.64	15.27	14.91	14.76	4500 (3)	91	4/24/2018
P237.8589+12.5660	237.8589	12.5660	15.58	0.04	15.84	15.58	15.37	15.30	8100 (4)	95	6/15, 6/16/2018
P244.8986+10.9310	244.8986	10.9310	15.58	0.07	15.76	15.48	15.28	15.22	7200 (4)	86	4/25, 6/15/2018
<i>2018B:</i>											
P021.6938+29.0039	21.6938	29.0039	15.78	0.08	16.00	15.72	15.47	15.36	9600 (4)	61	1/16, 1/17/2019
P031.9938+27.7363	31.9938	27.7363	15.55	0.05	15.77	15.54	15.34	15.27	5400 (3)	74	1/17/2019
P180.3206+02.5788	180.3206	2.5788	15.71	0.02	16.30	15.89	15.46	15.28	9600 (4)	50	1/18, 1/20/2019
P182.5866+09.8940	182.5866	9.8940	15.23	0.02	15.60	15.30	15.07	15.00	5400 (3)	87	1/19/2019
P184.1783+01.0664	184.1783	1.0664	15.81	0.02	16.11	15.85	15.66	15.59	7200 (3)	75	1/16/2019
P184.2997+43.4721	184.2997	43.4721	15.92	0.01	16.70	16.16	15.68	15.49	7200 (3)	46	1/19/2019
P188.0262+00.2055	188.0262	0.2055	15.51	0.02	15.86	15.58	15.34	15.27	7200 (4)	76	1/19, 1/20/2019
P198.0851+08.9428	198.0851	8.9428	15.67	0.03	16.05	15.74	15.47	15.38	7200 (3)	114	1/20/2019
<i>2019A:</i>											
P192.3242+13.3956	192.3242	13.3956	15.61	0.03	16.03	15.69	15.38	15.28	9600 (4)	68	3/27/2019
P194.9935+12.0585	194.9935	12.0585	15.25	0.03	15.81	15.36	15.02	14.91	6000 (3)	53	3/27, 3/28/2019
P207.3454+14.1268	207.3454	14.1268	16.45	0.03	16.77	16.50	16.28	16.18	14400 (6)	54	6/22, 6/28/2019
P207.9290+03.2767	207.9290	3.2767	15.50	0.03	15.79	15.53	15.34	15.27	9600 (4)	81	3/26/2019
P236.9604+11.6155	236.9604	11.6155	15.63	0.06	16.26	15.73	15.24	15.01	8800 (4)	34	3/29/2019
P246.9682+08.5360	246.9682	8.5360	15.57	0.06	15.77	15.51	15.30	15.24	8800 (4)	44	3/30/2019
P247.2115+06.6348	247.2115	6.6348	15.39	0.06	16.33	15.55	14.92	14.65	6600 (3)	47	3/31/2019
P257.3131+12.8939	257.3131	12.8939	15.31	0.12	15.82	15.24	14.71	14.49	6600 (3)	53	3/29/2019
P258.1048+40.5405	258.1048	40.5405	16.06	0.04	16.34	16.07	15.88	15.82	31200 (13)	53	3/31, 6/22/2019
<i>2019B:</i>											
P008.5638+28.1855	8.5638	28.1855	15.31	0.05	15.65	15.34	15.06	14.97	8100 (3)	105	11/14/2019
P016.2907+28.3957	16.2907	28.3957	14.93	0.06	15.49	15.01	14.59	14.41	5400 (3)	112	11/08/2019
P021.9576+32.4131	21.9576	32.4131	15.75	0.05	16.36	15.89	15.42	15.21	8100 (3)	78	11/11, 11/12/2019
P113.8240+45.1863	113.8240	45.1863	15.43	0.07	15.71	15.39	15.13	15.06	7200 (3)	40	11/09/2019
P116.9657+33.5337	116.9657	33.5337	15.52	0.06	16.16	15.59	15.13	14.91	7200 (3)	55	11/11/2019
P133.0683+28.7219	133.0683	28.7219	15.39	0.03	16.08	15.56	15.11	14.90	7200 (3)	66	01/18/2020
P339.1417+25.5503	339.1417	25.5503	14.77	0.04	15.01	14.76	14.54	14.47	5400 (3)	112	11/08/2019
P339.3203+25.8764	339.3203	25.8764	15.37	0.06	15.78	15.40	15.04	14.90	7200 (3)	66	11/09, 11/11/2019

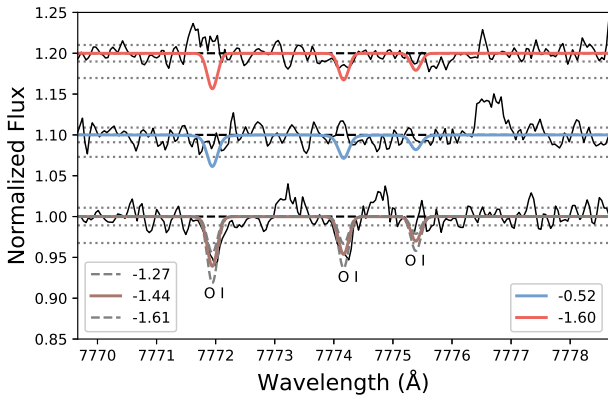


Figure A3. Synthesized O I lines for P207+14 (brown, bottom), P184+43 (blue, middle), and P192+13 (red, top). Labels the same as in Fig. 9.

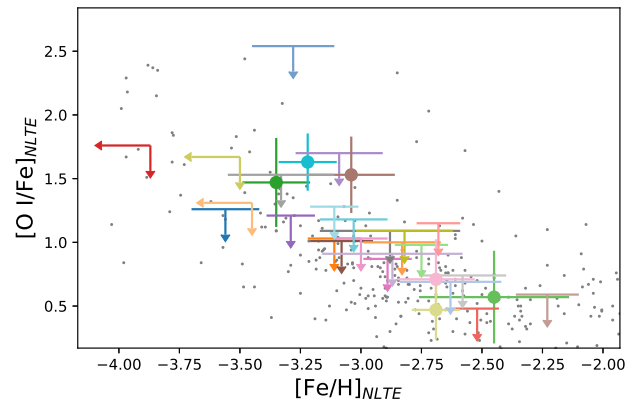


Figure A4. NLTE abundances for oxygen and iron, $[O/Fe]_{NLTE}$ vs. $[Fe/H]_{NLTE}$. Labels the same as in Fig. 9.

Table B2. Stellar parameters from the Pristine photometric survey (PRIS, [Starkenburg et al. 2017b](#)) and follow-up medium resolution spectroscopy (MRS) analyzed with FERRE [Aguado et al. \(2019\)](#) are shown. Carbonicity is also determined from the medium resolution spectra, with the exception of P207.3454+14.1268 which was observed with a medium-resolution ESO 3.6m-EFOSC spectrum ([Buzzoni et al. 1984](#)). The C-rich flag denotes whether the star has $[C/Fe] > 1.0$, and an asterisk denotes that the SNR was too low for a reliable determination. Radial velocities from medium resolution spectroscopy (from [Sestito et al. 2020](#)) are compared to our more precise GRACES values.

ID	PRIS T_{phot} (K)	PRIS $[Fe/H]_{\text{phot}}$ (dex)	MRS SNR	MRS T_{eff} (K)	MRS $\log g$ (dex)	MRS $[Fe/H]$ (dex)	MRS C-rich?	MRS RV (km s^{-1})	GRACES RV (km s^{-1})
P008.5638+28.1855	6173	-3.04	34	6169 ± 17	5.00 ± 0.07	-2.84 ± 0.05	N*	-266.4 ± 7.4	-272.3 ± 0.5
P016.2907+28.3957	5583	-3.02	21	5378 ± 24	1.13 ± 0.10	-3.27 ± 0.04	Y	-384.5 ± 10.8	-374.3 ± 0.5
P021.6938+29.0039	6184	-3.31	25	5789 ± 20	1.09 ± 0.09	-3.40 ± 0.04	Y*	-91.0 ± 8.4	-85.4 ± 0.5
P021.9576+32.4131	5408	-3.53	55	5379 ± 147	2.40 ± 0.84	-2.67 ± 0.19	N*	—	-152.6 ± 0.1
P031.9938+27.7363	6465	-3.27	25	6477 ± 35	4.93 ± 0.04	-2.83 ± 0.04	N*	-215.1 ± 11.1	-209.4 ± 0.6
P113.8240+45.1863	6296	-2.71	27	5900 ± 12	5.00 ± 0.00	-3.10 ± 0.03	Y*	-126.9 ± 7.6	-135.9 ± 0.6
P116.9657+33.5337	5423	-2.65	20	5025 ± 15	1.01 ± 0.01	-3.04 ± 0.02	N	-171.5 ± 11.6	-180.9 ± 0.4
P133.0683+28.7219	5445	-3.01	8	5288 ± 29	1.02 ± 0.01	-3.41 ± 0.05	Y*	6.8 ± 20.7	11.9 ± 0.6
P180.3206+02.5788	5563	-3.53	25	5406 ± 107	1.84 ± 1.14	-2.99 ± 0.11	N*	-212.3 ± 9.7	-204.9 ± 0.4
P182.5866+09.8940	6360	-2.87	34	6237 ± 131	5.00 ± 0.44	-3.48 ± 0.11	N*	139.5 ± 8.3	95.3 ± 0.2
P184.1783+01.0664	6483	-2.97	33	6323 ± 48	4.36 ± 0.14	-3.49 ± 0.06	Y*	407.2 ± 10.8	397.6 ± 1.4
P184.2997+43.4721	5419	-2.92	24	5509 ± 26	4.97 ± 0.02	-3.66 ± 0.04	N*	-104.4 ± 12.0	-110.3 ± 0.6
P188.0262+00.2055	6339	-3.00	16	6049 ± 52	4.76 ± 0.18	-3.23 ± 0.07	Y*	114.4 ± 8.7	93.3 ± 0.3
P191.8535+12.0508	6422	-3.14	33	6270 ± 53	4.75 ± 0.12	-3.88 ± 0.11	N*	18.8 ± 9.9	30.6 ± 0.4
P192.3242+13.3956	6047	-3.10	22	6142 ± 34	4.96 ± 0.03	-2.75 ± 0.04	N*	—	61.1 ± 0.7
P194.9935+12.0585	5936	-2.41	28	5935 ± 39	4.95 ± 0.05	-2.89 ± 0.06	N*	-34.8 ± 7.8	-42.7 ± 3.0
P198.0851+08.9428	6215	-3.00	7	5623 ± 81	1.26 ± 0.25	-3.37 ± 0.11	N*	—	105.1 ± 0.1
P207.3454+14.1268	6304	-3.17	55	6058 ± 280	4.14 ± 0.89	-4.01 ± 0.65	N*	—	-78.8 ± 0.1
P207.9290+03.2767	6516	-2.95	18	6490 ± 46	4.89 ± 0.10	-2.96 ± 0.07	N*	126.4 ± 7.1	109.3 ± 0.3
P209.0986+09.8244	6477	-2.92	32	6395 ± 38	4.85 ± 0.09	-3.14 ± 0.05	N*	-108.8 ± 8.9	-116.7 ± 0.1
P224.8444+02.3043	5791	-3.40	19	5455 ± 39	1.23 ± 0.18	-3.92 ± 0.08	Y*	196.3 ± 24.3	189.2 ± 0.8
P236.9604+11.6155	5320	-3.21	23	5298 ± 29	1.10 ± 0.08	-3.39 ± 0.03	N	-47.8 ± 9.8	-53.5 ± 0.9
P237.8589+12.5660	6443	-3.08	37	6323 ± 34	4.53 ± 0.09	-3.88 ± 0.08	N*	6.5 ± 8.0	-3.8 ± 0.9
P244.8986+10.9310	6492	-2.92	26	6481 ± 28	4.97 ± 0.03	-3.11 ± 0.05	N*	-182.1 ± 11.6	-176.7 ± 0.3
P246.9682+08.5360	6446	-3.13	34	6411 ± 32	4.70 ± 0.07	-3.45 ± 0.05	N*	-55.2 ± 9.8	-58.0 ± 0.5
P247.2115+06.6348	4969	-2.87	9	5026 ± 68	1.96 ± 0.36	-2.99 ± 0.08	N*	—	-200.8 ± 0.4
P257.3131+12.8939	5277	-2.99	19	5281 ± 53	2.50 ± 0.48	-2.80 ± 0.06	N	-129.4 ± 7.0	-129.4 ± 0.4
P258.1048+40.5405	6510	-2.92	79	6283 ± 297	3.95 ± 0.90	-3.76 ± 0.73	N*	—	-169.4 ± 1.5
P339.1417+25.5503	6413	-3.15	27	6048 ± 30	5.00 ± 0.00	-3.42 ± 0.06	Y*	-53.5 ± 7.8	-78.9 ± 0.1
P339.3203+25.8764	5816	-3.24	22	5589 ± 31	4.99 ± 0.01	-3.49 ± 0.07	N*	-141.5 ± 9.0	-157.7 ± 0.3

Table B3. Stellar parameters and iron abundances for our GRACES sample. Effective temperatures are from the [Mucciarelli & Bellazzini \(2020\)](#) calibration and surface gravities are calculated from the Stefan-Boltzmann law (see text). Short ID's are used to identify stars throughout the text and in the figures. Iron abundance errors represent the total combined systematic error due to the stellar parameters and the line-to-line scatter (see [Table B11](#)). The number of lines used to calculate the average [Fe/H] are given in parentheses. $\Delta\text{Fe}_{\text{NLTE}}$ is the averaged NLTE correction for Fe I lines with known NLTE calculations, in the sense that $\text{Fe}_{\text{NLTE}} = \text{Fe}_{\text{LTE}} + \Delta\text{Fe}_{\text{NLTE}}$. *Slope* is the slope of the line fit to A(Fe I) vs. excitation potential, which can serve as a spectroscopic check of the effective temperature when more than 10 lines are available.

ID	Short ID	T_{eff} (K)	$\log g$ (dex)	[Fe I/H]	[Fe II/H]	[Fe/H]	FeI–FeII	$\Delta\text{Fe}_{\text{NLTE}}$	<i>Slope</i>
P008.5638+28.1855	P008+28	6154 ± 241	4.61 ± 0.08	-2.80 ± 0.23 (22)	-2.88 ± 0.12 (3)	-2.82 ± 0.11 (25)	0.08	0.07 (13)	-0.06
P016.2907+28.3957	P016+28	5398 ± 116	2.40 ± 0.10	-2.95 ± 0.26 (50)	-2.85 ± 0.28 (6)	-2.93 ± 0.20 (56)	-0.10	0.25 (26)	-0.02
P021.6938+29.0039	P021+29	5878 ± 137	3.54 ± 0.10	-3.29 ± 0.95 (12)	-3.14 ± 0.45 (4)	-3.27 ± 0.41 (16)	-0.15	0.19 (7)	0.10
P021.9576+32.4131	P021+32	5343 ± 116	2.02 ± 0.11	-3.05 ± 0.13 (45)	-3.62 ± 0.13 (3)	-3.21 ± 0.30 (48)	0.57	0.34 (23)	-0.03
P031.9938+27.7363	P031+27	6172 ± 212	3.79 ± 0.10	-3.07 ± 0.78 (13)	-3.07 ± 0.27 (4)	-3.07 ± 0.26 (17)	0.00	0.18 (8)	0.01
P113.8240+45.1863	P113+45	6184 ± 210	4.51 ± 0.09	-2.28 ± 0.27 (27)	-2.41 ± 0.18 (4)	-2.29 ± 0.16 (31)	0.13	0.06 (13)	0.03
P116.9657+33.5337	P116+33	5245 ± 108	2.15 ± 0.11	-2.86 ± 0.11 (62)	-3.14 ± 0.13 (5)	-2.93 ± 0.16 (67)	0.28	0.24 (32)	-0.03
P133.0683+28.7219	P133+28	5285 ± 123	2.09 ± 0.10	-2.75 ± 0.09 (68)	-3.09 ± 0.13 (6)	-2.84 ± 0.19 (74)	0.34	0.26 (36)	-0.06
P180.3206+02.5788	P180+02	5400 ± 113	2.53 ± 0.11	-2.90 ± 0.26 (7)	-3.20 ± 0.31 (3)	-3.14 ± 0.25 (10)	0.30	0.26 (5)	-0.03
P182.5866+09.8940	P182+09	6371 ± 260	4.51 ± 0.10	-2.90 ± 0.19 (7)	-3.20 ± 0.21 (3)	-2.93 ± 0.21 (10)	0.30	0.11 (5)	-0.03
P184.1783+01.0664	P184+01	6207 ± 171	3.64 ± 0.13	-3.50 ± 0.43 (3)	-3.47 ± 0.16 (3)	-3.49 ± 0.15 (6)	-0.03	0.27 (1)	1.85
P184.2997+43.4721	P184+43	5268 ± 146	4.94 ± 0.09	-3.31 ± 0.28 (14)	<-3.27	-3.29 ± 0.28 (17)	>-0.04	0.01 (6)	-0.08
P188.0262+00.2055	P188+00	6393 ± 230	4.55 ± 0.09	-2.86 ± 0.10 (10)	-3.12 ± 0.10 (3)	-2.93 ± 0.15 (13)	0.26	0.10 (4)	-0.05
P191.8535+12.0508	P191+12	6116 ± 164	3.61 ± 0.09	-3.78 ± 1.01 (7)	-3.96 ± 0.39 (3)	-3.85 ± 0.37 (10)	0.18	0.29 (2)	0.11
P192.3242+13.3956	P192+13	5814 ± 117	3.46 ± 0.10	-2.66 ± 0.56 (42)	-2.73 ± 0.21 (4)	-2.67 ± 0.20 (46)	0.07	0.15 (25)	-0.01
P194.9935+12.0585	P194+12	5808 ± 214	4.55 ± 0.09	-3.15 ± 0.40 (8)	-3.04 ± 0.18 (2)	-3.14 ± 0.17 (10)	-0.11	0.05 (5)	-0.02
P198.0851+08.9428	P198+08	5862 ± 132	3.39 ± 0.10	-2.66 ± 0.29 (24)	-2.06 ± 0.19 (6)	-2.61 ± 0.34 (30)	-0.60	0.16 (14)	0.02
P207.3454+14.1268	P207+14	6460 ± 253	4.63 ± 0.09	-3.16 ± 0.11 (2)	-3.19 ± 0.25 (2)	-3.16 ± 0.10 (4)	0.03	0.12 (1)	-0.89
P207.9290+03.2767	P207+03	6301 ± 251	3.88 ± 0.11	-3.19 ± 0.68 (8)	-3.24 ± 0.22 (3)	-3.20 ± 0.21 (11)	0.05	0.20 (4)	-0.02
P209.0986+09.8244	P209+09	6153 ± 180	3.70 ± 0.11	-3.32 ± 0.78 (8)	-3.37 ± 0.28 (3)	-3.33 ± 0.26 (11)	0.05	0.22 (4)	0.04
P224.8444+02.3043	P224+02	5583 ± 116	2.86 ± 0.13	-3.72 ± 0.13 (7)	-3.51 ± 0.16 (3)	-3.68 ± 0.15 (10)	-0.21	0.33 (4)	0.03
P236.9604+11.6155	P236+11	5167 ± 115	1.80 ± 0.10	-3.52 ± 0.11 (11)	-3.93 ± 0.21 (3)	-3.75 ± 0.23 (14)	0.41	0.42 (5)	0.12
P237.8589+12.5660	P237+12	6148 ± 175	3.61 ± 0.10	<-4.28	<-4.23	<-4.26	<-0.05	0.39 (1)	0.07
P244.8986+10.9310	P244+10	6143 ± 150	3.72 ± 0.09	-3.52 ± 0.82 (6)	-3.57 ± 0.31 (3)	-3.53 ± 0.29 (9)	0.05	0.24 (3)	0.00
P246.9682+08.5360	P246+08	6114 ± 142	3.58 ± 0.10	<-3.65	<-3.90	<-3.78	<0.25	0.28 (9)	0.33
P247.2115+06.6348	P247+06	4848 ± 97	1.19 ± 0.10	-3.26 ± 0.12 (45)	-3.50 ± 0.18 (4)	-3.30 ± 0.16 (49)	0.24	0.27 (22)	-0.06
P257.3131+12.8939	P257+12	5149 ± 105	1.78 ± 0.10	-2.85 ± 0.07 (63)	-3.22 ± 0.13 (3)	-2.89 ± 0.19 (66)	0.37	0.26 (33)	-0.05
P258.1048+40.5405	P258+40	6554 ± 245	4.37 ± 0.09	<-3.42	<-3.87	<-3.64	<0.45	0.19 (8)	-0.26
P339.1417+25.5503	P339.1+25.5	6434 ± 237	4.41 ± 0.09	-2.78 ± 0.25 (19)	-2.87 ± 0.11 (4)	-2.80 ± 0.11 (23)	0.09	0.11 (13)	0.00
P339.3203+25.8764	P339.3+25.8	5591 ± 118	3.11 ± 0.10	-3.28 ± 0.14 (23)	-3.45 ± 0.17 (3)	-3.33 ± 0.14 (26)	0.17	0.22 (12)	-0.01
HD 122563		4749 ± 89	1.12 ± 0.11	-2.89 ± 0.10 (54)	-2.87 ± 0.09 (9)	-2.88 ± 0.07 (63)	-0.02	0.11 (48)	-0.08

Table B4. LTE abundances for the α -elements. Errors represent the total combined systematic error due to the stellar parameters and line-to-line scatter (Table B8 and B9). The number of lines used is given in parentheses.

ID	[O I/Fe]	[Mg I/Fe]	[Ca I/Fe]	[Ca II/Fe]	[Ti I/Fe]	[Ti II/Fe]
P008.5638+28.1855	<1.05	0.47 ± 0.13 (4)	0.08 ± 0.15 (3)	0.78 ± 0.15 (3)	<0.45	<0.55
P016.2907+28.3957	<1.40	0.55 ± 0.11 (4)	0.29 ± 0.13 (10)	1.17 ± 0.13 (3)	0.48 ± 0.15 (4)	0.61 ± 0.11 (6)
P021.6938+29.0039	<1.20	0.11 ± 0.18 (2)	0.33 ± 0.15 (4)	0.92 ± 0.20 (3)	<1.10	<0.50
P021.9576+32.4131	<1.25	0.78 ± 0.29 (3)	0.46 ± 0.30 (7)	0.42 ± 0.32 (3)	<0.20	0.15 ± 0.34 (1)
P031.9938+27.7363	<1.05	0.50 ± 0.16 (3)	0.38 ± 0.14 (4)	0.95 ± 0.12 (3)	<0.80	<0.65
P113.8240+45.1863	<0.70	0.09 ± 0.34 (2)	0.00 ± 0.17 (5)	0.30 ± 0.21 (1)	<0.55	<0.50
P116.9657+33.5337	0.95 ± 0.30 (1)	0.57 ± 0.18 (3)	0.35 ± 0.17 (8)	0.25 ± 0.25 (3)	0.35 ± 0.19 (3)	0.24 ± 0.18 (2)
P133.0683+28.7219	<1.00	0.15 ± 0.44 (2)	0.27 ± 0.20 (10)	0.43 ± 0.25 (3)	0.30 ± 0.27 (2)	0.30 ± 0.22 (1)
P180.3206+02.5788	<1.35	0.47 ± 0.19 (3)	0.30 ± 0.20 (6)	0.60 ± 0.21 (3)	0.52 ± 0.27 (2)	1.40 ± 0.27 (1)
P182.5866+09.8940	<1.20	-0.02 ± 0.22 (2)	0.80 ± 0.28 (1)	0.73 ± 0.22 (3)	<0.80	<0.95
P184.1783+01.0664	1.90 ± 0.20 (2)	0.77 ± 0.26 (2)	<0.45	1.20 ± 0.12 (2)	<1.30	<1.25
P184.2997+43.4721	<2.55	0.51 ± 0.28 (2)	<-0.25	0.11 ± 0.17 (3)	<0.75	<1.35
P188.0262+0.2055	<1.10	0.43 ± 0.17 (3)	0.15 ± 0.29 (2)	0.88 ± 0.21 (3)	<0.90	<0.85
P191.8535+12.0508	<1.55	0.25 ± 0.16 (2)	<0.15	1.27 ± 0.16 (3)	<1.35	<1.10
P192.3242+13.3956	<0.70	0.16 ± 0.13 (3)	0.11 ± 0.10 (5)	0.62 ± 0.26 (2)	<0.25	0.35 ± 0.20 (1)
P194.9935+12.0585	<1.75	0.32 ± 0.36 (2)	0.17 ± 0.19 (2)	0.53 ± 0.35 (2)	<0.50	<1.05
P198.0851+08.9428	0.81 ± 0.36 (2)	0.65 ± 0.34 (2)	-0.19 ± 0.32 (4)	1.13 ± 0.33 (3)	<0.15	0.47 ± 0.33 (2)
P207.3454+14.1268	1.65 ± 0.26 (1)	1.09 ± 0.15 (3)	<-0.45	1.06 ± 0.17 (2)	<1.35	<1.25
P207.9290+03.2767	<1.23	0.23 ± 0.19 (2)	0.55 ± 0.21 (3)	1.04 ± 0.14 (3)	<0.95	<0.90
P209.0986+09.8244	<1.25	0.76 ± 0.12 (4)	0.35 ± 0.22 (2)	0.96 ± 0.13 (3)	<1.05	<0.90
P224.8444+02.3043	1.80 ± 0.34 (1)	0.32 ± 0.17 (3)	0.25 ± 0.19 (1)	1.39 ± 0.22 (3)	<0.95	<0.70
P236.9604+11.6155	<1.95	0.52 ± 0.40 (2)	0.57 ± 0.30 (2)	0.64 ± 0.25 (3)	<1.00	<0.75
P237.8589+12.5660	<2.15	<0.15	<0.95	<1.25	<1.40	<1.40
P244.8986+10.9310	<1.45	0.47 ± 0.18 (4)	0.57 ± 0.16 (3)	1.16 ± 0.12 (3)	<1.10	<1.00
P246.9682+08.5360	<1.95	<0.28	<0.85	<1.22	<1.40	<1.35
P247.2115+06.6348	<1.45	0.53 ± 0.16 (3)	0.27 ± 0.17 (5)	0.24 ± 0.36 (2)	0.38 ± 0.18 (4)	0.43 ± 0.23 (4)
P257.3131+12.8939	<0.95	0.59 ± 0.21 (4)	0.38 ± 0.22 (8)	0.37 ± 0.23 (3)	0.39 ± 0.25 (3)	0.22 ± 0.22 (5)
P258.1048+40.5405	<1.50	<0.40	<0.65	<1.46	<1.40	<1.40
P339.1417+25.5503	0.70 ± 0.22 (2)	0.28 ± 0.19 (2)	0.27 ± 0.15 (5)	0.92 ± 0.15 (3)	0.60 ± 0.25 (1)	<0.35
P339.3203+25.8764	<1.50	0.63 ± 0.20 (2)	0.23 ± 0.12 (4)	0.64 ± 0.14 (3)	<0.20	<0.45
HD 122563	—	0.62 ± 0.09 (4)	0.31 ± 0.08 (14)	—	0.15 ± 0.16 (1)	0.33 ± 0.07 (10)

Table B5. LTE abundances for light elements and Fe-peak elements. Errors represent the total combined systematic error due to the stellar parameters and line-to-line scatter (Table B10 and B11). The number of lines used is given in parentheses. P016.2907+28.3957 is the only star in the sample to have a detectable Sc abundance. The systematic errors for P016.2907+28.3957 are given in Table B13.

ID	[Na I/Fe]	[K I/Fe]	[Sc II/Fe]	[Cr I/Fe]	[Mn I/Fe]	[Ni I/Fe]	[Cu I/Fe]	[Zn I/Fe]
P008.5638+28.1855	-0.15 ± 0.17 (1)	<0.60	<1.60	-0.20 ± 0.20 (1)	<0.35	<0.05	<1.00	<0.95
P016.2907+28.3957	0.37 ± 0.18 (2)	<0.55	0.90 ± 0.53 (1)	-0.15 ± 0.16 (4)	<0.15	-0.05 ± 0.16 (1)	<0.50	<0.70
P021.6938+29.0039	<-0.40	<1.30	<2.20	-0.05 ± 0.25 (1)	<1.05	0.20 ± 0.27 (1)	<1.40	<1.65
P021.9576+32.4131	0.07 ± 0.31 (2)	0.80 ± 0.33 (1)	<1.10	-0.02 ± 0.31 (3)	<0.40	0.10 ± 0.32 (1)	<0.80	<1.00
P031.9938+27.7363	-0.10 ± 0.17 (1)	<0.95	<1.90	-0.15 ± 0.27 (1)	<0.80	<0.15	<1.30	<1.30
P113.8240+45.1863	0.36 ± 0.27 (2)	<0.30	<1.80	-0.33 ± 0.24 (2)	<0.40	<-0.30	<0.95	<1.10
P116.9657+33.5337	0.05 ± 0.24 (2)	0.45 ± 0.25 (1)	<0.90	-0.23 ± 0.21 (3)	<0.25	-0.05 ± 0.21 (1)	<0.55	<0.70
P133.0683+28.7219	0.02 ± 0.24 (2)	0.45 ± 0.24 (1)	<0.80	-0.29 ± 0.23 (3)	<0.10	-0.02 ± 0.35 (2)	<0.50	<0.70
P180.3206+02.5788	-0.15 ± 0.22 (2)	0.60 ± 0.25 (1)	<1.60	-0.20 ± 0.24 (1)	<0.60	<-0.10	<1.00	<1.20
P182.5866+09.8940	-0.55 ± 0.26 (2)	<0.75	<2.00	<-0.20	<0.85	<0.15	<1.40	<1.35
P184.1783+01.0664	1.92 ± 0.27 (2)	<1.50	<2.30	<0.10	<1.35	<0.70	<1.85	<1.80
P184.2997+43.4721	-0.21 ± 0.16 (2)	<0.85	<3.00	-0.45 ± 0.27 (1)	<0.90	<0.15	<1.15	<2.10
P188.0262+0.2055	-0.48 ± 0.22 (2)	<0.80	<2.10	<-0.15	<0.85	<0.20	<1.35	<1.40
P191.8535+12.0508	<0.00	<1.40	<2.30	<0.20	<1.30	<0.60	<1.80	<1.75
P192.3242+13.3956	-0.64 ± 0.19 (2)	<0.40	<1.30	-0.22 ± 0.21 (2)	<0.30	0.00 ± 0.16 (1)	<0.70	<0.85
P194.9935+12.0585	<-0.55	<0.95	<2.50	<-0.30	<0.85	<0.10	<1.20	<1.60
P198.0851+08.9428	-0.24 ± 0.35 (2)	<0.25	<1.20	-0.31 ± 0.36 (2)	<0.25	<-0.25	<0.75	<0.70
P207.3454+14.1268	0.51 ± 0.19 (2)	<1.40	<2.60	<0.15	<1.37	<0.70	<1.85	<1.75
P207.9290+03.2767	-0.28 ± 0.22 (2)	<1.15	<2.10	0.10 ± 0.25 (2)	<1.05	<0.45	<1.60	<1.50
P209.0986+09.8244	0.00 ± 0.18 (2)	<1.05	<2.00	<-0.15	<1.05	0.30 ± 0.29 (1)	<1.50	<1.50
P224.8444+02.3043	0.29 ± 0.14 (2)	1.45 ± 0.18 (1)	<2.00	-0.10 ± 0.21 (1)	<1.10	<0.25	<1.45	<1.65
P236.9604+11.6155	<0.90	<1.05	<2.90	<-0.10	<1.25	<0.30	<1.55	<1.90
P237.8589+12.5660	<0.00	<2.00	<2.90	<0.80	<1.85	<1.00	<2.45	<2.45
P244.8986+10.9310	0.00 ± 0.15 (2)	<1.35	<2.10	<0.10	<1.15	<0.60	<1.70	<1.65
P246.9682+08.5360	<0.25	<2.00	<3.20	<0.75	<1.85	<1.00	<2.35	<2.30
P247.2115+06.6348	-0.01 ± 0.21 (2)	<0.45	<1.40	-0.18 ± 0.20 (4)	<0.35	-0.05 ± 0.20 (1)	<0.65	<1.10
P257.3131+12.8939	0.04 ± 0.41 (2)	0.50 ± 0.25 (1)	<0.90	-0.02 ± 0.26 (3)	<0.15	0.07 ± 0.31 (2)	<0.50	<0.75
P258.1048+40.5405	<-0.05	<1.85	<3.30	<0.50	<1.95	<1.00	<2.45	<2.45
P339.1417+25.5503	<-0.40	<0.75	<1.60	-0.13 ± 0.24 (2)	<0.55	<-0.05	<1.10	<1.00
P339.3203+25.8764	0.08 ± 0.14 (2)	<0.65	<1.60	-0.15 ± 0.19 (1)	<0.65	<-0.15	<1.00	<1.20
HD 122563	0.43 ± 0.11 (2)	—	—	-0.08 ± 0.12 (8)	<-0.25	0.00 ± 0.13 (1)	<-0.60	0.30 ± 0.13 (1)

Table B6. LTE abundances for neutron-capture elements. Errors represent the total combined systematic error due to the stellar parameters and line-to-line scatter (Table B12). P016.2907+28.3957 is the only star in the sample to have detectable La and Nd abundances. The systematic errors for P016.2907+28.3957 are given in Table B13.

ID	[Y II/Fe]	[Zr II/Fe]	[Ba II/Fe]	[La II/Fe]	[Nd II/Fe]	[Eu II/Fe]
P008.5638+28.1855	<1.15	<2.60	<0.05	<2.25	<2.45	<2.55
P016.2907+28.3957	<0.30	<1.80	2.13 ± 0.19 (2)	1.63 ± 0.42 (1)	1.45 ± 0.26 (1)	<1.75
P021.6938+29.0039	<1.55	<3.15	<0.05	<2.50	<3.05	<2.65
P021.9576+32.4131	<0.55	<2.05	<-0.65	<1.50	<1.65	<1.90
P031.9938+27.7363	<1.30	<2.80	<0.20	<2.40	<2.60	<2.65
P113.8240+45.1863	<1.25	<2.90	0.75 ± 0.27 (2)	<2.35	<2.50	<2.30
P116.9657+33.5337	<0.35	<1.85	<-0.95	<1.30	<1.50	<1.60
P133.0683+28.7219	<0.30	<1.65	-0.15 ± 0.29 (2)	<1.25	<1.40	<1.55
P180.3206+02.5788	<0.80	<2.45	<-0.55	<1.80	<2.00	<2.10
P182.5866+09.8940	<1.50	<3.00	<0.35	<2.60	<2.90	<2.80
P184.1783+01.0664	<1.75	<3.35	1.47 ± 0.16 (2)	<2.85	<3.10	<3.30
P184.2997+43.4721	<1.95	<3.60	<0.35	<2.83	<3.10	<3.05
P188.0262+0.2055	<1.60	<3.10	<0.45	<2.70	<2.90	<2.90
P191.8535+12.0508	<1.75	<3.30	<0.65	<2.80	<3.05	<3.15
P192.3242+13.3956	<0.80	<2.30	<-0.55	<1.75	<2.05	<2.00
P194.9935+12.0585	<1.70	<3.40	<0.25	<2.70	<2.95	<2.80
P198.0851+08.9428	<0.60	<2.20	<-0.40	<1.95	<1.95	<2.05
P207.3454+14.1268	<2.00	<3.50	<0.80	<2.93	<3.40	<3.27
P207.9290+03.2767	<1.55	<3.10	<0.30	<2.65	<2.90	<2.80
P209.0986+09.8244	<1.55	<3.00	<0.40	<2.60	<2.85	<2.90
P224.8444+02.3043	<1.35	<3.00	<0.25	<2.35	<2.60	<2.65
P236.9604+11.6155	<1.35	<3.00	<-0.10	<2.15	<2.50	<2.40
P237.8589+12.5660	<2.35	<4.00	<1.25	<3.35	<3.65	<3.75
P244.8986+10.9310	<1.70	<3.10	0.66 ± 0.25 (2)	<2.60	<2.95	<3.10
P246.9682+08.5360	<2.35	<3.85	<1.00	<3.30	<3.70	<3.50
P247.2115+06.6348	<0.40	<2.10	-0.80 ± 0.21 (2)	<1.20	<1.35	<1.45
P257.3131+12.8939	<0.20	<1.75	-0.40 ± 0.26 (2)	<1.15	<1.35	<1.40
P258.1048+40.5405	<2.55	<4.20	<1.15	<3.65	<4.00	<3.65
P339.1417+25.5503	<1.20	<2.50	<0.10	<2.40	<2.55	<2.55
P339.3203+25.8764	<1.10	<2.55	<-0.25	<2.05	<2.25	<2.40
HD 122563	-0.15 ± 0.15 (4)	—	-0.95 ± 0.15 (2)	<0.45	<0.05	<0.60

Table B7. LTE lithium abundances from the Li doublet at 6707 Å. The σ represents the line measurement error due to the continuum placement. ΔT and Δg are the systematic errors in the stellar parameters T_{eff} and $\log g$, while ΔFe is due to the uncertainty in $[\text{Fe}/\text{H}]$ (see Table B3). Δ is the total combined error of these added in quadrature.

ID	A(Li)	σ	ΔT	Δg	ΔFe	Δ
P008.5638+28.1855	1.98	0.14	-0.13	-0.08	-0.09	0.23
P016.2907+28.3957	<0.82					
P021.6938+29.0039	1.58	0.14	-0.52	-0.42	-0.46	0.82
P021.9576+32.4131	0.89	0.22	0.08	0.13	0.11	0.29
P031.9938+27.7363	1.73	0.18	-0.42	-0.37	-0.38	0.70
P113.8240+45.1863	1.96	0.18	-0.17	-0.12	-0.12	0.30
P116.9657+33.5337	0.87	0.20	-0.05	-0.05	-0.04	0.21
P133.0683+28.7219	<0.89					
P180.3206+02.5788	0.96	0.22	-0.09	-0.04	-0.09	0.26
P182.5866+09.8940	1.82	0.16	-0.08	-0.08	-0.10	0.22
P184.1783+01.0664	<1.56					
P184.2997+43.4721	<1.06					
P188.0262+00.2055	1.94	0.18	0.07	0.12	0.11	0.25
P191.8535+12.0508	1.60	0.16	-0.43	-0.43	-0.41	0.75
P192.3242+13.3956	1.93	0.14	-0.25	-0.20	-0.20	0.40
P194.9935+12.0585	1.41	0.18	-0.32	-0.32	-0.32	0.58
P198.0851+08.9428	<1.34					
P207.3454+14.1268	<1.79					
P207.9290+03.2767	1.95	0.14	-0.14	-0.14	-0.11	0.27
P209.0986+09.8244	1.62	0.22	-0.39	-0.29	-0.30	0.61
P224.8444+02.3043	<1.02					
P236.9604+11.6155	<1.00					
P237.8589+12.5660	1.49	0.20	-0.48	-0.38	-0.38	0.75
P244.8986+10.9310	1.72	0.16	-0.38	-0.33	-0.30	0.61
P246.9682+08.5360	1.92	0.27	-0.11	0.04	0.04	0.30
P247.2115+06.6348	<0.50					
P257.3131+12.8939	<0.66					
P258.1048+40.5405	1.96	0.18	-0.13	-0.08	-0.08	0.25
P339.1417+25.5503	1.90	0.14	-0.11	-0.11	-0.10	0.23
P339.3203+25.8764	1.52	0.14	0.03	0.03	0.05	0.16
HD122563	<-0.18					

Table B8. Systematic errors for the α -elements (pt. 1). The σ represents the line-to-line scatter for a given element, added in quadrature with errors imposed by the continuum placement for each line used. When the number of lines $N_X > 5$ for species X, then σ is reduced by $1/\sqrt{N_X}$. ΔT and Δg are the systematic errors in the stellar parameters T_{eff} and $\log g$, while ΔFe is due to the uncertainty in $[\text{Fe}/\text{H}]$ (see Table B3). Δ is the total combined error of these added in quadrature.

ID	[O I/H]					[Mg I/H]					[Ca I/H]				
	σ	ΔT	Δg	ΔFe	Δ	σ	ΔT	Δg	ΔFe	Δ	σ	ΔT	Δg	ΔFe	Δ
P008.5638+28.1855						0.05	-0.06	-0.03	-0.04	0.09	0.08	-0.10	-0.10	-0.11	0.20
P016.2907+28.3957						0.07	0.28	0.31	0.29	0.51	0.07	0.11	0.12	0.12	0.21
P021.6938+29.0039						0.13	-0.27	-0.22	-0.21	0.42	0.10	-0.33	-0.28	-0.27	0.52
P021.9576+32.4131						0.07	0.12	0.12	0.08	0.19	0.06	0.02	0.03	0.07	0.10
P031.9938+27.7363						0.10	-0.11	-0.10	-0.09	0.20	0.09	-0.25	-0.26	-0.25	0.45
P113.8240+45.1863						0.26	-0.02	-0.01	-0.03	0.26	0.11	-0.12	-0.11	-0.12	0.23
P116.9657+33.5337	0.24	0.13	0.08	0.14	0.32	0.09	0.02	0.03	0.04	0.11	0.07	-0.01	-0.01	0.00	0.07
P133.0683+28.7219						0.39	0.17	0.14	0.20	0.49	0.07	0.00	0.00	0.01	0.07
P180.3206+02.5788						0.10	0.07	0.07	0.07	0.15	0.08	-0.04	-0.03	-0.03	0.10
P182.5866+09.8940						0.10	0.08	0.10	0.08	0.18	0.20	-0.08	-0.08	-0.05	0.24
P184.1783+01.0664	0.15	0.41	0.23	0.29	0.58	0.12	0.29	0.39	0.40	0.63					
P184.2997+43.4721						0.22	-0.18	-0.18	-0.18	0.38					
P188.0262+00.2055						0.06	0.10	0.10	0.10	0.18	0.21	-0.08	-0.05	-0.06	0.24
P191.8535+12.0508						0.05	-0.36	-0.30	-0.33	0.58					
P192.3242+13.3956						0.09	-0.14	-0.09	-0.09	0.20	0.06	-0.24	-0.18	-0.18	0.35
P194.9935+12.0585						0.22	0.21	0.21	0.21	0.42	0.16	-0.14	-0.15	-0.15	0.30
P198.0851+08.9428	0.17	0.29	0.16	0.24	0.44	0.13	0.05	0.13	0.12	0.22	0.10	-0.17	-0.09	-0.10	0.24
P207.3454+14.1268	0.18	0.17	0.12	0.14	0.31	0.08	0.09	0.10	0.11	0.20					
P207.9290+03.2767						0.11	-0.12	-0.09	-0.11	0.21	0.14	-0.25	-0.21	-0.23	0.42
P209.0986+09.8244						0.09	-0.10	-0.05	-0.02	0.14	0.19	-0.34	-0.24	-0.25	0.52
P224.8444+02.3043	0.31	-0.22	-0.22	-0.32	0.54	0.09	0.07	0.14	0.09	0.20	0.11	-0.06	-0.01	-0.06	0.14
P236.9604+11.6155						0.33	0.16	0.14	0.14	0.42	0.19	-0.03	-0.03	-0.02	0.20
P237.8589+12.5660						0.13	-0.40	-0.33	-0.36	0.65					
P244.8986+10.9310						0.16	-0.23	-0.16	-0.18	0.37	0.14	-0.30	-0.25	-0.21	0.47
P246.9682+08.5360						0.12	-0.22	-0.09	-0.09	0.28					
P247.2115+06.6348						0.08	0.03	0.03	0.06	0.11	0.09	-0.05	-0.02	-0.02	0.11
P257.3131+12.8939						0.08	0.01	0.03	0.03	0.09	0.07	0.02	0.05	0.07	0.11
P258.1048+40.5405						0.15	-0.03	-0.03	-0.03	0.16					
P339.1417+25.5503	0.16	0.22	0.17	0.18	0.37	0.15	0.14	0.14	0.15	0.29	0.08	-0.10	-0.06	-0.09	0.17
P339.3203+25.8764						0.16	0.21	0.18	0.20	0.38	0.06	-0.04	-0.04	-0.04	0.09
HD 122563						0.06	-0.05	0.00	0.01	0.08	0.05	-0.04	0.00	0.01	0.07

Table B9. Systematic errors for the α -elements (pt. 2). See the caption for Table B8.

ID	[Ca II/H]					[Ti I/H]					[Ti II/H]				
	σ	ΔT	Δg	ΔFe	Δ	σ	ΔT	Δg	ΔFe	Δ	σ	ΔT	Δg	ΔFe	Δ
P008.5638+28.1855	0.10	-0.03	-0.00	0.01	0.11										
P016.2907+28.3957	0.11	0.18	0.18	0.21	0.34	0.07	0.04	0.05	0.07	0.12	0.07	0.02	-0.01	0.02	0.07
P021.6938+29.0039	0.15	-0.25	-0.29	-0.21	0.46										
P021.9576+32.4131	0.10	-0.08	-0.09	-0.06	0.17						0.18	-0.07	-0.12	-0.09	0.25
P031.9938+27.7363	0.10	-0.18	-0.20	-0.19	0.34										
P113.8240+45.1863	0.16	-0.17	-0.12	-0.12	0.29										
P116.9657+33.5337	0.19	-0.17	-0.20	-0.18	0.37	0.08	-0.10	-0.08	-0.07	0.17	0.10	-0.14	-0.15	-0.14	0.27
P133.0683+28.7219	0.15	-0.17	-0.18	-0.15	0.33	0.15	-0.10	-0.05	-0.07	0.20	0.11	-0.10	-0.10	-0.07	0.19
P180.3206+02.5788	0.13	-0.09	-0.11	-0.06	0.21	0.18	-0.12	-0.09	-0.09	0.25	0.21	-0.14	-0.14	-0.14	0.32
P182.5866+09.8940	0.11	0.07	0.07	0.05	0.15										
P184.1783+01.0664	0.08	-0.00	-0.05	0.01	0.10										
P184.2997+43.4721	0.09	-0.04	-0.02	-0.04	0.11										
P188.0262+00.2055	0.12	0.06	0.06	0.05	0.16										
P191.8535+12.0508	0.10	0.04	0.01	0.03	0.11										
P192.3242+13.3956	0.24	-0.21	-0.21	-0.23	0.44						0.18	-0.25	-0.25	-0.20	0.45
P194.9935+12.0585	0.19	0.71	0.71	0.65	1.21										
P198.0851+08.9428	0.08	-0.09	-0.13	-0.03	0.18						0.12	-0.14	-0.17	-0.14	0.29
P207.3454+14.1268	0.10	0.22	0.22	0.24	0.41										
P207.9290+03.2767	0.09	-0.16	-0.17	-0.14	0.29										
P209.0986+09.8244	0.10	-0.20	-0.21	-0.16	0.34										
P224.8444+02.3043	0.17	-0.12	-0.09	-0.09	0.25										
P236.9604+11.6155	0.13	-0.14	-0.15	-0.12	0.27										
P237.8589+12.5660	0.16	0.28	0.25	0.32	0.52										
P244.8986+10.9310	0.08	-0.18	-0.19	-0.16	0.31										
P246.9682+08.5360	0.10	-0.10	-0.07	-0.06	0.17										
P247.2115+06.6348	0.33	-0.25	-0.29	-0.27	0.57	0.09	-0.08	-0.09	-0.05	0.16	0.18	-0.14	-0.15	-0.12	0.30
P257.3131+12.8939	0.11	-0.14	-0.16	-0.14	0.28	0.08	-0.08	-0.01	-0.04	0.12	0.08	-0.13	-0.13	-0.11	0.23
P258.1048+40.5405	0.15	-0.03	-0.03	-0.03	0.16										
P339.1417+25.5503	0.11	-0.04	-0.04	-0.03	0.13	0.18	-0.16	-0.16	-0.15	0.33					
P339.3203+25.8764	0.09	-0.09	-0.10	-0.08	0.18										
HD 122563						0.11	-0.10	0.00	-0.04	0.16	0.06	-0.01	-0.02	0.01	0.06

Table B10. Systematic errors for [Na I/H] and [K I/H]. See the caption for Table B8.

ID	[Na I/H]					[K I/H]				
	σ	ΔT	Δg	ΔFe	Δ	σ	ΔT	Δg	ΔFe	Δ
P008.5638+28.1855	0.06	-0.05	0.00	-0.01	0.08					
P016.2907+28.3957	0.16	0.58	0.58	0.56	1.00					
P021.6938+29.0039										
P021.9576+32.4131	0.09	0.11	0.16	0.14	0.26	0.15	0.03	0.08	0.06	0.19
P031.9938+27.7363	0.06	-0.32	-0.27	-0.28	0.51					
P113.8240+45.1863	0.21	0.05	0.09	0.09	0.25					
P116.9657+33.5337	0.15	0.10	0.15	0.11	0.26	0.17	-0.05	-0.05	-0.04	0.19
P133.0683+28.7219	0.11	0.10	0.10	0.13	0.23	0.15	0.00	0.00	-0.02	0.16
P180.3206+02.5788	0.13	0.03	0.06	0.06	0.16	0.17	-0.04	0.01	0.01	0.18
P182.5866+09.8940	0.13	-0.10	-0.08	-0.10	0.21					
P184.1783+01.0664	0.15	0.44	0.54	0.55	0.89					
P184.2997+43.4721	0.10	-0.10	-0.10	-0.09	0.19					
P188.0262+00.2055	0.10	-0.03	-0.03	-0.04	0.12					
P191.8535+12.0508										
P192.3242+13.3956	0.17	-0.27	-0.19	-0.19	0.42					
P194.9935+12.0585										
P198.0851+08.9428	0.14	-0.11	-0.06	-0.07	0.20					
P207.3454+14.1268	0.12	0.10	0.15	0.12	0.25					
P207.9290+03.2767	0.14	-0.28	-0.25	-0.25	0.47					
P209.0986+09.8244	0.08	-0.36	-0.26	-0.27	0.52					
P224.8444+02.3043	0.06	0.00	0.09	0.04	0.12					
P236.9604+11.6155										
P237.8589+12.5660										
P244.8986+10.9310	0.10	-0.37	-0.28	-0.30	0.56					
P246.9682+08.5360						0.17	-0.18	-0.18	-0.23	0.39
P247.2115+06.6348	0.16	0.09	0.09	0.12	0.24					
P257.3131+12.8939	0.36	0.14	0.18	0.16	0.45	0.13	-0.03	-0.03	-0.01	0.14
P258.1048+40.5405	0.16	-0.13	-0.08	-0.08	0.23					
P339.1417+25.5503										
P339.3203+25.8764	0.10	0.00	0.00	0.02	0.10					
HD 122563	0.08	-0.05	-0.04	0.01	0.10					

Table B11. Systematic errors for Fe and Fe-peak elements. See the caption for Table B8. Since only upper limits were determined for [Mn I/H], [Cu I/H], and [Zn I/H], for all stars in the sample, the systematic errors are not shown here.

ID	[Cr I/H]					[Fe I/H]					[Fe II/H]					[Ni I/H]				
	σ	ΔT	Δg	ΔFe	Δ	σ	ΔT	Δg	ΔFe	Δ	σ	ΔT	Δg	ΔFe	Δ	σ	ΔT	Δg	ΔFe	Δ
P008.5638+28.1855	0.11	-0.15	-0.15	-0.11	0.26	0.05	-0.15	-0.12	-0.11	0.23	0.12	0.01	0.01	0.02	0.12					
P016.2907+28.3957	0.11	0.06	0.09	0.08	0.17	0.04	0.13	0.16	0.16	0.26	0.09	0.16	0.13	0.16	0.28	0.11	0.11	0.11	0.09	0.21
P021.6938+29.0039	0.18	-0.62	-0.52	-0.51	0.97	0.06	-0.62	-0.51	-0.50	0.95	0.17	-0.23	-0.28	-0.20	0.45	0.23	-0.57	-0.47	-0.46	0.90
P021.9576+32.4131	0.07	0.05	0.07	0.05	0.12	0.05	0.05	0.07	0.07	0.13	0.07	-0.06	-0.07	-0.04	0.13	0.11	0.03	0.08	0.06	0.15
P031.9938+27.7363	0.18	-0.47	-0.42	-0.43	0.78	0.06	-0.48	-0.43	-0.42	0.78	0.09	-0.15	-0.15	-0.13	0.27					
P113.8240+45.1863	0.15	-0.22	-0.20	-0.20	0.38	0.06	-0.16	-0.14	-0.15	0.27	0.17	0.04	0.04	0.04	0.18					
P116.9657+33.5337	0.09	-0.11	-0.09	-0.08	0.18	0.04	-0.07	-0.05	-0.05	0.11	0.08	-0.06	-0.07	-0.05	0.13	0.11	-0.10	-0.05	-0.09	0.18
P133.0683+28.7219	0.08	-0.07	-0.04	-0.04	0.12	0.04	-0.06	-0.03	-0.05	0.09	0.07	-0.04	-0.08	-0.05	0.13	0.27	-0.09	-0.05	-0.06	0.30
P180.3206+02.5788	0.16	-0.09	-0.04	-0.04	0.19	0.06	0.13	0.16	0.15	0.26	0.17	0.16	0.13	0.16	0.31					
P182.5866+09.8940						0.06	-0.12	-0.10	-0.09	0.19	0.17	-0.08	-0.08	-0.06	0.21					
P184.1783+01.0664						0.08	-0.36	-0.16	-0.17	0.43	0.16	-0.01	0.03	0.00	0.16					
P184.2997+43.4721	0.20	-0.21	-0.16	-0.18	0.38	0.07	-0.18	-0.13	-0.15	0.28										
P188.0262+00.2055						0.05	-0.07	-0.04	-0.04	0.10	0.10	0.00	0.00	-0.01	0.10					
P191.8535+12.0508						0.11	-0.61	-0.56	-0.57	1.01	0.13	-0.22	-0.22	-0.20	0.39					
P192.3242+13.3956	0.17	-0.41	-0.33	-0.33	0.64	0.05	-0.38	-0.29	-0.29	0.56	0.11	-0.11	-0.12	-0.08	0.21	0.11	-0.40	-0.35	-0.35	0.65
P194.9935+12.0585						0.07	-0.24	-0.22	-0.22	0.40	0.16	0.05	0.05	0.05	0.18					
P198.0851+08.9428	0.14	-0.25	-0.15	-0.19	0.37	0.05	-0.21	-0.13	-0.14	0.29	0.17	0.01	-0.06	-0.03	0.19					
P207.3454+14.1268						0.10	0.01	0.04	0.03	0.11	0.25	0.02	0.02	0.01	0.25					
P207.9290+03.2767	0.14	-0.39	-0.37	-0.36	0.66	0.05	-0.41	-0.39	-0.38	0.68	0.11	-0.10	-0.13	-0.10	0.22					
P209.0986+09.8244						0.05	-0.53	-0.40	-0.40	0.78	0.09	-0.16	-0.16	-0.14	0.28	0.25	-0.49	-0.39	-0.35	0.76
P224.8444+02.3043	0.16	-0.11	-0.01	-0.06	0.20	0.05	-0.10	0.02	-0.06	0.13	0.11	-0.04	-0.09	-0.06	0.16					
P236.9604+11.6155						0.09	-0.05	-0.02	-0.02	0.11	0.08	-0.11	-0.12	-0.11	0.21					
P237.8589+12.5660																				
P244.8986+10.9310						0.05	-0.54	-0.45	-0.42	0.82	0.11	-0.17	-0.17	-0.15	0.31					
P246.9682+08.5360																				
P247.2115+06.6348	0.12	-0.07	-0.05	-0.05	0.16	0.05	-0.07	-0.06	-0.06	0.12	0.10	-0.07	-0.09	-0.08	0.18	0.11	-0.10	-0.05	-0.07	0.17
P257.3131+12.8939	0.15	-0.00	0.03	0.06	0.16	0.04	-0.05	0.00	-0.00	0.07	0.12	-0.00	-0.00	0.02	0.13	0.22	-0.05	0.00	-0.01	0.23
P258.1048+40.5405																				
P339.1417+25.5503	0.10	-0.16	-0.16	-0.15	0.29	0.05	-0.16	-0.12	-0.14	0.25	0.08	-0.04	-0.05	-0.04	0.11					
P339.3203+25.8764	0.16	-0.12	-0.12	-0.10	0.25	0.06	-0.09	-0.07	-0.05	0.14	0.09	-0.07	-0.10	-0.08	0.17					
HD 122563	0.08	-0.08	0.02	0.01	0.11	0.04	-0.09	-0.00	-0.00	0.10	0.07	-0.00	-0.05	-0.01	0.09	0.06	-0.10	0.00	0.01	0.12

Table B12. Systematic errors for [Ba II/H]. See the caption for Table B8.

ID	σ	ΔT	[Ba II/H]		
			Δg	ΔFe	Δ
P008.5638+28.1855					
P016.2907+28.3957	0.12	0.14	0.11	0.14	0.25
P021.6938+29.0039					
P021.9576+32.4131					
P031.9938+27.7363					
P113.8240+45.1863	0.12	-0.14	-0.14	-0.12	0.27
P116.9657+33.5337					
P133.0683+28.7219	0.11	-0.20	-0.20	-0.17	0.35
P180.3206+02.5788					
P182.5866+09.8940					
P184.1783+01.0664	0.12	-0.16	-0.06	-0.02	0.21
P184.2997+43.4721					
P188.0262+00.2055					
P191.8535+12.0508					
P192.3242+13.3956					
P194.9935+12.0585					
P198.0851+08.9428					
P207.3454+14.1268					
P207.9290+03.2767					
P209.0986+09.8244					
P224.8444+02.3043					
P236.9604+11.6155					
P237.8589+12.5660					
P244.8986+10.9310	0.21	-0.43	-0.38	-0.33	0.69
P246.9682+08.5360					
P247.2115+06.6348	0.13	-0.22	-0.22	-0.22	0.40
P257.3131+12.8939	0.12	-0.05	-0.02	-0.03	0.14
P258.1048+40.5405					
P339.1417+25.5503					
P339.3203+25.8764					
HD 122563	0.12	-0.05	-0.05	-0.01	0.14

Table B13. Systematic errors for [Sc II/H], [La II/H] and [Nd II/H] for P016.2907+28.3957.

ID	[Sc II/H]					[La II/H]					[Nd II/H]				
	σ	ΔT	Δg	ΔFe	Δ	σ	ΔT	Δg	ΔFe	Δ	σ	ΔT	Δg	ΔFe	Δ
P016.2907+28.3957	0.30	0.21	0.16	0.19	0.44	0.23	0.21	0.21	0.19	0.42	0.23	-0.06	-0.06	-0.03	0.25

Table B14. NLTE Corrections. NLTE deviations were calculated on a line-by-line basis for each star given its line list and stellar parameters; the averaged NLTE correction is given below. Corrections in oxygen are from [Sitnova et al. \(2013\)](#), Na from [Lind et al. \(2011\)](#), Mg from [Bergemann et al. \(2017\)](#), Ca from [Mashonkina et al. \(2007\)](#), Ti from [Bergemann \(2011\)](#), and Cr from [Bergemann & Cescutti \(2010\)](#).

ID	$\Delta[O\ I/H]$	$\Delta[Na\ I/H]$	$\Delta[Mg\ I/H]$	$\Delta[Ca\ I/H]$	$\Delta[Ti\ I/H]$	$\Delta[Ti\ II/H]$	$\Delta[Cr\ I/H]$
P008.5638+28.1855		-0.17 (1)	0.05 (4)	0.13 (3)	0.35 (2)	0.04 (2)	0.45 (1)
P016.2907+28.3957		-0.40 (2)	0.16 (4)	0.26 (6)	0.62 (3)	0.04 (6)	0.62 (4)
P021.6938+29.0039		-0.06 (2)	0.14 (2)	0.21 (3)		0.04 (2)	0.61 (1)
P021.9576+32.4131		-0.18 (2)	0.20 (3)	0.31 (6)	0.59 (2)	0.06 (1)	0.69 (3)
P031.9938+27.7363		-0.13 (1)	0.12 (3)	0.25 (3)		0.05 (2)	0.57 (1)
P113.8240+45.1863	-0.05 (2)	-0.42 (2)	0.03 (2)	0.08 (4)	0.34 (2)	0.04 (2)	0.36 (2)
P116.9657+33.5337		-0.30 (2)	0.15 (3)	0.26 (5)	0.62 (3)	0.05 (2)	0.61 (3)
P133.0683+28.7219		-0.31 (2)	0.15 (2)	0.27 (6)	0.62 (2)	0.04 (1)	0.60 (3)
P180.3206+02.5788		-0.13 (2)	0.16 (3)	0.26 (4)	0.60 (1)	0.01 (1)	0.66 (1)
P182.5866+09.8940		-0.07 (2)	0.07 (2)			0.04 (2)	0.47 (2)
P184.1783+01.0664		-0.27 (2)	0.17 (2)	0.35 (1)		0.04 (1)	0.63 (2)
P184.2997+43.4721		-0.09 (2)	0.00 (2)	0.12 (5)	0.21 (2)	0.03 (2)	0.40 (1)
P188.0262+0.2055		-0.08 (2)	0.07 (3)	0.16 (2)		0.04 (2)	0.47 (2)
P191.8535+12.0508		-0.05 (2)	0.20 (2)				
P192.3242+13.3956	-0.07 (2)	-0.10 (2)	0.09 (3)	0.18 (4)	0.49 (2)	0.05 (1)	0.53 (2)
P194.9935+12.0585		-0.05 (2)	0.04 (2)	0.13 (2)	0.34 (2)	0.03 (2)	0.49 (3)
P198.0851+08.9428	-0.08 (2)	-0.21 (2)	0.09 (2)	0.17 (3)	0.49 (2)	0.05 (2)	0.53 (2)
P207.3454+14.1268		-0.20 (2)	0.09 (3)	0.22 (4)		0.04 (1)	0.48 (2)
P207.9290+03.2767		-0.07 (2)	0.14 (2)	0.27 (2)		0.05 (2)	0.58 (2)
P209.0986+09.8244		-0.09 (2)	0.14 (4)	0.29 (2)		0.04 (2)	0.61 (2)
P224.8444+02.3043		-0.10 (2)	0.20 (3)	0.26 (1)		-0.00 (2)	0.72 (1)
P236.9604+11.6155		-0.31 (2)	0.26 (2)	0.30 (2)		0.05 (2)	0.76 (2)
P237.8589+12.5660		-0.04 (1)	0.23 (2)				
P244.8986+10.9310		-0.06 (2)	0.15 (4)	0.31 (1)		0.03 (1)	0.62 (2)
P246.9682+08.5360		-0.06 (2)	0.19 (2)				0.65 (1)
P247.2115+06.6348		-0.17 (2)	0.12 (3)	0.30 (4)	0.59 (3)	0.10 (4)	0.59 (4)
P257.3131+12.8939		-0.32 (2)	0.15 (4)	0.24 (6)	0.61 (3)	0.07 (5)	0.59 (3)
P258.1048+40.5405		-0.07 (1)	0.14 (2)				
P339.1417+25.5503	-0.12 (2)	-0.10 (2)	0.07 (2)	0.18 (3)		0.05 (2)	0.47 (2)
P339.3203+25.8764		-0.13 (2)	0.16 (2)	0.20 (2)		0.04 (2)	0.66 (1)
HD 122563		-0.33 (2)	0.08 (3)	0.22 (7)	0.48 (4)	0.08 (7)	0.39 (5)

Table B15. Sample line list of atomic lines used in this paper. The best fit abundance per line in each star is listed as $A(X) = \log[N(X)/N(H)] + 12$. Shortened target names are listed by their RA and DEC. The full table is available online.

Elem	λ (Å)	χ (eV)	$\log(gf)$	P016 +28	P237 +12	P247 +06	HD122563
Fe I	5269.537	0.858	-1.33	4.70	<3.22	3.95	4.51
Fe I	5328.039	0.914	-1.47	4.70	<3.37	4.00	4.61
Fe II	5169.028	2.891	-0.87	4.75	<3.27	4.20	
Li I	6707.924	0.0	-0.299	<0.82	1.49	<0.50	<-0.18
O I	7774.166	9.139	0.17	7.38	<6.80	<7.06	
Na I	5889.951	0.0	0.12	3.71	<1.98	2.94	3.81
Mg I	5172.684	2.71	-0.4	5.22	3.39	4.70	5.32
Mg I	5183.604	2.715	-0.18	5.37	3.59	4.65	5.52
K I	7698.974	0.0	-0.17	<2.65	<2.77	<2.18	
Ca I	6122.217	1.884	-0.41	3.86	<3.48	3.34	3.91
Ca I	6162.173	1.897	0.1	3.51	<3.03	3.14	3.61
Sc I	4670.4	1.356	-1.324	1.12	<1.79	<1.25	
Ti I	4981.731	0.848	0.57	2.42	<2.09	1.90	2.22
Ti I	4991.066	0.835	0.45	2.47	<2.09	1.95	2.32
Ti II	5188.68	1.581	-1.21	2.72	<2.09	2.00	2.42
Ti II	5226.543	1.565	-1.3	2.67	<2.09	1.80	2.27
Cr I	5206.023	0.941	0.02	2.51	<2.28	2.04	2.36
Cr I	5208.409	0.941	0.17	2.56	<2.18	1.94	2.51
Mn I	4823.514	2.317	-0.466	<2.65	<3.02	<2.48	2.35
Ni I	5476.904	1.825	-0.78	3.24	<2.96	2.87	3.34
Zn I	4810.528	4.075	-0.14	<2.33	<2.75	<2.36	1.98
Y II	4900.11	1.032	-0.09	<-0.12	<0.30	<-0.69	-0.92
Ba II	6141.73	0.704	-0.077	1.35	<-0.83	-1.92	-1.70
Ba II	6496.91	0.604	-0.38	1.40	<-0.68	-1.92	-1.60
La II	4920.798	0.59	-0.27	-0.20	<0.19	<-1.00	<-1.33
Nd II	4811.342	0.064	-1.14	0.69	<1.56	<0.22	<-1.06
Nd II	4825.48	0.182	-0.42	-0.06	<0.81	<-0.53	<-1.41
Eu II	6645.072	1.379	-0.517	<-0.66	<0.01	<-1.33	<-1.76

Table B16. Gaia DR2 proper motions, parallaxes, orbital parameters, and action vectors for stars in this paper, based on orbits calculated using the $1/\varpi$ distances. Actions and energies have been normalized to the Sun for brevity ($J_{\phi\odot} = 2009.92$ kpc km s⁻¹, $J_{z\odot} = 0.35$ kpc km s⁻¹, $E_{\odot} = -64943.61$ km² s⁻²; Sestito et al. 2019)

ID	μ_{α} ($\mu\text{as yr}^{-1}$)	μ_{δ} ($\mu\text{as yr}^{-1}$)	ϖ (μas)	r_{peri} (kpc)	r_{apo} (kpc)	Eccentricity	$ Z _{\text{max}}$ (kpc)	$J_{\phi}/J_{\phi\odot}$	$J_z/J_{z\odot}$	E/E_{\odot}
P008.5638+28.1855	44.54 ± 0.07	12.19 ± 0.07	0.8800 ± 0.0436	6.0 ± 0.1	11.7 ± 0.7	0.32 ± 0.02	10.9 ± 0.6	-0.27 ± 0.02	3113.98 ± 11.60	0.803 ± -0.028
P016.2907+28.3957	3.66 ± 0.06	-1.95 ± 0.05	0.0840 ± 0.0365	5.7 ± 2.1	29.3 ± 7.0	0.68 ± 0.03	20.3 ± 1.4	-0.70 ± 0.40	2061.04 ± 572.95	0.391 ± -0.117
P021.6938+29.0039	13.42 ± 0.09	4.54 ± 0.07	0.3643 ± 0.0452	4.8 ± 0.1	11.6 ± 0.9	0.42 ± 0.03	8.4 ± 1.6	0.45 ± 0.05	1532.21 ± 403.68	0.849 ± -0.038
P021.9576+32.4131	6.83 ± 0.09	-4.16 ± 0.08	0.1301 ± 0.0519	3.3 ± 3.3	13.2 ± 3.1	0.67 ± 0.21	4.0 ± 1.2	-0.39 ± 0.48	254.75 ± 112.52	0.860 ± -0.159
P031.9938+27.7363	12.91 ± 0.09	-26.81 ± 0.10	0.4654 ± 0.0553	2.5 ± 1.1	11.8 ± 0.6	0.66 ± 0.11	3.5 ± 1.4	-0.42 ± 0.12	307.35 ± 178.99	0.922 ± -0.062
P113.8240+45.1863	-33.61 ± 0.07	-23.27 ± 0.05	0.7620 ± 0.0506	9.0 ± 0.1	20.9 ± 2.1	0.40 ± 0.04	17.9 ± 2.3	0.64 ± 0.02	3755.69 ± 437.76	0.496 ± -0.046
P116.9657+33.5337	0.94 ± 0.07	-11.58 ± 0.04	0.1269 ± 0.0452	5.7 ± 3.9	45.4 ± 80.6	0.76 ± 0.09	24.0 ± 30.6	-0.77 ± 0.79	1440.86 ± 297.30	0.325 ± -0.292
P133.0683+28.7219	-0.73 ± 0.08	-11.92 ± 0.05	0.1443 ± 0.0514	5.7 ± 4.9	16.4 ± 14.8	0.55 ± 0.25	6.9 ± 7.0	-0.61 ± 0.66	635.43 ± 383.09	0.748 ± -0.252
P180.3206+02.5788	-0.05 ± 0.10	-11.36 ± 0.06	0.1616 ± 0.0608	4.4 ± 1.1	59.9 ± 78.7	0.82 ± 0.10	51.2 ± 58.1	0.25 ± 0.37	3365.47 ± 795.44	0.136 ± -0.228
P182.5866+09.8940	-76.32 ± 0.09	-46.52 ± 0.06	0.7807 ± 0.0476	4.5 ± 0.4	34.2 ± 12.0	0.75 ± 0.05	10.5 ± 4.6	-0.87 ± 0.10	372.56 ± 89.22	0.339 ± -0.162
P184.1783+01.0664	-1.92 ± 0.12	-6.88 ± 0.07	0.2203 ± 0.0587	8.3 ± 0.1	27.3 ± 0.8	0.53 ± 0.01	26.2 ± 0.8	-0.30 ± 0.12	5894.07 ± 637.49	0.383 ± -0.014
P184.2997+43.4721	-19.30 ± 0.05	-37.97 ± 0.06	1.4142 ± 0.0506	1.8 ± 0.1	8.5 ± 0.0	0.64 ± 0.02	2.5 ± 0.2	0.31 ± 0.02	245.74 ± 4.87	1.140 ± -0.005
P188.0262+00.2055	25.18 ± 0.10	-35.02 ± 0.07	0.7269 ± 0.0441	1.6 ± 0.2	21.4 ± 1.9	0.86 ± 0.02	4.1 ± 0.4	0.34 ± 0.03	145.12 ± 5.97	0.600 ± -0.051
P191.8535+12.0508	-11.78 ± 0.08	-0.00 ± 0.05	0.4436 ± 0.0362	4.7 ± 0.2	9.5 ± 0.2	0.34 ± 0.03	2.5 ± 0.2	0.64 ± 0.02	233.92 ± 21.55	0.958 ± -0.003
P192.3242+13.3956	-12.93 ± 0.09	-1.36 ± 0.06	0.2900 ± 0.0435	2.6 ± 0.4	11.1 ± 0.8	0.62 ± 0.07	4.2 ± 0.7	0.42 ± 0.05	392.90 ± 52.80	0.946 ± -0.031
P194.9935+12.0585	-32.89 ± 0.07	-27.50 ± 0.05	0.8620 ± 0.0335	0.6 ± 0.2	8.2 ± 0.4	0.86 ± 0.04	3.8 ± 0.4	0.10 ± 0.03	349.95 ± 37.17	1.183 ± -0.004
P198.0851+8.9428	-0.22 ± 0.10	-0.72 ± 0.07	-0.0585 ± 0.0555	23.9 ± 28.5	86.0 ± 247.6	0.33 ± 0.20	55.6 ± 85.7	-0.06 ± 0.56	15444.69 ± 23639.44	0.204 ± -0.445
P207.3454+14.1268	-6.03 ± 0.14	-16.95 ± 0.10	0.5402 ± 0.0814	2.6 ± 0.6	8.0 ± 0.1	0.52 ± 0.09	3.6 ± 0.4	0.35 ± 0.08	485.66 ± 64.42	1.124 ± -0.021
P207.9290+03.2767	-27.35 ± 0.07	-9.93 ± 0.05	0.4321 ± 0.0411	0.9 ± 0.4	11.6 ± 65.9	0.83 ± 0.07	8.4 ± 59.7	-0.12 ± 0.07	813.71 ± 58.63	1.065 ± -0.043
P209.0986+9.8244	-20.90 ± 0.08	-1.71 ± 0.06	0.3218 ± 0.0435	1.5 ± 0.4	14.1 ± 2.0	0.80 ± 0.07	10.4 ± 3.3	0.19 ± 0.08	1086.27 ± 316.95	0.825 ± -0.073
P224.8444+02.3043	-2.31 ± 0.06	-0.10 ± 0.06	0.0194 ± 0.0397	13.4 ± 13.6	331.6 ± 662.9	0.76 ± 0.15	239.9 ± 476.0	0.57 ± 1.10	11107.29 ± 13163.12	-0.105 ± -0.728
P236.9604+11.6155	-0.86 ± 0.09	-3.12 ± 0.14	0.1705 ± 0.0599	4.1 ± 0.6	6.3 ± 0.3	0.21 ± 0.06	3.9 ± 1.0	0.38 ± 0.11	883.84 ± 371.10	1.147 ± -0.035
P237.8589+12.5660	-5.94 ± 0.06	-7.86 ± 0.05	0.2971 ± 0.0410	2.1 ± 0.4	6.6 ± 0.1	0.52 ± 0.07	2.5 ± 0.4	0.30 ± 0.06	328.14 ± 71.82	1.268 ± -0.026
P244.8986+10.9310	-16.05 ± 0.06	-12.30 ± 0.04	0.3805 ± 0.0588	1.1 ± 0.6	7.9 ± 14.5	0.74 ± 0.14	2.3 ± 6.0	-0.17 ± 0.09	209.31 ± 17.05	1.291 ± -0.013
P246.9682+08.5360	-6.41 ± 0.05	12.37 ± 0.04	0.2747 ± 0.0392	3.7 ± 0.4	28.7 ± 6.8	0.76 ± 0.07	9.5 ± 3.5	0.69 ± 0.04	398.12 ± 84.91	0.424 ± -0.118
P247.2115+06.6348	-1.27 ± 0.06	-2.96 ± 0.03	0.0830 ± 0.0410	2.6 ± 0.9	7.9 ± 2.6	0.47 ± 0.21	7.2 ± 1.9	-0.02 ± 0.15	1900.73 ± 456.17	1.101 ± -0.116
P257.3131+12.8939	2.14 ± 0.07	-1.62 ± 0.06	0.0565 ± 0.0370	8.4 ± 3.5	23.5 ± 32.4	0.37 ± 0.12	22.7 ± 32.3	-0.06 ± 0.26	5781.40 ± 3366.22	0.610 ± -0.363
P258.1048+40.5405	0.83 ± 0.06	1.07 ± 0.08	0.3890 ± 0.0364	3.0 ± 0.0	8.3 ± 0.0	0.47 ± 0.00	4.7 ± 0.2	0.37 ± 0.01	736.29 ± 55.41	1.076 ± -0.005
P339.1417+25.5503	33.41 ± 0.06	11.41 ± 0.05	0.9142 ± 0.0342	2.6 ± 0.1	12.8 ± 0.4	0.66 ± 0.02	0.8 ± 0.0	0.50 ± 0.01	22.68 ± 0.72	0.883 ± -0.014
P339.3203+25.8764	20.30 ± 0.08	2.16 ± 0.06	0.2368 ± 0.0438	2.0 ± 1.1	46.0 ± 76.7	0.90 ± 0.02	9.4 ± 19.7	-0.45 ± 0.22	157.15 ± 57.13	0.337 ± -0.308

This paper has been typeset from a \TeX/L\AA\TeX file prepared by the author.